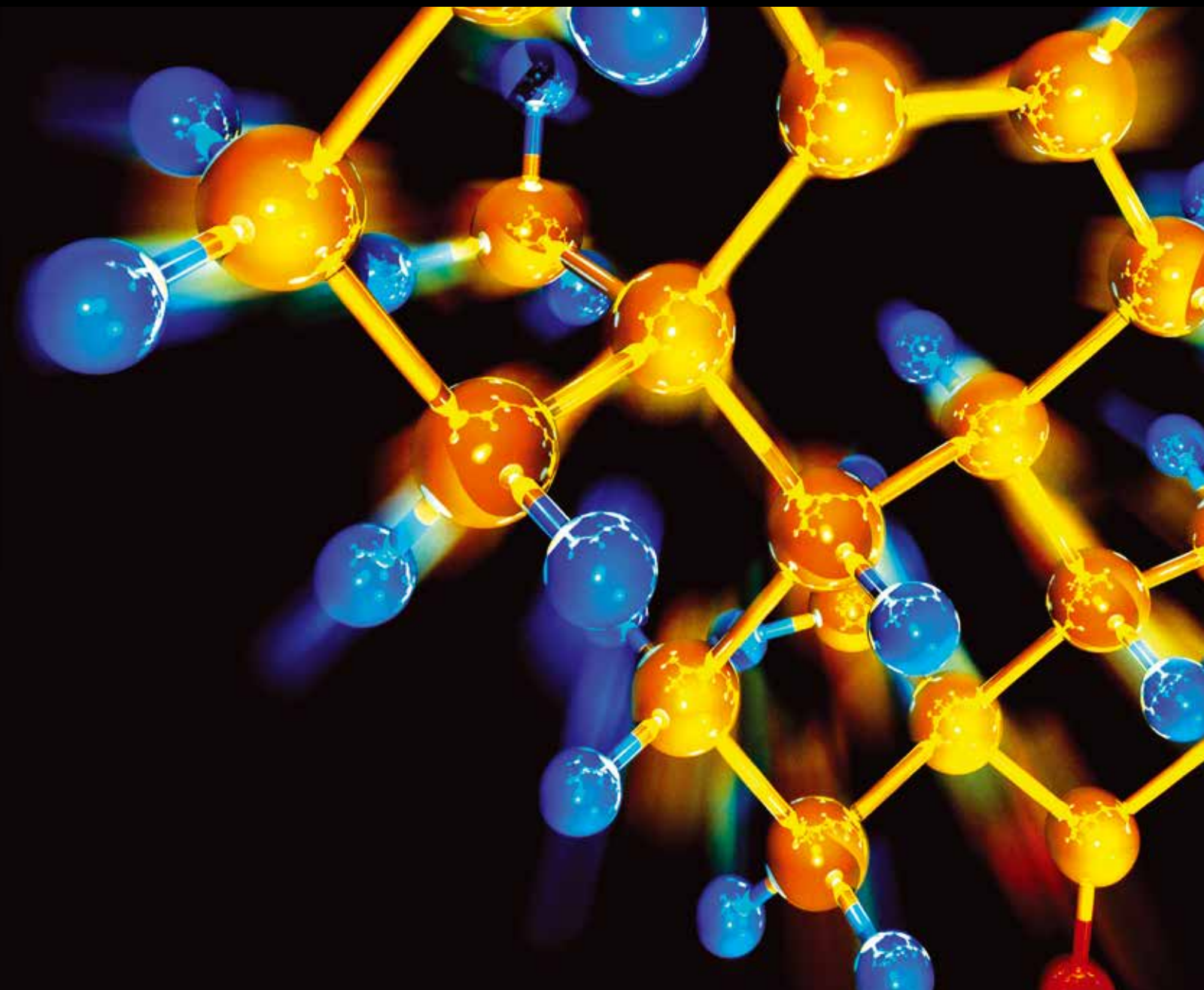


The Application of Advanced Materials on the Water or Wastewater Treatment

Guest Editors: Yalei Zhang, Asit Mazumder, Tian C. Zhang, and Chaomeng Dai u





The Application of Advanced Materials on the Water or Wastewater Treatment

The Application of Advanced Materials on the Water or Wastewater Treatment

Guest Editors: Yalei Zhang, Asit Mazumder, Tian C. Zhang, and Chaomeng Dai



Copyright © 2015 Hindawi Publishing Corporation. All rights reserved.

This is a special issue published in "Journal of Chemistry." All articles are open access articles distributed under the Creative Commons Attribution License, which permits unrestricted use, distribution, and reproduction in any medium, provided the original work is properly cited.

Contents

The Application of Advanced Materials on the Water or Wastewater Treatment, Yalei Zhang, Asit Mazumder, Tian C. Zhang, and Chaomeng Dai
Volume 2015, Article ID 369102, 2 pages

Effect of Li(I) and TiO₂ on the Upconversion Luminance of Pr:Y₂SiO₅ and Its Photodegradation on Nitrobenzene Wastewater, Yi Yang, Guang-Zhi Xia, Cheng Liu, Jin-Hua Zhang, and Lian-Jun Wang
Volume 2015, Article ID 938073, 7 pages

Actual Application of a H₂-Based Polyvinyl Chloride Hollow Fiber Membrane Biofilm Reactor to Remove Nitrate from Groundwater, Yanhao Zhang, Lilong Huang, Zhibin Zhang, Cuizhen Sun, and Jixiang Li
Volume 2015, Article ID 349830, 7 pages

Preparation and Characteristics of Polyaluminium Chloride by Utilizing Fluorine-Containing Waste Acidic Mother Liquid from Clay-Brine Synthetic Cryolite Process, Feng-shan Zhou, Bo Hu, Bao-lin Cui, Feng-bao Liu, Fang Liu, Wei-heng Wang, Yang Liu, Rong-rong Lu, Ying-Mo Hu, Yi-he Zhang, and Jin-Guang Wu
Volume 2014, Article ID 274126, 7 pages

The Effect of Salinity on Membrane Fouling Characteristics in an Intermittently Aerated Membrane Bioreactor, Kang Xie, Siqing Xia, Jing Song, Jixiang Li, Liping Qiu, Jiabin Wang, and Shoubin Zhang
Volume 2014, Article ID 765971, 7 pages

Dechlorination of Hexachloroethane in Water Using Iron Shavings and Amended Iron Shavings: Kinetics and Pathways, D. L. Wu, Y. X. Liu, Z. G. Liu, and L. M. Ma
Volume 2014, Article ID 325879, 9 pages

Preparation and Application of Sustained-Release Potassium Ferrate(VI), Xuan Xu, Wei Wei, Ping Tao, and Yan Zhang
Volume 2014, Article ID 640757, 7 pages

Editorial

The Application of Advanced Materials on the Water or Wastewater Treatment

Yalei Zhang,¹ Asit Mazumder,^{2,3} Tian C. Zhang,⁴ and Chaomeng Dai⁵

¹College of Environmental Science and Engineering, Tongji University, 1239 Siping Road, Shanghai 200092, China

²Department of Biology, University of Victoria, 3800 Finnerty Road, Victoria, BC, Canada V8W 2Y2

³Shenzhen Institute of Advanced Technology, Laboratory for Food Safety and Environmental Technology, Chinese Academy of Science, Shenzhen, China

⁴Department of Civil Engineering, Engineering College, University of Nebraska-Lincoln at Omaha Campus, 205D PKI, Omaha, NE 68182-0178, USA

⁵Department of Hydraulic Engineering, College of Civil Engineering, Tongji University, 1239 Siping Road, Shanghai 200092, China

Correspondence should be addressed to Yalei Zhang; zhangyalei@tongji.edu.cn

Received 27 November 2014; Accepted 27 November 2014

Copyright © 2015 Yalei Zhang et al. This is an open access article distributed under the Creative Commons Attribution License, which permits unrestricted use, distribution, and reproduction in any medium, provided the original work is properly cited.

Water scarcity is being recognized as a present and future threat to human activity, and, as a consequence, water purification technologies are gaining major worldwide attention. Advanced materials have many properties, such as strong adsorption, enhanced redox, and photocatalytic properties, providing unprecedented opportunities to treat surface water, groundwater, and industrial wastewater that are contaminated with toxic metals, organic and inorganic compounds, bacteria, and viruses. Currently, tremendous progress has been made in development of advanced materials for their environmental applications, and knowledge has been accumulated of the effects of these advanced materials on and their applications in the environment security, recycling, and reuse of raw materials and treatment agents, economic benefits, and potential problems to our society. This special issue aims to provide an up-to-date account of advancement in these areas as well as insights gained through field experience.

Specifically, this special issue aims to study (a) advanced materials and advanced composite materials applications in water treatment, industry wastewater treatment, resource reuse of noble metals (e.g., gold, silver) from industry wastewater, environmental analysis, and groundwater remediation; (b) potential toxicity of engineered advanced (composite) materials; (c) transformations of advanced (composite) materials in the environment; and (d) modifications of advanced (composite) materials for enhancing contaminant uptake from aqueous solutions. While the selected six papers may not fully cover the topic of this special issue, they represent

the rich and many-faceted knowledge that we are pleased to share with the readers.

Y. Zhang et al. present an updated review on removing nitrate from groundwater, focusing on innovative ideas as compared to the traditional way. Their work highlights the actual performance of a polyvinyl chloride (PVC) membrane biofilm reactor for removing nitrate from groundwater, with the influences of DO and membrane fouling on the process being assessed.

Offcuts and natural mineral are important materials for removing pollutants due to their low cost. In particular in developing countries, high cost is the main factor that limits the development of environmental protection industry. D. L. Wu et al. demonstrated that iron shavings, a common byproduct of mechanical processing plants, can offer superior reductive dechlorination of hexachloroethane (HCA). While the purity of such Fe metals may be low, these shavings are readily available at low costs and could potentially be used for remediation. "Treating wastes with another waste" is a sustainable approach in environmental engineering fields. F. Zhou et al. prepared and characterized polyaluminium chloride by utilizing fluorine-containing waste with acidic mother liquids from the clay-brine synthetic cryolite process, with detailed processes of the synthesis and characteristics being described.

X. Xu et al. present their work on preparation and application of sustained-release potassium ferrate (VI). They describe a novel encapsulation method using hypochlorite

oxidation to prepare sustained-release K_2FeO_4 during water treatment. Composite materials have gained the unprecedented development in recent years, but they also have many problems, such as the stability, economical efficiency, applicability, and feasibility. The article provides the insight on how to make a composite material have a better performance than the individual materials.

Y. Yang et al. prepared Li(I) doped $Pr:Y_2SiO_5$ upconversion materials and anatase TiO_2 nanofilm coated $Li,Pr:Y_2SiO_5$ composite. They tested the luminescence intensities emitted by these composite materials and the photodegradation performances of these materials for treatment of nitrobenzene in wastewater. Their results show that $Li,Pr:Y_2SiO_5$ has a much better photodegradation performance than $Pr:Y_2SiO_5$, indicating that rare earth luminescent materials may have much greater application potential when combined with (or doped by) other materials (e.g., anatase TiO_2 and rare earth ions).

K. Xie et al. evaluated the effect of salinity on membrane fouling characteristics in an intermittently aerated membrane bioreactor (IAMBR). They investigated the system performance and variation of sludge characteristics at different salinities. The membrane fouling may be attributed to the interactions of the variation of sludge characteristics caused by salinity. Therefore, future studies should pay more attention to expand our knowledge of the relationship among the membrane fouling and sludge characteristics in salinity wastewater.

We believe that this special issue can benefit researchers, practitioners, and educators. The readers will find that this special issue not only contains accurate information and updated reviews on some advanced (composite) materials, but also has extensive applications of new materials. We also hope that the special issue will give more inspiration for the development of new or composite advanced materials in the future.

*Yalei Zhang
Asit Mazumder
Tian C. Zhang
Chaomeng Dai*

Research Article

Effect of Li(I) and TiO₂ on the Upconversion Luminescence of Pr:Y₂SiO₅ and Its Photodegradation on Nitrobenzene Wastewater

Yi Yang,^{1,2} Guang-Zhi Xia,¹ Cheng Liu,¹ Jin-Hua Zhang,^{1,2} and Lian-Jun Wang^{1,2}

¹School of Environmental and Biological Engineering, Nanjing University of Science and Technology, Nanjing 210094, China

²Lianyungang Institute, Nanjing University of Science and Technology, Lianyungang 222006, China

Correspondence should be addressed to Yi Yang; yyi301@163.com

Received 16 April 2014; Accepted 27 August 2014

Academic Editor: Tian C. Zhang

Copyright © 2015 Yi Yang et al. This is an open access article distributed under the Creative Commons Attribution License, which permits unrestricted use, distribution, and reproduction in any medium, provided the original work is properly cited.

Based on the substrate of Pr:Y₂SiO₅ upconversion nanomaterials, lithium ion Li(I) doped Pr:Y₂SiO₅ and TiO₂ nanofilm coated Li,Pr:Y₂SiO₅ composites were prepared by using a sol-gel method. X-ray diffractometer, SEM, and fluorescence spectrometer have been employed to test the crystal structure, microimages, and upconversion luminescence performances. The doping of Li(I) affects highly the crystal transition of Pr:Y₂SiO₅ and X₂-Y₂SiO₅ phase was well formed by doping 8% Li(I). Furthermore, the doping of Li(I) also brings high luminance intensity of Pr:Y₂SiO₅ and contributes to a maximum intensity of 9.76×10^6 cps doped 8%. Too much of Li(I) doping would result in big crystal size and fluorescence quenching of Pr:Y₂SiO₅ material. However, the coating of TiO₂ nanofilm is not helping in increasing the upconversion fluorescence of Li,Pr:Y₂SiO₅ but is promoting the full use of the fluorescence. The luminescence intensities of TiO₂/Li,Pr:Y₂SiO₅ composites are getting down sharply with the coating amount since the luminescence emitted by Li,Pr:Y₂SiO₅ is quickly adsorbed in situ by the TiO₂ coating film. With the optimum coating concentration of 1%, the TiO₂/Li,Pr:Y₂SiO₅ composite shows excellent photodegradation performances on nitrobenzene wastewater, though it shows a low luminescence intensity. For 5 mg/L nitrobenzene wastewater, the composite presents a photodegradation rate of 97.08% in 4 hours.

1. Introduction

Currently, rare earth luminescent materials have been widely studied and used in information display, lighting, and other areas of optoelectronic devices supporting material [1–5], since its phosphor high luminous intensity and good shape can effectively improve the microscopic performance of the display. However, researches focused on the luminescence application in other fields, which the fluorescent materials emitted, are not as much as in the display fields. Some reports aimed at biological application, such as antibacterials [6, 7], and some researchers focus on environmental application of the luminescent materials [8, 9].

As one of the most researched luminescent material, yttrium silicates Y₂SiO₅ has a great potential application in many fields because of its high stability and good luminescence properties. Activated Y₂SiO₅ luminescent material

which is usually doped with other metal ions or activating agents is widely researched because of its much higher luminescence intensity than that of nonactivated material [10, 11]. Yttrium silicates Y₂SiO₅ has a particular geometry which leads to a possible replace of Y by other element ions, especially rare earth ions [12]. For example, Ce(III) doped Y₂SiO₅ can replace ZnS:Ag and can be used as blue phosphors for field emission display (FED); Tb(III) doped Y₂SiO₅ is a kind of cathode luminescence materials. Praseodymium ion Pr(III) has a similar ionic radius with Y ion but more suitable energy levels and longer excited state lifetimes than Y. As a result, higher energy photons and higher luminescence intensity could be emitted. Because of the small ionic radius, lithium ion Li(I) can easily get into the crystal lattice and replace the host atoms of Y₂SiO₅.

The photocatalytic behavior of TiO₂ has been studied extensively, because of the ability of nanoscale TiO₂ to

decompose a wide variety of inorganic and organic pollutants and toxic material in both liquid and gas phase systems [13–15], as well as the photocatalysis of nanoscale TiO_2 and its application for water purification [16, 17]. However, only ultraviolet light wavelength less than 387 nm, which is about 4% of the solar light, can be absorbed by pure anatase TiO_2 , since the energy gap of pure anatase TiO_2 is about 3.2 eV [18]. This became the main barrier which is limiting the wide use of TiO_2 as a photocatalyst. Many methods can be used to develop TiO_2 as a promising photocatalyst for wastewater treatment, such as surface modification [19, 20], doping with other metal ions, nonmetal ions and semiconductors [21–25], and oxygen vacancy generating [26].

The combination of anatase TiO_2 with upconversion materials could hopefully make more efficient use of solar energy in practical applications and provide a wide use of TiO_2 in photodegradation fields. In this study, Li(I) doped $\text{Pr:Y}_2\text{SiO}_5$ upconversion materials and anatase TiO_2 nanofilm coated Li,Pr: Y_2SiO_5 composite have been prepared and the luminescence intensities they emitted were tested. Nevertheless, the photodegradation performances of the as-prepared materials have been tested on the target pollutant of nitrobenzene wastewater.

2. Materials and Methods

2.1. Preparation of Samples. Praseodymium ion Pr(III), 1%, doped Y_2SiO_5 upconversion nanomaterials were prepared by following [8]. First, 0.1 mol/L praseodymium nitrate solution was added to the mixture (1:1, vol) of HNO_3 and H_2O dissolving 0.663 g Y_2O_3 . Heating was followed until the solution became a viscous mixture. A number of crystals were seed out after cooling down. The crystal was collected and dissolved in ethanol. Tetraethyl orthosilicate (TEOS) was added and mixed with the ethanol solution of the crystals. The obtained mixture was put into a water bath of 70 °C until a gel was formed. The gel was dried in an oven at 104 °C and then ground into powder. At last, the powder was calcined at a temperature of 950 °C for 3 h in a muffle furnace to get the product $\text{Pr:Y}_2\text{SiO}_5$ upconversion nanomaterials.

Lithium ion Li(I) doped $\text{Pr:Y}_2\text{SiO}_5$ nanomaterials were prepared by adding 0.1 mol/L lithium nitrate to the praseodymium nitrate solution at the first step during the preparation of $\text{Pr:Y}_2\text{SiO}_5$. Then, sol-gel process and heat treatment parameters were followed as in the preparation of $\text{Pr:Y}_2\text{SiO}_5$ nanomaterials. The lithium ion doping concentrations, 2%, 6%, 8%, and 10%, were adjusted by changing the added volume of lithium nitrate solution. These products were called as Li,Pr: Y_2SiO_5 .

The composite catalysts of $\text{TiO}_2/\text{Li,Pr:Y}_2\text{SiO}_5$ were prepared by adding the as-prepared Li,Pr: Y_2SiO_5 powder, which was ground and ultrasonic-dispersed in absolute alcohol for 30 min, to the mixture of titanium tetrabutoxide, absolute alcohol, and distilled water with a volume ratio of 1 : 7 : 2. The mixture was adjusted to pH 2.5 by using nitric acid. After stirring for 1 h, the suspension was put into a water bath at 70 °C to form a white gel. Then, the gel was dried in an oven at 80 °C and ground into powder. At last, the powder

was calcined at a temperature of 500 °C for 2 h in a muffle furnace to get the product $\text{TiO}_2/\text{Li,Pr:Y}_2\text{SiO}_5$ composite catalyst. The TiO_2 concentrations, 0.3%, 0.5%, 1.0%, and 2.0%, were adjusted by changing the added volume of titanium tetrabutoxide.

2.2. Property Testing of Samples. A scanning electron microscopy (Hitachi S4800, SEM, Japan) was employed to characterize the microimages and particle size of the samples. X-ray diffractometer (D8 Advance, Bruker Corporation, German) was used to characterize the crystal form of the samples. The upconversion luminescence of the nanomaterials was tested by using a fluorescence spectrometer (FL3-TCSPC, Horiba Jobin Yvon Corporation, France). The exciting parameters were selected as 488 nm of the excitation wavelength, 370 nm of the optical filters, and 1 nm of the slit [27, 28].

Nitrobenzene wastewater, which was from a TNT factory and was diluted to 5 mg/L, was used as a target pollutant to test the photodegradation performances of the as-prepared upconversion nanomaterials. Triphosphor tube light, 100 W, was used as the exciting light source for the upconversion nanomaterials. The treatment time lasted for 1 h to 6 h. The degradation rate of nitrobenzene was calculated by comparing the ultraviolet absorption values at the wavelength of 267 nm to the original values of the nitrobenzene solution. The ultraviolet absorption values were tested by using an ultraviolet-visible spectrophotometer. The relationship of the nitrobenzene concentrations (x), in the range of 0.5–10 mg/L, with the ultraviolet absorption value (y), was determined by a linear equation $y = 9.06x - 0.312$, with a correlation R^2 of 0.99982.

3. Results and Discussion

3.1. $\text{Pr:Y}_2\text{SiO}_5$ with Different Li(I) Concentrations. Doping ions are known for changing crystal structure and crystal size, as well as light conversion performances for upconversion nanomaterials [8, 9]. Figure 1 shows the XRD patterns of $\text{Pr:Y}_2\text{SiO}_5$ with different Li(I) concentrations, 0%, 2%, 6%, 8%, and 10%.

It is known that Y_2SiO_5 has two types of crystal structure, low-temperature (X1) and high temperature (X2), when taking high temperature structure, with better emission performances. It is very interesting that the doping amount of Li(I) contributes a great effect to the crystal transition of Y_2SiO_5 materials. When the doping amounts of Li(I) are not bigger than 6%, the crystal form of samples belongs to low-temperature phase X1 molecular configuration (X1- Y_2SiO_5), which is corresponding to the PDF card number of #52-1810. However, when the doping amounts are high as 8%, the crystal forms of Y_2SiO_5 materials transfer from X1- Y_2SiO_5 to X2- Y_2SiO_5 phase, which is corresponding to the PDF card number of #21-1458, as shown in Figure 2. Generally, for X2- Y_2SiO_5 materials, heat treatment temperature up to 1350 °C is needed [12], instead of 950 °C in this study. It indicates that the doping of Li(I) can effectively decrease the crystallization temperature of Y_2SiO_5 and promotes the crystallization of X2- Y_2SiO_5 at a lower temperature. When the doping amount

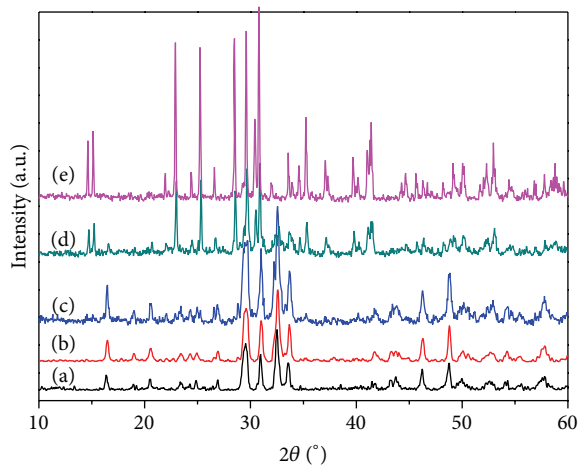


FIGURE 1: XRD patterns of Pr:Y₂SiO₅ doped different concentrations of Li(I). (a) 0%; (b) 2%; (c) 6%; (d) 8%; (e) 10%.

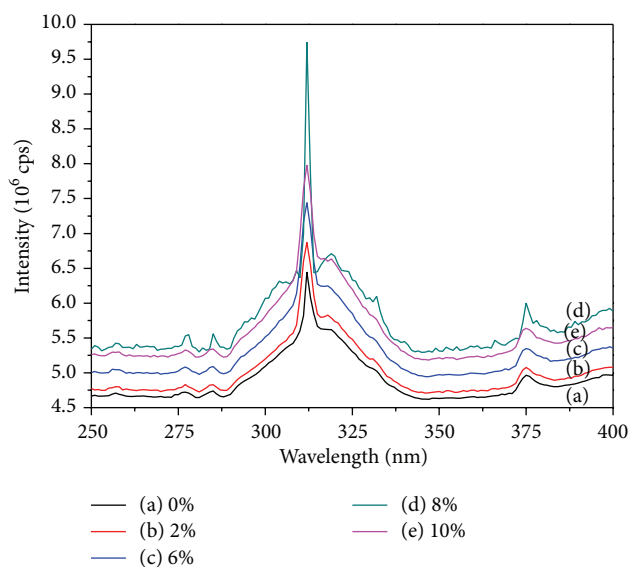


FIGURE 2: Emission spectra of Pr:Y₂SiO₅ doped different concentrations of Li(I). (a) 0%; (b) 2%; (c) 6%; (d) 8%; (e) 10%.

of Li(I) is increased to 10%, the diffraction peaks show much more sharp than that of 8%. The crystal sizes of Pr:Y₂SiO₅ with 8% and 10% Li(I) are 47.8 nm and 62.5 nm at 2θ angle 30.83°, respectively, which are calculated by the Scherrer equation [29]: $D = K\lambda/(\beta \cos \theta)$, where D is the crystal size (nm); K is 0.89, the Scherrer constant; θ is the diffraction angle at which the diffraction peaks are located (°); β is the full width at half maximum (FWHM) of the main diffraction peaks (rad), which is located at the 2θ angle of 30.83° in this situation; λ is 0.154056 nm, the X-ray wavelength.

Figure 2 shows the upconversion luminescence emission spectra of Pr:Y₂SiO₅ doped with different concentrations of Li(I). Since the excitation wavelength is set on 488 nm, the peaks of the upconversion luminescence emission spectra are located at 312 nm, instead of 425 nm and 360 nm of

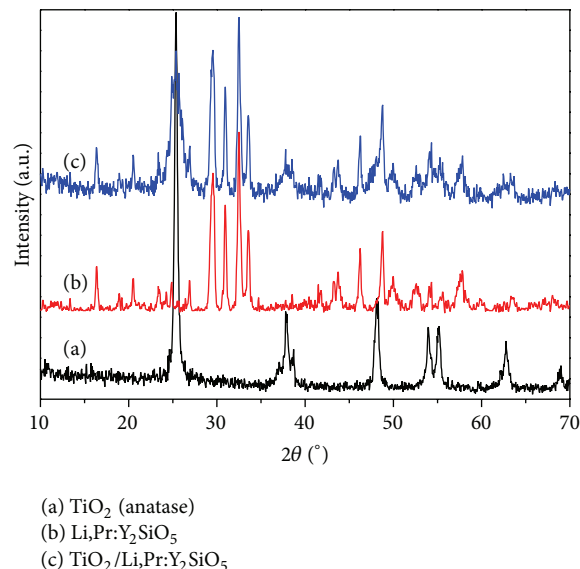


FIGURE 3: XRD patterns of samples. (a) Commercial anatase TiO₂; (b) Li,Pr:Y₂SiO₅; (c) TiO₂/Li,Pr:Y₂SiO₅.

the excitation wavelength and the emission spectra peaks, respectively [8].

As the Li(I) doping amount increases, the intensity of the emission spectra is increasing gradually but is getting down at the doping amount of 10%, as shown in Figure 2. Sample doped with 8% Li(I) shows the strongest luminescence intensity of 9.76×10^6 cps (count per second), which is about 1.5 times of the blank sample Pr:Y₂SiO₅ (0% Li) emitted at the wavelength of 312 nm. Compared to lower doping samples, sample doped with 8% Li(I) emits much stronger upconversion luminescence, which has more intact X2-Pr:Y₂SiO₅ structures according to the test results in Figure 1. On the other hand, too much of Li(I) doping amount, as shown in Figure 1, would result in big crystal size of Pr:Y₂SiO₅ nanomaterials. For upconversion luminescence nanomaterials, a smaller crystal size hopefully contributes to higher upconversion efficiency. However, it is believed that too high doping concentration of exotic ions would result in luminescent quenching [30]. As a result, the doping concentration of 10% Li(I) results in a low luminescence intensity, as shown in Figure 2. Therefore, Pr:Y₂SiO₅ upconversion nanomaterial doping 8% Li(I), which has a smaller crystal size and less fluorescence quenching, emits much stronger luminescence than that of doping 10% Li(I), as shown in Figure 2.

3.2. Testing of TiO₂/Li,Pr:Y₂SiO₅ Composites. It is different with doping of ions; doping of nanomaterials would seldom change the crystal structure of the host material. Figure 3 shows the XRD patterns of three kinds of samples, commercial nanometer TiO₂ (anatase), as-prepared Li,Pr:Y₂SiO₅ (8% Li), and as-prepared TiO₂/Li,Pr:Y₂SiO₅ (1% TiO₂).

As shown in Figure 3, the XRD pattern of sample (c) is seemingly the combination of that of sample (a) and sample (b), which clearly corresponds to the XRD diffraction peaks

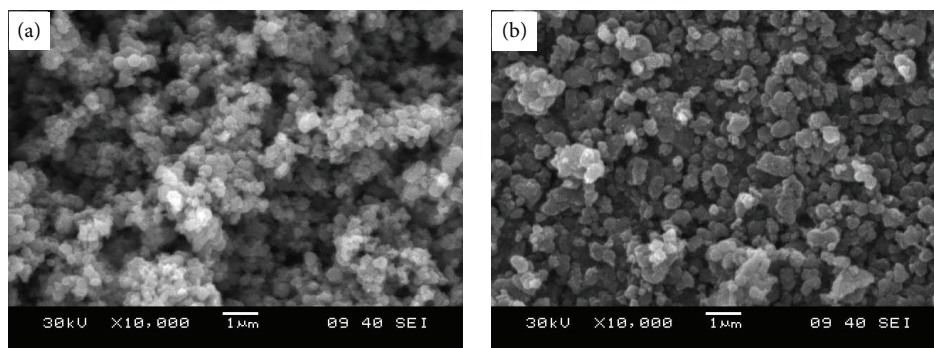


FIGURE 4: SEM photos of (a) $\text{Li,Pr:Y}_2\text{SiO}_5$ and (b) $\text{TiO}_2/\text{Li,Pr:Y}_2\text{SiO}_5$ nanomaterials.

of TiO_2 and $\text{Li,Pr:Y}_2\text{SiO}_5$. However, comparing the intensities of diffraction peaks belonging to TiO_2 , the diffraction intensities of sample (c) are much lower than those of sample (a), commercial anatase TiO_2 . On the other hand, the diffraction intensities belonging to $\text{Li,Pr:Y}_2\text{SiO}_5$ do not show big differences between $\text{Li,Pr:Y}_2\text{SiO}_5$ and its composite. It indicates that TiO_2 and $\text{Li,Pr:Y}_2\text{SiO}_5$ are two independent materials coexisted in the composite of $\text{TiO}_2/\text{Li,Pr:Y}_2\text{SiO}_5$. Titanium dioxide probably in the form of films exists on the surface of $\text{Li,Pr:Y}_2\text{SiO}_5$ particles, which also can be suggested by the SEM photos of the samples, as shown in Figure 4.

Figure 4(a) shows SEM photo of $\text{Li,Pr:Y}_2\text{SiO}_5$ particles, which presents regular but partially reunited spherical particles in the diameter of 300 nm to 500 nm. A little different from $\text{Li,Pr:Y}_2\text{SiO}_5$ sample, $\text{TiO}_2/\text{Li,Pr:Y}_2\text{SiO}_5$ nanoparticles show good dispersibility and are a little big in size, which is in the range of 500 nm to 800 nm, as shown in Figure 4(b). Much bigger particle sizes in SEM than those of XRD indicate that every single particle is composed of several crystals which makes it difficult to disperse the $\text{Li,Pr:Y}_2\text{SiO}_5$ powders fully in the preparation process. Energy dispersive X-ray spectrometer (EDS) testing on the sample surface of Figure 4(b) shows that Ti and O are the majority of elements, while Si and Y are the minority of elements. It is difficult to find element information of Li and Pr in the EDS testing. It suggests that TiO_2 film gives intact coating for $\text{Li,Pr:Y}_2\text{SiO}_5$ particles in a thickness of about 100 nm to 150 nm.

Figure 5 shows the upconversion emission spectra of $\text{Li,Pr:Y}_2\text{SiO}_5$ with different concentrations of TiO_2 . It is very different to the situation of doping with Li(I) and Pr(III); the upconversion luminescence intensities are decreasing with the coating amount of TiO_2 , instead of increasing by the doping amount of Li(I) and Pr(III). This should be attributed to the semiconductor characteristics of TiO_2 . It is known that titanium dioxide is a kind of *n*-type semiconductor material with a band gap of 3.2 eV (for anatase). When it is exposed to ultraviolet light whose wavelength is less than 387.5 nm, energy would be added to valence electron and it would be excited by photon and would leap from the valence band (VB) to the conduction band (CB), where it can move freely around the crystal in the form of photoelectron [31]. As a result, a hole is left behind in the valence band. On the occasion

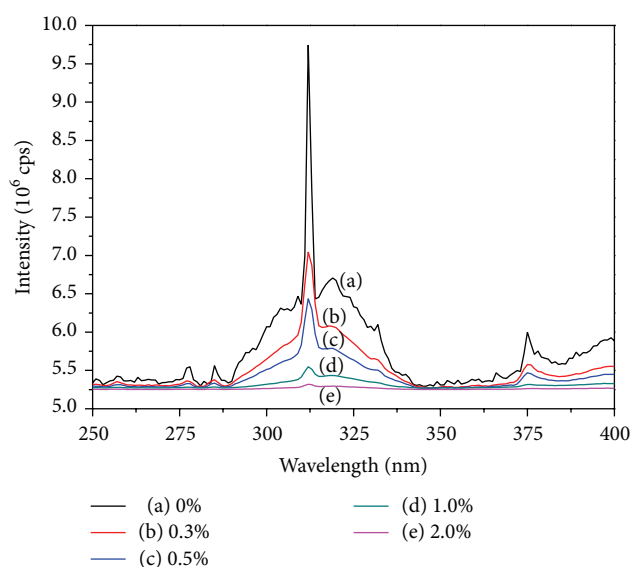


FIGURE 5: Emission spectra of $\text{Li,Pr:Y}_2\text{SiO}_5$ with different concentrations of TiO_2 . (a) 0%; (b) 0.3%; (c) 0.5%; (d) 1.0%; (e) 2.0%.

of nanoscale TiO_2 coating on the upconversion material $\text{Li,Pr:Y}_2\text{SiO}_5$, the luminescence emitted by $\text{Li,Pr:Y}_2\text{SiO}_5$ is absorbed in situ by the TiO_2 coating film. When more of TiO_2 film is coated, less of the luminescence intensity can be tested. When the coating amount of TiO_2 film is up to 1%, the intensity of the emission spectra is very low. There almost can not be found luminescence peaks on the emission spectra of the sample with 2% of TiO_2 , as shown in Figure 5. It means that too much of coating TiO_2 would absorb out all the luminescence that the upconversion material $\text{Li,Pr:Y}_2\text{SiO}_5$ emitted. Therefore, the coating amount of 1% could be a balance point or optimum value for the composite of $\text{TiO}_2/\text{Li,Pr:Y}_2\text{SiO}_5$ nanomaterials.

3.3. Photodegradation of Nitrobenzene Wastewater. Nitrobenzene wastewater, which is an environmental priority control pollutant, usually comes from the factories manufacturing medicines, pesticides, plastics, and explosives. The

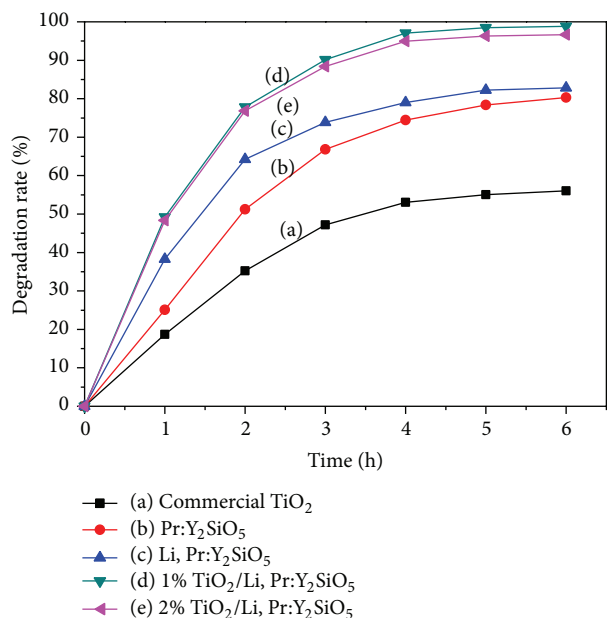


FIGURE 6: The photodegradation performances of nanomaterial samples. (a) Commercial TiO₂; (b) Pr:Y₂SiO₅; (c) Li,Pr:Y₂SiO₅; (d) 1% TiO₂/Li,Pr:Y₂SiO₅; (e) 2% TiO₂/Li,Pr:Y₂SiO₅.

degradation-resistant pollutant, which is attributed to its particular molecular structures, is difficult to degrade by normal methods [32]. In this study, 5 mg/L nitrobenzene wastewater and 1.5 g/L photocatalysts are used to test the photodegradation performances of as-prepared samples. The photodegradation curves of nitrobenzene wastewater with the photocatalysts of commercial nanometer anatase TiO₂, Pr:Y₂SiO₅, Li,Pr:Y₂SiO₅, 1% TiO₂/Li,Pr:Y₂SiO₅ (with 1% of TiO₂, similarly hereinafter), and 2% TiO₂/Li,Pr:Y₂SiO₅, are shown in Figure 6. All the data in Figure 6 are the mean values measured 3 times.

Samples TiO₂/Li,Pr:Y₂SiO₅, curves (d) and (e), show excellent photodegradation performances, but commercial TiO₂ shows the worst in the samples. Nanoscale TiO₂ is known for its good photocatalysis performances on pollutions under ultraviolet light. However, very different situation for nanoscale TiO₂ would arise when it is exposed to visible light. Thus, in this study, compounding of TiO₂ with Li,Pr:Y₂SiO₅ nanomaterials, which can upconvert visible light to ultraviolet light, would significantly improve the photocatalysis performances of TiO₂ under visible light, as shown in Figure 6. Although the luminescence intensities of TiO₂/Li,Pr:Y₂SiO₅ composite are far lower than that of Li,Pr:Y₂SiO₅ nanomaterials, as shown in Figure 5, it does not mean that the upconversion processes of Li,Pr:Y₂SiO₅ in the composite are stopped. It is still working well in the form of promoting and strengthening the photocatalysis of TiO₂ by providing high energy photons, instead of in the form of high intensity of upconversion luminescence emit out of the materials which can be tested, as shown in Figures 5 and 6. On the other hand, too much coating of TiO₂ film would not only

increase the barrier of visible light to Li,Pr:Y₂SiO₅ nanomaterials, which weakens the intensity of incident light, but also decrease the proportion of Li,Pr:Y₂SiO₅ in the composite, in which the conversion of visible light to ultraviolet light is provided. Therefore, TiO₂/Li,Pr:Y₂SiO₅ coating with 2% TiO₂ shows a little bit poor photodegradation performance than that with 1% TiO₂, as shown in Figure 6.

For samples Pr:Y₂SiO₅ and Li,Pr:Y₂SiO₅, their photodegradation performances show high consistency with the intensities of upconversion luminescence which they emitted; the former is lower than the latter. Because of lack of direct or quick conversion ultraviolet light, high energy photons, to hydroxyl radical (•OH) [33], which is one of the most strong oxidizability matter, two of the upconversion nanomaterials show much more poor photodegradation performances than TiO₂/Li,Pr:Y₂SiO₅ composites.

4. Conclusions

Lithium ion Li(I) doped Pr:Y₂SiO₅ and TiO₂ nanofilm coated Li,Pr:Y₂SiO₅ composites were prepared by using a sol-gel method. The doping amount of Li(I) plays an important role on the upconversion luminescence of the nanomaterial which reaches a maximum intensity of 9.76×10^6 cps with the doping concentration of 8%. The coating of TiO₂ nanofilm leads the luminescence intensity of TiO₂/Li,Pr:Y₂SiO₅ composite to get down sharply, since the luminescence emitted by Li,Pr:Y₂SiO₅ is adsorbed in situ by the TiO₂ coating film. As a result, the TiO₂/Li,Pr:Y₂SiO₅ composite with 1% TiO₂, which presents a low luminescence intensity, shows the excellent photodegradation performance on nitrobenzene wastewater. For 5 mg/L of nitrobenzene wastewater, the photodegradation rate is up to 97.08% and 98.82% in 4 h and 6 h, respectively.

Conflict of Interests

The authors declare that there is no conflict of interests regarding the publication of this paper.

Acknowledgment

The work was supported by the Foundation of Jiangsu Environmental Protection Department, China (no. 2012015).

References

- [1] S. Marks, J. G. Heck, M. H. Habicht, P. Oña-Burgos, C. Feldmann, and P. W. Roesky, "[Ln(BH₄)₂(THF)₂](Ln = Eu, Yb)—a highly luminescent material. Synthesis, properties, reactivity, and NMR studies," *Journal of the American Chemical Society*, vol. 134, no. 41, pp. 16983–16986, 2012.
- [2] L. Zhang, B. Liu, and S. Dong, "Bifunctional nanostructure of magnetic core luminescent shell and its application as solid-state electrochemiluminescence sensor material," *Journal of Physical Chemistry B*, vol. 111, no. 35, pp. 10448–10452, 2007.
- [3] V. Martínez-Martínez, R. García, L. Gómez-Hortigüela, R. S. Llano, J. Pérez-Pariente, and I. López-Arbeloa, "Highly

- luminescent and optically switchable hybrid material by one-pot encapsulation of dyes into MgAPO-11 unidirectional nanopores," *ACS Photonics*, vol. 1, no. 3, pp. 205–211, 2014.
- [4] V. B. Taxak and S. P. Khatkar, "Synthesis, characterization and luminescent properties of Eu/Tb-doped LaSrAl₃O₇ nanophosphors," *Journal of Alloys and Compounds*, vol. 549, pp. 135–140, 2013.
- [5] D. Giaume, V. Buissette, K. Lahlil et al., "Emission properties and applications of nanostructured luminescent oxide nanoparticles," *Progress in Solid State Chemistry*, vol. 33, no. 2-4, pp. 99–106, 2005.
- [6] W. Wang, Q. Shang, W. Zheng et al., "A novel near-infrared antibacterial material depending on the upconverting property of Er³⁺-Yb³⁺-Fe³⁺ tridoped TiO₂ nanopowder," *Journal of Physical Chemistry C*, vol. 114, no. 32, pp. 13663–13669, 2010.
- [7] M. Wang, G. Abbineni, A. Clevenger, C. Mao, and S. Xu, "Upconversion nanoparticles: Synthesis, surface modification and biological applications," *Nanomedicine: Nanotechnology, Biology, and Medicine*, vol. 7, no. 6, pp. 710–729, 2011.
- [8] Y. Yang, C. Liu, P. Mao, and L.-J. Wang, "Upconversion luminescence and photodegradation performances of Pr doped Y₂SiO₅ nanomaterials," *Journal of Nanomaterials*, vol. 2013, Article ID 427370, 7 pages, 2013.
- [9] G. Feng, S. Liu, Z. Xiu et al., "Visible light photocatalytic activities of TiO₂ nanocrystals doped with upconversion luminescence agent," *Journal of Physical Chemistry C*, vol. 112, no. 35, pp. 13692–13699, 2008.
- [10] T. Anh, P. Benalloul, C. Barthou, L. T. Giang, N. Vu, and L. Minh, "Luminescence, energy transfer, and upconversion mechanisms of Y₂O₃ nanomaterials doped with Eu³⁺, Tb³⁺, Tm³⁺, Er³⁺, and Yb³⁺ ions," *Journal of Nanomaterials*, vol. 2007, Article ID 48247, 10 pages, 2007.
- [11] N. Nguyen, M. H. Nam, T. K. Anh, L. Q. Minh, and E. Tanguy, "Optical properties of Eu³⁺ doped Y₂O₃ nanophosphors," *Advances in Natural Sciences*, vol. 6, pp. 119–123, 2006.
- [12] J. Lin, Q. Su, S. Wang, and H. Zhang, "Influence of crystal structure on the luminescence properties of bismuth (III), europium(III) and dysprosium(III) in Y₂SiO₅," *Journal of Materials Chemistry*, vol. 6, no. 2, pp. 265–269, 1996.
- [13] M. R. Hoffmann, S. T. Martin, W. Choi, and D. W. Bahnemann, "Environmental applications of semiconductor photocatalysis," *Chemical Reviews*, vol. 95, no. 1, pp. 69–96, 1995.
- [14] K. Palmisano, V. Augugliaro, A. Sclafani, and M. Schiavello, "Activity of chromium-ion-doped titania for the dinitrogen photoreduction to ammonia and for the phenol photodegradation," *Journal of physical chemistry*, vol. 92, no. 23, pp. 6710–6713, 1988.
- [15] B. Neumann, P. Bogdanoff, H. Tributsch, S. Sakthivel, and H. Kisch, "Electrochemical mass spectroscopic and surface photovoltage studies of catalytic water photooxidation by undoped and carbon-doped titania," *Journal of Physical Chemistry B*, vol. 109, no. 35, pp. 16579–16586, 2005.
- [16] T. Ochiai and A. Fujishima, "Photoelectrochemical properties of TiO₂ photocatalyst and its applications for environmental purification," *Journal of Photochemistry and Photobiology C: Photochemistry Reviews*, vol. 13, no. 4, pp. 247–262, 2012.
- [17] T. Ochiai, K. Masuko, S. Tago et al., "Synergistic water-treatment reactors using a TiO₂-modified Ti-mesh filter," *Water*, vol. 5, no. 3, pp. 1101–1115, 2013.
- [18] J. M. Mwabora, T. Lindgren, E. Avendaño et al., "Structure, composition, and morphology of photoelectrochemically active TiO_{2-x}N_x thin films deposited by reactive DC magnetron sputtering," *Journal of Physical Chemistry B*, vol. 108, no. 52, pp. 20193–20198, 2004.
- [19] L. Liu, C. Zhao, and F. Yang, "TiO₂ and polyvinyl alcohol (PVA) coated polyester filter in bioreactor for wastewater treatment," *Water Research*, vol. 46, no. 6, pp. 1969–1978, 2012.
- [20] S. Yang, J.-S. Gu, H.-Y. Yu et al., "Polypropylene membrane surface modification by RAFT grafting polymerization and TiO₂ photocatalysts immobilization for phenol decomposition in a photocatalytic membrane reactor," *Separation and Purification Technology*, vol. 83, no. 1, pp. 157–165, 2011.
- [21] M. Farbod and M. Kajbafvala, "Effect of nanoparticle surface modification on the adsorption-enhanced photocatalysis of Gd/TiO₂ nanocomposite," *Powder Technology*, vol. 239, pp. 434–440, 2013.
- [22] J. L. Rodríguez, T. Poznyak, M. A. Valenzuela, H. Tiznado, and I. Chairez, "Surface interactions and mechanistic studies of 2,4-dichlorophenoxyacetic acid degradation by catalytic ozonation in presence of Ni/TiO₂," *Chemical Engineering Journal*, vol. 222, pp. 426–434, 2013.
- [23] W. Zhang, L. Zou, and L. Wang, "A novel charge-driven self-assembly method to prepare visible-light sensitive TiO₂/activated carbon composites for dissolved organic compound removal," *Chemical Engineering Journal*, vol. 168, no. 1, pp. 485–492, 2011.
- [24] N. Liu, X. Chen, J. Zhang, and J. W. Schwank, "A review on TiO₂-based nanotubes synthesized via hydrothermal method: formation mechanism, structure modification, and photocatalytic applications," *Catalysis Today*, vol. 225, pp. 34–51, 2014.
- [25] Q. Wang, X. Wang, X. Li, Y. Cai, and Q. Wei, "Surface modification of PMMA/O-MMT composite microfibers by TiO₂ coating," *Applied Surface Science*, vol. 258, no. 1, pp. 98–102, 2011.
- [26] D. L. Hou, H. J. Meng, L. Y. Jia, X. J. Ye, H. J. Zhou, and X. L. Li, "Oxygen vacancy enhanced the room temperature ferromagnetism in Ni-doped TiO₂ thin films," *Physics Letters A*, vol. 364, no. 3-4, pp. 318–322, 2007.
- [27] C. Hu, C. Sun, J. Li, Z. Li, H. Zhang, and Z. Jiang, "Visible-to-ultraviolet upconversion in Pr³⁺:Y₂SiO₅ crystals," *Chemical Physics*, vol. 325, no. 2-3, pp. 563–566, 2006.
- [28] C. L. Sun, J. F. Li, C. H. Hu, H. M. Jiang, and Z. K. Jiang, "Ultraviolet upconversion in Pr³⁺:Y₂SiO₅ crystal by Ar⁺ laser (488 nm) excitation," *European Physical Journal D*, vol. 39, no. 2, pp. 303–306, 2006.
- [29] G. Ramakrishna, H. Nagabhushana, D. V. Sunitha, S. C. Prashantha, S. C. Sharma, and B. M. Nagabhushana, "Effect of different fuels on structural, photo and thermo luminescence properties of solution combustion prepared Y₂SiO₅ nanopowders," *Spectrochimica Acta A: Molecular and Biomolecular Spectroscopy*, vol. 127, pp. 177–184, 2014.
- [30] L. Jia, Z. Shao, Q. Lü, Y. Tian, and J. Han, "Optimum europium doped aluminoborates phosphors and their photoluminescence properties under VUV and UV excitation," *Optics and Laser Technology*, vol. 54, pp. 79–83, 2013.
- [31] K. Nakata, T. Ochiai, T. Murakami, and A. Fujishima, "Photoenergy conversion with TiO₂ photocatalysis: new materials and recent applications," *Electrochimica Acta*, vol. 84, pp. 103–111, 2012.

- [32] X. Fu, J. Ji, W. Tang, W. Liu, and S. Chen, "Mo-W based copper oxides: Preparation, characterizations, and photocatalytic reduction of nitrobenzene," *Materials Chemistry and Physics*, vol. 141, no. 2-3, pp. 719–726, 2013.
- [33] S. A. V. Eremia, D. Chevalier-Lucia, G.-L. Radu, and J.-L. Marty, "Optimization of hydroxyl radical formation using TiO_2 as photocatalyst by response surface methodology," *Talanta*, vol. 77, no. 2, pp. 858–862, 2008.

Research Article

Actual Application of a H₂-Based Polyvinyl Chloride Hollow Fiber Membrane Biofilm Reactor to Remove Nitrate from Groundwater

Yanhao Zhang,^{1,2} Lilong Huang,¹ Zhibin Zhang,¹ Cuizhen Sun,¹ and Jixiang Li³

¹School of Municipal and Environmental Engineering, Shandong Jianzhu University, Jinan 250101, China

²State Key Laboratory of Pollution Control and Resource Reuse, Tongji University, Shanghai 200092, China

³Sustainable Technology Research Center, Shanghai Advanced Research Institute, Chinese Academy of Sciences, Shanghai 201210, China

Correspondence should be addressed to Zhibin Zhang; zhazhb@163.com

Received 24 April 2014; Accepted 27 October 2014

Academic Editor: Tian C. Zhang

Copyright © 2015 Yanhao Zhang et al. This is an open access article distributed under the Creative Commons Attribution License, which permits unrestricted use, distribution, and reproduction in any medium, provided the original work is properly cited.

To evaluate the actual performance of the H₂-based polyvinyl chloride hollow fiber membrane biofilm reactor (HF-MBfR), we used HF-MBfR to remove nitrate from the nitrate contaminated groundwater with the dissolved oxygen (~6.2 mg/L) in Zhangqiu city (Jinan, China). The reactor was operated over 135 days with the actual nitrate contaminated groundwater. The result showed that maximum of nitrate denitrification rate achieved was over 133.8 g NO₃⁻-N/m³d (1.18 g NO₃⁻-N/m²d) and the total nitrogen removal was more than 95.0% at the conditions of influent nitrate 50 mg/L, hydrogen pressure 0.05 MPa, and dissolved oxygen (DO) 6.2 mg/L, with the nitrate in effluent under the value limits of drinking water. The fluxes analysis showed that the electron-equivalent fluxes of nitrate, sulfate, and oxygen account for about 81.2%, 15.2%, and 3.6%, respectively, which indicated that nitrate reduction could consume more electrons than that of sulfate reduction and dissolved oxygen reduction. The nitrate reduction was not significantly influenced by sulfate reduction and the dissolved oxygen reduction. Based on the actual groundwater quality on site, the Langelier Saturation Index (LSI) was 0.4, and the membrane could be at the risk of surface scaling.

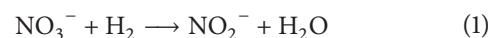
1. Introduction

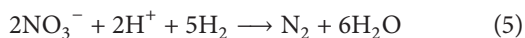
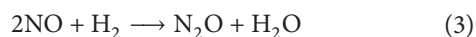
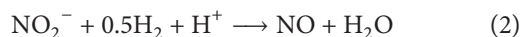
Currently, nitrate contamination of drinking water supplies has become a serious problem in the world. If the level of nitrate in water exceeds 10 mg N/l (WHO), methemoglobinemia in infants or blue baby syndrome would occur, and nitrosamines, that is, potential carcinogenic metabolites of nitrate, would be formed [1–3].

The best available technologies (BAT) for NO₃⁻ removal from drinking water include ion exchange [4], reverse osmosis [5], and electrodialysis [6, 7]. However, the utilities of these processes were limited due to their expensive operation and subsequent disposal problem of the generated nitrate waste brine [8]. Biological denitrification is carried out by facultative bacteria that can use NO₃⁻ as a terminal electron acceptor for respiration under anoxic conditions. The microorganisms that participated in the processes (i.e.,

heterotrophic denitrification and autotrophic denitrification) are genetically diverse and metabolically versatile [9]. Basically, organic substrates such as methanol or ethanol were used in the process of heterotrophic denitrification because organic carbon concentrations in drinking water are very low [10]. Therefore, the cost increases and the second pollutions also could appear.

Autotrophic denitrification using hydrogen as the supplemental donor has been extensively investigated to remove nitrate from polluted drinking water or waste water [11–14]. The autohydrogenotrophic denitrifiers are able to respire on NO₃⁻-N in the absence of molecular oxygen. Otherwise, hydrogen is cheaper and nontoxic and of lower biomass yield and without a residual [15, 16]. The following equations could describe the stoichiometry of hydrogenotrophic denitrification [15]:





Using hydrogen to reduce nitrate or other oxidants in water had been studied through sparging gas or bubbleless gas [11, 13, 17]. Due to the danger of explosion and low hydrogen utilization for the sparging methods, bubbleless gas-permeable membrane technology has developed to a promising way to reduce nitrate. Bubbleless gas-permeable membranes had been studied before including different composite membrane, including nonporous polyurethane layers [17], polypropylene [18], silicone-coated reinforced fiberglass fibers [16], and silicone-coated ferronickel slag [19]. The nitrate reducing processes normally could achieve a good effect of denitrification in the absence of oxygen, because of the oxygen always being a competitor for the electron acceptors. Therefore, most of the hydrogenotrophic denitrification processes were operated in the absence of oxygen in laboratories, while, for the nitrate contaminated drinking water, including surface water or shallow groundwater, dissolved oxygen (DO) is often present in the contaminated waters and is the favored electron acceptor for hydrogen oxidizing bacteria. On the other hand, membrane fouling is not clear in the MBfR, although there are lots of studies about membrane fouling on membrane bioreactor (MBR), while, in MBR it is the contaminated water with SS that goes through the micropores of the membrane in order to get purified water or to hold back the particles. However, in MBfR it is the pressured hydrogen that goes through the membrane pores to provide the hydrogen for utilization by the hydrogenotrophic bacteria on the membrane surface. Therefore, the fouling mechanisms are different for MBR and MBfR. Otherwise, there are still some problems that limited the application for the MBfR, such as the inconvenient hydrogen supply and lower hydrogen utilization rate.

The objective of this study was to investigate the actual performance of polyvinyl chloride (PVC) membrane biofilm reactor for removing nitrate from groundwater, especially to assess the influences of DO and membrane fouling on the process.

2. Materials and Methods

2.1. Membrane Biofilm Reactor. The HF-MBfR used in this study is shown in Figure 1. A transparent plastic cylinder was used as a hollow fiber membrane reactor, in which two membrane modules were directly submerged in the bulk fluid and gas sealed with the plastic ring and the cap of the reactor (Figure 1). The reactor was 22 cm in height and 6 cm in inner diameter. The system made the feed-media mix well in the biofilm reactor because the stirring power was generated by a magnetic stirrer set in the bottom of the reactor. The hollow fibers were made of PVC with pore size of $0.01 \mu\text{m}$, manufactured by Litree Company (Suzhou, China). The outside and inner diameters of the fiber are 0.15 and

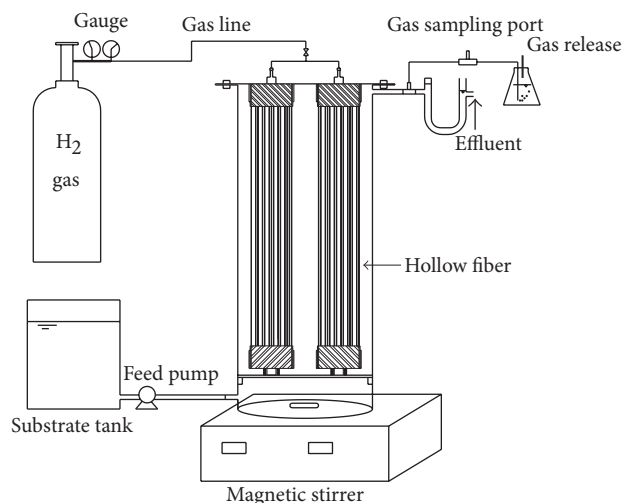


FIGURE 1: Schematic of the MBfR.

0.085 cm, respectively, which provides 633.3 cm^2 of surface area with total 96 hollow fibers (each module consisted of 48 hollow fibers). The total available volume of the reactor system was 560 mL. The void ratio of the working reactor volume (volume of fiber was 23.7 mL) was 95.8%. A single peristaltic pump (Longer BT50-1J, Baoding, China) was used to keep a nitrate-medium-feed rate of 1.1 mL/min. Pure H_2 was supplied to the inside hollow fibers through a H_2 gas tank via a metering valve.

2.2. Influent of Nitrate Contaminated Shallow Groundwater.

In the present study, the feeding medium was taken from the groundwater in the vegetable land at the suburb of Zhangqiu city (Jinan, China), where a lot of fertilizers had been used in the lands. Therefore, the shallow groundwater around the vegetable land had been contaminated by nitrate, and the water quality was shown in Table 1.

2.3. Start-Up and Experimental Conditions.

Start-up of the continuous stirred MBfR began when hydrogen was supplied to the membrane under the hydrogen pressure of 0.03 MPa, and the MBfR had been acclimated for several months in our laboratory. The flow rate was 1.1 mL/min with the HRT 8.5 h, and the MBfR was operated over 135 days. To reduce the influent shock loading for the biofilm, the pumped groundwater had been diluted by tap water. The detailed operation conditions of the reactor were listed in Table 2.

2.4. Analytical Method.

All the fluid samples collected from the reactor were kept in the refrigerator at 4°C and analyzed within 2 days. The concentrations of $\text{NO}_3^- \text{-N}$, $\text{NO}_2^- \text{-N}$, and SO_4^{2-} , hardness, alkalinity, TDS, and pH value were analyzed according to Chinese NEPA standard methods [20]. DO was measured by a DO probe (Hach, HQ40d). The gas sample in the headspace of the reactor was taken by inserting a gas-tight syringe through the rubber stopper on the gas-sampling port. The gas concentrations were measured by a GC 14-B equipped with a TCD detector (Shimadzu Co.). The liquid

TABLE 1: Water quality for the groundwater.

Total dissolved solids (mg/L)	pH	DO (mg/L)	Alkalinity (mg/L as CaCO ₃)	Hardness (mg/L as CaCO ₃)	Nitrate (mg N/L)	Nitrite (mg N/L)	Sulfate (mg/L)
300–400	7.5~7.8	5.5~6.5	400~600	150~250	45~55	ND	80~90

TABLE 2: Operation conditions of the membrane biofilm reactor.

	Run I	Run II	Run III
Operation period (day)	1–36	37–81	82–135
H ₂ pressure (MPa)	0.03	0.04	0.05
Influent NO ₃ ⁻ -N (mg/L)	20.0 ± 2.0	40.0 ± 4.0	50.0 ± 4.0
Hydraulic retention time (h)		8.5	

phase concentrations of H₂ in the reactor were calculated by H₂ headspace concentrations using Henry's law.

For the SEM experiment, a part of a new control PVC membrane fiber was obtained by a sterile shaver and cleaned with distilled water and then dried and coated with Au/Pb in order to enhance the quality of the images. After the preparation, the fiber was examined by scanning electron microscope (SEM, XL-30, Philips, Netherlands). The samples of fiber at running stages were checked by SEM using the same methods without the preparation of washing [21, 22].

3. Results and Discussion

3.1. Denitrification Performance of Continuous Stirred MBfR.

Under the condition of HRT 8.5 h, the influent concentrations of nitrate ranged from 20 to 50 mg N/L (Table 1), and the influent concentrations of sulfate ranged from 40 to 90 mg SO₄²⁻/L through the experiments with the hydrogen pressure varied from 0.03 to 0.05 MPa. In Run I of the first 36 days, the biofilm was successfully switched to the new influent from the synthetic influent and the concentrations of nitrate and sulfate in the effluent dropped gradually to 0.3 mg N/L and 24.0 mg SO₄²⁻/L, respectively, and the nitrite was not detected in the final phase of the periods (Figure 2). Although the DO in the influent was maintained at about 6.2 ± 0.3 mg/L, the TN removal also reached about 98.3 ± 2.5%, and the effluent DO was about 0.2 mg/L, which indicated that the electron acceptor nitrate and oxygen could get hydrogen electron donor easier than sulfate.

At Run II and Run III, the hydrogen pressures were adjusted to 0.04 and 0.05 MPa, respectively, and the influent nitrate was adjusted to 40 and 50 mg N/L. The results showed that the average removal efficiencies of nitrate in Runs I and II were 98.8% and 95.1%, respectively. In the effluent, the average of residual nitrate concentrations was about 0.5 and 0.6 mg N/L, respectively, and the concentrations of nitrite were about 0.3 mg N/L, which does not exceed regulatory level of 1.0 mg N/L (WHO).

The influent nitrate and sulfate loading and volumetric denitrification and sulfate reduction were shown in Figures 3 and 4, respectively.

From Run I to Run III, the average nitrate volumetric loading rate increased from 56.5 to 139.5 g N/m³d, and the

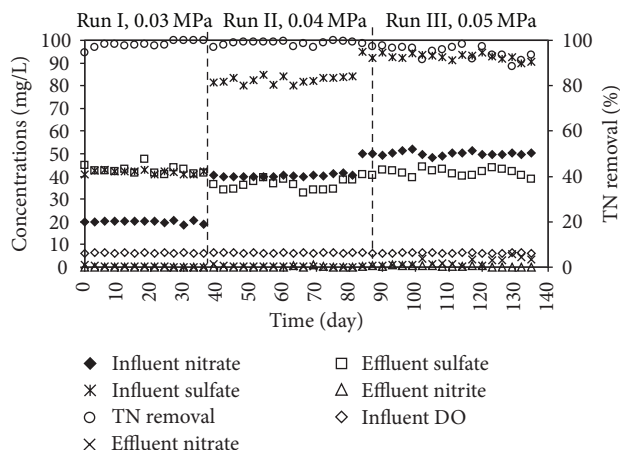


FIGURE 2: The nitrate, nitrite, sulfate, DO, and TN removal in the continuous experiments.

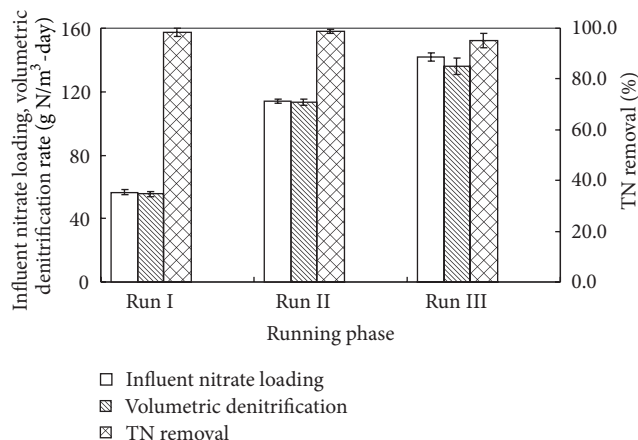


FIGURE 3: Influent nitrate loading, volumetric denitrification rate, and TN removal in the experiment. Error bars represent the standard deviation between continuous samples during one running phase.

average volumetric denitrification rates were 55.5, 131.1, and 139.5, respectively, which corresponded to average surface denitrification rates of 0.49, 0.98, and 1.18 g N/m²d, respectively. The average TN removal rate at Run I to Run III reached 98.3%, 98.8%, and 95.0%, respectively, while, at influent of 12.5 mg NO₃⁻-N/L and hydrogen pressure of 0.42 atm, Lee and Rittmann [17] achieved 1.0 g N/m²d using the MBfR with 1-micron thick layer of nonporous polyurethane with microporous polyethylene on the inner and outer sides. With the same materials as that of Rittmann, a denitrification rate of 1.4 g N/m²d was got by Shin et al. [23] using a serial MBfR (nitrification and denitrification) under the condition

TABLE 3: Electronic-equivalent fluxes for sulfate and nitrate.

Period	Denitrification rate or substrate flux ^a			Electron-equivalent flux (eq/m ² d)				Distribution of electron-equivalent fluxes (%)		
	Nitrate (g/m ² d)	Sulfate (g SO ₄ ²⁻ /m ² d)	O ₂ (g/m ² d)	Nitrate ^b	Sulfate ^c	O ₂ ^d	Sum-up of the fluxes	Nitrate	Sulfate	O ₂
Run I	0.49	0.45	0.15	0.18	0.04	0.02	0.23	76.0	15.9	8.1
Run II	0.98	0.75	0.15	0.35	0.06	0.02	0.43	81.5	14.2	4.3
Run III	1.18	0.97	0.15	0.42	0.08	0.02	0.52	81.2	15.2	3.6

^aCalculated by $J_{\text{substrate}} = (\text{influent flow rate } (Q) \times \text{removed substrate } (\Delta S)) / (\text{area of biofilm surface } (A_B))$, where Q is in m³/d, ΔS is in g-substrate (NO₃⁻-N or SO₄²⁻)/m³, A_B is in m², and J is in g-NO₃⁻-N/m²d or g-SO₄²⁻/m²d.

^bCalculated by $J_{e-\text{NO}_3^-} = (\text{influent flow rate } (Q) \times \text{removed NO}_3^- \text{-N } (\Delta S)) / (\text{area of biofilm surface } (A_B) \times \text{EW}_{\text{Nitrate}})$, where Q is in m³/d, ΔS is in g-NO₃⁻-N/m³, A_B is in m², $\text{EW}_{\text{Nitrate}}$ is in 14 g-NO₃⁻-N/5 e⁻ equivalent for reduction of nitrate to nitrogen gas, and J is in g-NO₃⁻-N/m²d. We assume five electrons per mole for nitrate reduction to nitrogen gas.

^cCalculated by $J_{e-\text{SO}_4^{2-}} = (\text{influent flow rate } (Q) \times \text{removed SO}_4^{2-} (\Delta S)) / (\text{area of biofilm surface } (A_B) \times \text{EW}_{\text{Sulfate}})$, where Q is in m³/d, ΔS is in g-SO₄²⁻/m³, A_B is in m², $\text{EW}_{\text{Sulfate}}$ is in 96 g-NO₃⁻-N/8 e⁻ equivalent for reduction of sulfate to sulfide, and J is in g-SO₄²⁻/m²d. We assume 8 electrons per mole for sulfate reduction to sulfide, for seen $\text{SO}_4^{2-} + 4\text{H}_2 + 1.5\text{H}^+ \rightarrow 0.5\text{H}_2\text{S} + 0.5\text{HS}^- + 4\text{H}_2\text{O}$ (i) [26].

^dCalculated by $J_{e-\text{O}_2} = (\text{influent flow rate } (Q) \times \text{removed O}_2 (\Delta S)) / (\text{area of biofilm surface } (A_B) \times \text{EW}_{\text{Oxygen}})$, where Q is in m³/d, ΔS is in g-O₂/m³, A_B is in m², $\text{EW}_{\text{Oxygen}}$ is in 32 g-O₂/4 e⁻ equivalent for reduction of O₂ to O²⁻, and J is in g-O₂/m²d. We assume 4 electrons per mole for reduction O₂ to O²⁻, for seen $\text{O}_2 + 4\text{H}^+ \rightarrow 2\text{H}_2\text{O}$ (ii).

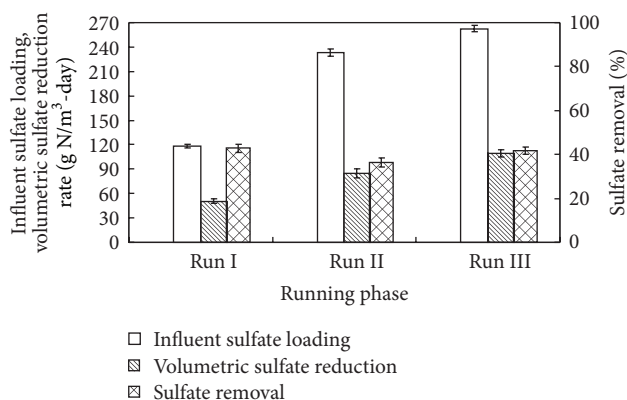


FIGURE 4: Influent sulfate loading, volumetric sulfate reduction rate, and sulfate removal in the experiment. Error bars represent the standard deviation between continuous samples during one running phase.

of influent nitrate concentration of 51 mg N/L and hydrogen pressure of 4 psi (about 0.3 atm). The influent sulfate loading was varied from 118.5, 233.3, and 262.6 mg SO₄²⁻/L, with the sulfate reduction loading rates of 50.7, 84.6, and 109.6 mg SO₄²⁻/L, respectively. And the sulfate removals were 42.8%, 36.2%, and 41.8%, respectively, for the three phases.

3.2. Flux Analysis. Table 3 showed the average values of substrate fluxes and electron-equivalent fluxes for all the electron acceptors, along with the percentage distribution of each flux. With the increasing of influent nitrate concentrations, the oxygen flux reduced. For the distribution of electron-equivalent fluxes, with the influent nitrate concentration increasing, the nitrate fluxes and sulfate fluxes increased, while the O₂ fluxes contained a constant with the effluent DO that was near zero. The results indicated that the autotrophic

denitrifiers could utilize DO and nitrate preferentially rather than sulfate. On the other hand, the electron-equivalent fluxes of the nitrate accounted for more than 80% at Run II and Run III, while the electron-equivalent fluxes of sulfate and oxygen account for about 14.2% and 4.3%, respectively, at Run II; the electron-equivalent fluxes of sulfate and oxygen account for about 15.2% and 3.6%, respectively, at Run III. Therefore, with the influent nitrate loading increasing, the oxygen electron-equivalent fluxes decreased, which indicated that the 6.0 mg/L of DO concentration did not affect the nitrate removing from the groundwater [24].

The DO, nitrite, and nitrate in the effluent were very low, while the sulfate in the effluent was about half of its influent concentrations. The results about the sulfate reduction rate were consistent with those reported by Terada et al. [19]; they used a membrane-fibrous composite matrix (a poly membrane tube of dimethylsiloxane and silicone inner and a fibrous support covered the surface of the tube) to immobilize autohydrogenotrophic denitrifying bacteria in the reactor, and they found that, with the hydrogen pressure increased up to 50 kPa, only approximately 50% of sulfate was reduced by SRB. Zhao et al. [25] also reported that the nitrate and oxygen surface loading greater than 0.34 g H₂/m²·d could suppress the sulfate reduction in MBfR; that is, an appropriate range of nitrate and oxygen surface loading is essential to reduce other oxidized contaminants, such as chlorate and sulfate. The results mean the nitrate and oxygen were easier to get electrons than sulfate when the three electron acceptors were sufficient in autohydrogenotrophic denitrification processes [26].

3.3. Hydrogen Utilization. From Table 3, we can see that hydrogen consumption was mainly attributed to nitrate and sulfate reduction. According to Lee and Rittmann [15], with analyzing the hydrogen utilization of the system, the mass

balances of hydrogen, nitrate, nitrite, and sulfate in the autohydrogenotrophic biofilm were built under the fundamental assumptions. The assumptions are as follows: the substrate utilized by the suspended biomass is ignored and biomass is not included in the mass balances. Since hydrogen utilization for denitrification, sulfate reduction, and oxygen reduction follows the stoichiometry described in (1)–(5) and (i) and (ii) of Table 3, the sum of hydrogen consumption rates during denitrification and sulfate reduction by the biofilm ($R_{H,B}$, mg H_2/cm^3d) can be described by the following and the hydrogen flux ($J_{H,T}$, mg H_2/cm^2d) can be described by the following:

$$R_{H,B}V = \alpha_{H,3}Q(S_{3,i} - S_{3,o}) + \alpha_{H,2}\alpha_{2,3}Q(S_{3,i} - S_{3,o}) + \alpha_{H,4}Q(S_{4,i} - S_{4,o}) + \alpha_{H,5}Q(S_{5,i} - S_{5,o}) \quad (6)$$

$$- \alpha_{H,2}QS_{2,o},$$

$$J_{H,T}A_B = R_{H,B}V + QS_{H,o}, \quad (7)$$

where $R_{H,B}$ is the rate of hydrogen utilization by the biofilm (mg H_2/cm^3d). $\alpha_{H,3}$ is the stoichiometric consumption ratio of hydrogen to nitrate during nitrate reduction (mg H_2/mg N), $\alpha_{H,2}$ is the stoichiometric consumption ratio of hydrogen to nitrite during nitrite reduction to N_2 gas (mg H_2/mg N), and $\alpha_{H,4}$ is the stoichiometric consumption ratio of hydrogen to sulfate during sulfate reduction to sulfide (mg H_2/mg SO_4^{2-}). Based on the stoichiometric reactions of (1) to (5) and (i) and (ii) of Table 3, $\alpha_{H,3}$, $\alpha_{H,2}$, $\alpha_{H,4}$, and $\alpha_{H,5}$ are 0.143, 0.214 mg H_2/mg N, and 0.083 mg H_2/mg SO_4^{2-} and 0.215 mg H_2/mg O_2 , respectively. $\alpha_{2,3}$ is the stoichiometric coefficient for the production of nitrite from nitrate to nitrite, which is equal to 1 mg N/mg N. A_B is the biofilm surface area (cm^2), Q is the influent flow rate of the reactor system (l/d), and V is the volume of the reactor (cm^3). $S_{3,i}$ and $S_{3,o}$ are the nitrate concentrations in the influent and the effluent, respectively (mg N/L); $S_{4,i}$ and $S_{4,o}$ are the sulfate concentrations in the influent and the effluent, respectively (mg SO_4^{2-}/L); $S_{5,i}$ and $S_{5,o}$ are the DO concentrations in the influent and the effluent, respectively (mg O_2/L); $S_{H,o}$ is hydrogen concentration in the effluent (mg H_2/L). Then, the rate of hydrogen utilization by the biofilm, the hydrogen concentration in the effluent, and the hydrogen flux in the experiment are demonstrated in Figure 5.

In Run III, the average rate of hydrogen utilization by biofilm was better than that of Run I and Run II, that is, 0.060 mg H_2/cm^3d (0.034 mg H_2/cm^2d) (Figure 5). The results showed that the hydrogen utilization rate increased with the increasing of influent nitrate loading, which indicated this hydrogen pressure (or hydrogen flux) was enough to remove the nitrate from the groundwater, and there still was a potential for a higher influent nitrate loading. These results were consistent with those reported by Lee and Rittmann [15], and Figure 5 also illustrates the effluent hydrogen concentration decreased as the nitrate loading increased and then leveled off at the last running stages, averaged $121 \pm 49 \mu g/L$ in Run III. This result indicated that the nitrate loading limitation for autohydrogenotrophic

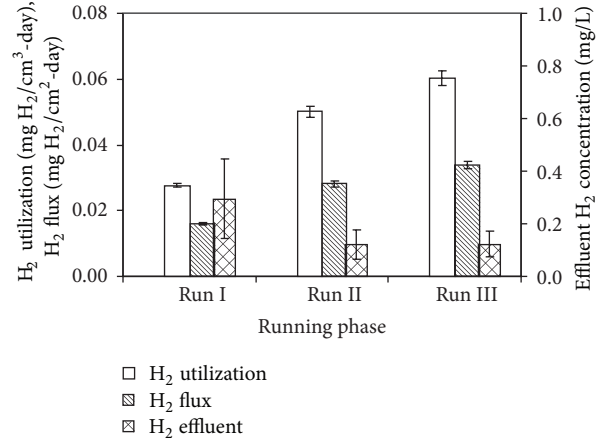


FIGURE 5: Average rate of hydrogen utilization by the biofilm, average hydrogen concentration in the effluent, and average hydrogen flux at different experimental periods.

TABLE 4: The H_2 utilization in the MBfR.

	Sum of H_2 utilization (%)	H_2 utilization for NO_3^- (%)	H_2 utilization for SO_4^{2-} (%)	H_2 utilization for O_2 (%)
Run I	96.9 ± 1.6	81.0 ± 1.6	15.9 ± 0.7	12.0 ± 0.4
Run II	99.3 ± 0.3	85.3 ± 0.9	14.0 ± 0.9	6.8 ± 0.3
Run III	99.4 ± 0.2	84.4 ± 0.9	15.0 ± 0.8	6.0 ± 0.4

denitrification was transitioned to hydrogen limitation at the stage of effluent hydrogen concentration leveling off, and hydrogen utilization rate was not influenced by sulfate and DO.

The percent unutilized hydrogen was calculated as the ratio of H_2 leaving in the effluent divided by the H_2 used for nitrate reduction, nitrite reduction, sulfate reduction, oxygen reduction, and loss to the effluent, as shown in (8). Based on the percent unutilized hydrogen in the experiment, the percent utilized hydrogen could be calculated correspondingly. The results were shown in Table 4.

The hydrogen utilization efficiency in Run I was about $96.9 \pm 1.6\%$, a little bit lower than that of Run II and Run III, which could be explained by the fact that the influent nitrate loading was lower, and the nitrate loading should be the limiting factor for denitrification at Run I:

$$\begin{aligned} \%H_2 \text{ unutilized} &= 100\% \times (S_{H,o}) \\ &\times (0.143(S_{3,i} - S_{3,o}) + 0.214(S_{3,i} - S_{3,o} - S_{2,o}) \\ &+ 0.083(S_{4,i} - S_{4,o}) + 0.125(S_{5,i} - S_{5,o}) + S_{H,o})^{-1}. \end{aligned} \quad (8)$$

3.4. Membrane Scaling Potential. At the denitrification process, the pH will increase because of alkalinity production (5), which can result in precipitation of $CaCO_3$ on the fibers [15, 27], blocking the pores of the membranes and limiting

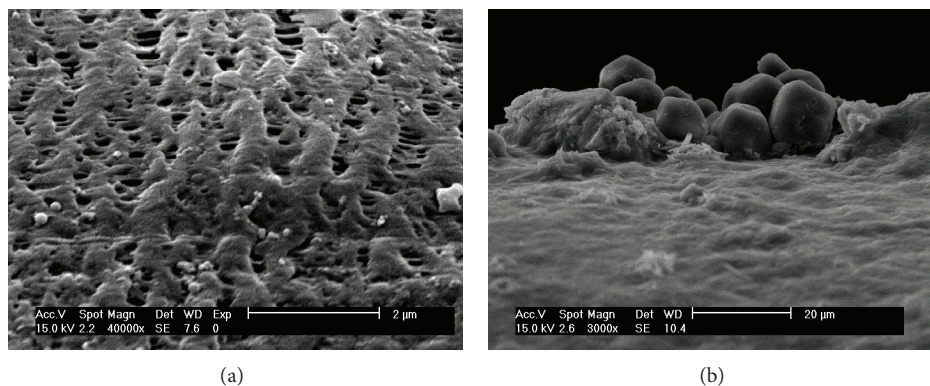


FIGURE 6: The scanning electron micrograph of control hollow fiber membrane surface (a) and polluted membrane from MBfR (b).

H₂ transfer across the micropores of the membrane. The membrane scaling potential by CaCO₃ was analyzed by the Langelier Saturation Index (LSI), which indicated whether or not the water was supersaturated:

$$\text{LSI} = \text{pH}_a - \text{pH}_s, \quad (9)$$

where pH_a is the measured pH and pH_s is the theoretical pH of the water if it were in equilibrium with CaCO₃ and calculated as

$$\text{pH}_s = \text{pK}_{a,\text{HCO}_3^-} - \text{pK}_{\text{SO}} + \text{p}[\text{Ca}^{2+}] + \text{p}[\text{HCO}_3^-] \quad (10)$$

$$- \log r_{\text{Ca}^{2+}} - \log r_{\text{HCO}_3^-}, \quad (11)$$

$$I = 2.5 \times 10^{-5} \times \text{TDS} \quad (12)$$

in which pK_{a,HCO₃⁻} is the HCO₃⁻ acid dissociation constant (10^{-10.33} at 25°C), K_{SO} is the solubility product for CaCO₃ (10^{-8.34} at 25°C), and [Ca²⁺] is measured alkalinity (M). r_{Ca²⁺} and r_{HCO₃⁻} are the activity coefficients for Ca²⁺ and HCO₃⁻, respectively. I is the ionic strength in mg/L.

Based on the average influent water quality of pH 7.6, TDS 300 mg/L, alkalinity 510 mg/L (as CaCO₃), and hardness 200 mg/L (as CaCO₃), the LSI was 0.4 in the effluent calculated by the above equations, which indicated that the membrane was at the risk of surface scaling. The LSI values were a little higher than that (LSI, 0.11 in the effluent) of the report by Ziv-El and Rittmann [24] who used MBfR to reduce the perchlorate from the groundwater, based on the groundwater of pH 7.5, DO 7.9 mg/L, alkalinity 230 mg CaCO₃/L, TDS 490 mg/L, and hardness 410 mg CaCO₃/L. For the MBfR running successfully, CO₂ was added to the reactor to lower the pH to prevent precipitation, even though the SEM of the biofilm at Run III showed that there was some membrane fouling (Figure 6). From Figure 6, the membrane micropores of the control fiber were homogenous (Figure 6(a)), while the precipitation particles at membrane fiber got at 130d were obvious.

4. Conclusion

From the 135 days of operations, the results showed that the continuous stirred PVC MBfR could remove nitrate effectively from the groundwater on site. The average denitrification rates of 133.8 g NO₃⁻-N/m²d (1.18 g NO₃⁻-N/m²d) were achieved at influent nitrate concentration 50 mg N/L and hydrogen pressure 0.05 MPa. The fluxes analysis showed that the electron-equivalent fluxes of sulfate and oxygen account for about 15.2% and 3.6%, respectively, at the conditions of actual influent, which indicated that nitrate reduction could consume more electrons than that of sulfate reduction and dissolved oxygen reduction. The nitrate reduction was not significantly influenced by sulfate reduction and the dissolved oxygen reduction. Based on the actual quality on site, the membrane could be at the risk of surface scaling; therefore, the reactor should be considered as the scaling control in the operation application.

Conflict of Interests

The authors declare that there is no conflict of interests regarding the publication of this paper.

Acknowledgments

This research was supported fancily by the Natural Science Foundation of Shandong Province (no. BS2013HZ028) and the State Key Laboratory of Pollution Control and Resource Reuse Foundation (no. PCRRF12017). The authors thank the Department of Environmental Protection of Shandong Province (no. SDHBYF-2012-14) and the National Natural Science Foundation of China (no. 51408588) for their kind support.

References

- [1] D. C. Bouchard, M. K. Williams, and R. Y. Surampalli, "Nitrate contamination of groundwater: sources and potential health effects," *The American Water Works Association*, vol. 84, no. 9, pp. 85–90, 1992.

- [2] Q. Wang, C. Feng, Y. Zhao, and C. Hao, "Denitrification of nitrate contaminated groundwater with a fiber-based biofilm reactor," *Bioresource Technology*, vol. 100, no. 7, pp. 2223–2227, 2009.
- [3] D. J. Wan, H. J. Liu, X. Zhao, J. H. Qu, S. H. Xiao, and Y. Hou, "Role of the Mg/Al atomic ratio in hydrotalcite-supported Pd/Sn catalysts for nitrate adsorption and hydrogenation reduction," *Journal of Colloid and Interface Science*, vol. 332, no. 1, pp. 151–157, 2009.
- [4] B.-U. Bae, Y.-H. Jung, W.-W. Han, and H.-S. Shin, "Improved brine recycling during nitrate removal using ion exchange," *Water Research*, vol. 36, no. 13, pp. 3330–3340, 2002.
- [5] J. J. Schoeman and A. Steyn, "Nitrate removal with reverse osmosis in a rural area in South Africa," *Desalination*, vol. 155, no. 1, pp. 15–26, 2003.
- [6] A. El Midaoui, F. Elhannouni, M. Taky et al., "Optimization of nitrate removal operation from ground water by electro dialysis," *Separation and Purification Technology*, vol. 29, no. 3, pp. 235–244, 2002.
- [7] J. W. Peel, K. J. Reddy, B. P. Sullivan, and J. M. Bowen, "Electrocatalytic reduction of nitrate in water," *Water Research*, vol. 37, no. 10, pp. 2512–2519, 2003.
- [8] M. Shrimali and K. P. Singh, "New methods of nitrate removal from water," *Environmental Pollution*, vol. 112, no. 3, pp. 351–359, 2001.
- [9] R. L. Smith, M. L. Ceazan, and M. H. Brooks, "Autotrophic, hydrogen-oxidizing, denitrifying bacteria in groundwater, potential agents for bioremediation of nitrate contamination," *Applied and Environmental Microbiology*, vol. 60, no. 6, pp. 1949–1955, 1994.
- [10] M. A. Gómez, E. Hontoria, and J. González-López, "Effect of dissolved oxygen concentration on nitrate removal from groundwater using a denitrifying submerged filter," *Journal of Hazardous Materials*, vol. 90, no. 3, pp. 267–278, 2002.
- [11] D. Dries, J. Liessens, W. Verstraete, P. Stevens, P. De Vos, and J. De Ley, "Nitrate removal from drinking water by means of hydrogenotrophic denitrifiers in a polyurethane carrier reactor," *Water Supply*, vol. 6, no. 3, pp. 181–192, 1988.
- [12] A. Kapoor and T. Viraraghavan, "Nitrate removal from drinking water—review," *Journal of Environmental Engineering*, vol. 123, no. 4, pp. 371–380, 1997.
- [13] M. Kurt, I. J. Dunn, and J. R. Bourne, "Biological denitrification of drinking water using autotrophic organisms with H₂ in a fluidized-bed biofilm reactor," *Biotechnology and Bioengineering*, vol. 29, no. 4, pp. 493–501, 1987.
- [14] H. Hasar, "Simultaneous removal of organic matter and nitrogen compounds by combining a membrane bioreactor and a membrane biofilm reactor," *Bioresource Technology*, vol. 100, no. 10, pp. 2699–2705, 2009.
- [15] K.-C. Lee and B. E. Rittmann, "Applying a novel autohydrogenotrophic hollow-fiber membrane biofilm reactor for denitrification of drinking water," *Water Research*, vol. 36, no. 8, pp. 2040–2052, 2002.
- [16] K. S. Haugen, M. J. Semmens, and P. J. Novak, "A novel in situ technology for the treatment of nitrate contaminated groundwater," *Water Research*, vol. 36, no. 14, pp. 3497–3506, 2002.
- [17] K.-C. Lee and B. E. Rittmann, "A novel hollow-fibre membrane biofilm reactor for autohydrogenotrophic denitrification of drinking water," *Water Science and Technology*, vol. 41, no. 4–5, pp. 219–226, 2000.
- [18] S. J. Ergas and A. F. Reuss, "Hydrogenotrophic denitrification of drinking water using a hollow fibre membrane bioreactor," *Journal of Water Supply: Research and Technology*, vol. 50, no. 3, pp. 161–171, 2001.
- [19] A. Terada, S. Kaku, S. Matsumoto, and S. Tsuneda, "Rapid autohydrogenotrophic denitrification by a membrane biofilm reactor equipped with a fibrous support around a gas-permeable membrane," *Biochemical Engineering Journal*, vol. 31, no. 1, pp. 84–91, 2006.
- [20] NEPA, *Water and Wastewater Monitoring Methods*, Chinese Environmental Science Publishing House, Beijing, China, 2002.
- [21] Y. Zhang, F. Zhong, S. Xia, X. Wang, and J. Li, "Autohydrogenotrophic denitrification of drinking water using a polyvinyl chloride hollow fiber membrane biofilm reactor," *Journal of Hazardous Materials*, vol. 170, no. 1, pp. 203–209, 2009.
- [22] S. Xia, Y. Zhang, and F. Zhong, "A continuous stirred hydrogen-based polyvinyl chloride membrane biofilm reactor for the treatment of nitrate contaminated drinking water," *Bioresource Technology*, vol. 100, no. 24, pp. 6223–6228, 2009.
- [23] J. H. Shin, B. I. Sang, Y. C. Chung, and Y. K. Choung, "A novel CSTR-type of hollow fiber membrane biofilm reactor for consecutive nitrification and denitrification," *Desalination*, vol. 221, no. 1–3, pp. 526–533, 2008.
- [24] M. C. Ziv-El and B. E. Rittmann, "Systematic evaluation of nitrate and perchlorate bioreduction kinetics in groundwater using a hydrogen-based membrane biofilm reactor," *Water Research*, vol. 43, no. 1, pp. 173–181, 2009.
- [25] H.-P. Zhao, A. Ontiveros-Valencia, Y. Tang et al., "Using a two-stage hydrogen-based membrane biofilm reactor (MBfR) to achieve complete perchlorate reduction in the presence of nitrate and sulfate," *Environmental Science and Technology*, vol. 47, no. 3, pp. 1565–1572, 2013.
- [26] J. Chung, R. Nerenberg, and B. E. Rittmann, "Bioreduction of selenate using a hydrogen-based membrane biofilm reactor," *Environmental Science and Technology*, vol. 40, no. 5, pp. 1664–1671, 2006.
- [27] K. C. Lee and B. E. Rittmann, "Effects of pH and precipitation on autohydrogenotrophic denitrification using the hollow-fiber membrane-biofilm reactor," *Water Research*, vol. 37, no. 7, pp. 1551–1556, 2003.

Research Article

Preparation and Characteristics of Polyaluminium Chloride by Utilizing Fluorine-Containing Waste Acidic Mother Liquid from Clay-Brine Synthetic Cryolite Process

Feng-shan Zhou,¹ Bo Hu,^{1,2} Bao-lin Cui,¹ Feng-bao Liu,^{1,3} Fang Liu,¹ Wei-heng Wang,¹ Yang Liu,¹ Rong-rong Lu,¹ Ying-Mo Hu,¹ Yi-he Zhang,¹ and Jin-Guang Wu⁴

¹ School of Materials Science and Technology, China University of Geosciences, Beijing 100083, China

² National Library of China, Beijing 100081, China

³ Tabei Exploratory & Development Department of PetroChina Tarim Oilfield Company, Korla 841000, China

⁴ College of Chemistry and Molecular Engineering, Peking University, Beijing 100871, China

Correspondence should be addressed to Feng-shan Zhou; zhoufs@cugb.edu.cn and Yi-he Zhang; zyh@cugb.edu.cn

Received 28 May 2014; Accepted 29 July 2014; Published 17 August 2014

Academic Editor: Chaomeng Dai

Copyright © 2014 Feng-shan Zhou et al. This is an open access article distributed under the Creative Commons Attribution License, which permits unrestricted use, distribution, and reproduction in any medium, provided the original work is properly cited.

Clay-brine process employing activated clay, NaCl, HCl, and HF as raw materials is the primarily advanced technology to synthesize cryolite in the present industrial grade. However, plenty of byproducts of fluorine-containing waste HCl at the concentration of about 10%~12% could not be utilized comprehensively and are even hazardous to the environment. This work proposed a new two-step technology to prepare inorganic polymer flocculants polyaluminium chloride (PAC) from synthetic cryolite mother liquor. Many specific factors such as the variety of aluminide source, reaction temperature and time, reagent ratio, and manner of alkaline addition were taken into consideration and their influences on the performances of produced PAC were discussed. It was found that synthetic cryolite mother liquor could react with bauxite and calcium aluminate directly to prepare cheap PAC, with plenty amount of water insoluble CaF_2 and CaSiF_6 produced as well. However, once HCl was introduced into synthetic cryolite mother liquor as well as by utilizing bauxite as aluminide source and sodium aluminate as adjusting basicity agent, the resultant PAC would dissolve out higher amount of aluminum while producing little amount of water insoluble materials. The coagulation behavior of the specially produced PAC could even match the industrial grade PAC conforming to national standard.

1. Introduction

1.1. Cryolite and Clay-Brine Synthetic Process. Cryolite, with professional name sodium aluminum fluoride and molecular formula Na_3AlF_6 , is a kind of white and small-geometry crystal whose group can be divided into synthetic cryolite and natural cryolite according to the origin of the material itself. It is well recognized that synthetic cryolite possesses much higher solubility than natural cryolite. The other property parameters of synthetic cryolite are as follows: specific gravity 3, hardness 2~3, melting point 1000°C, and air-slaking after absorption of water. Due to these distinguished properties, cryolite has been applied in diverse fields, among which being utilized as fluxing agent is one of the most common ways. Besides, it is also the significant raw material of aluminium

industry. For example, about 100~120 kg cryolite was reported to be consumed to produce 1 t metal-alumina in the present technology [1]. Thus, it is concluded that the large-scale aluminium industry would never exist in this world without cryolite.

There are various kinds of process routes to fabricate cryolite in industry and the raw materials differ greatly from each other accordingly. Among all the technology routes, the most industrial competitive and representative one is the well-known clay-brine process (CBP) employing activated clay, NaCl, HCl, and HF as raw materials [2]. The famous Dofluoride Chemicals Co. Ltd. located in Jiaozuo of China is the biggest production corporation in the world to produce synthetic cryolite and the process route it adopts is also the CBP as shown in Figure 1.

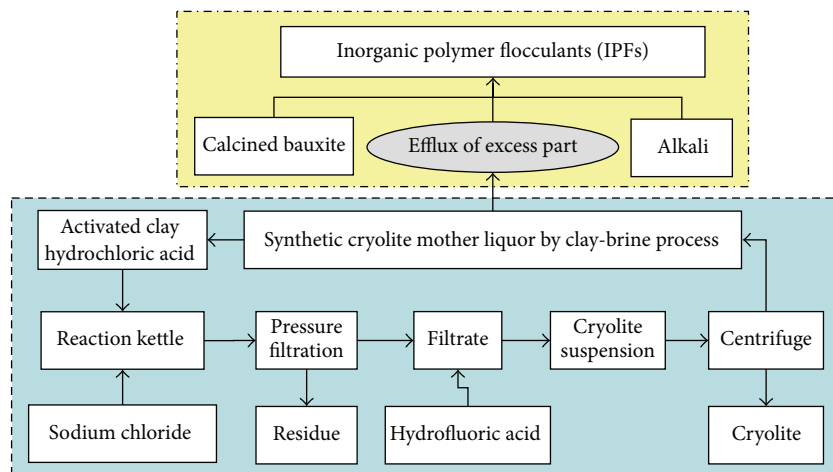
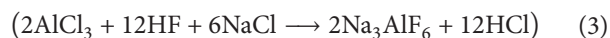
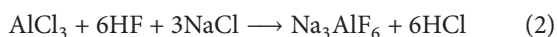


FIGURE 1: Process chart of synthetic cryolite by clay-brine process.

1.2. Features of Cryolite Mother Liquor. Fluorine-containing waste hydrochloric acid from CBP of synthetic cryolite is also commonly known as synthetic cryolite mother liquor (SCML). According to the following CBP reaction principles [2], 6 mol affiliated HCl will be produced to fabricate 1 mol cryolite with AlCl_3 as the aluminide source. The amount would even increase to as high as 12 mol once AlCl_3 is replaced by Al_2O_3 as the aluminide source. Among the total 12 mol HCl, 6 mol HCl would reverse back into the system to leach the clay for cycling utilization. However, the other 6 mol HCl would still remain as residue in the system and need to let out for postprocessing, enhancing the complexity as well as the cost of the process route remarkably. It is estimated that 50 000 m^3/a extra acidic synthetic cryolite mother liquor would be created if Do-fluoride Chemicals Co. fabricates 20 000 t/a synthetic cryolite [3–5]. Consider



Though SCML from CBP of synthetic cryolite possesses complicated composition as shown in Table 1, F^- , Cl^- , H^+ , and Na^+ are four main kinds of ions in it. Meanwhile, the total acidity ranges from 110 g/L to 140 g/L (or 3~4 mol/L) (or 10.4%~13.8%) and the weight percentage of NaCl is no more than 40 g/L. This is because the clay utilized in acid leaching is always made from the low grade calcined bauxite with $w(\text{Al}_2\text{O}_3) \geq 25\%$ and $w(\text{Fe}_2\text{O}_3) \geq 2.0\%$.

According to the standard of public water established by the American Environmental Protection Administration (EPA), drinking water with 0.4~0.6 mg/L F^- will do benefit to human health. However, the situation is not that optimistic when drinking water with F^- concentration higher than 1.0 mg/L for a long time which may even cause serious diseases such as dental and bone fluorosis [4]. In addition, both the difficult controlling of technology and the expensive cost of waste outlet during the treatment process of SCML as acidic waste make corporations suffer from tremendous

TABLE 1: Chemical composition of synthetic cryolite mother liquor (SCML).

Anionic ion	Concentration (g/L)	Cationic ion	Concentration (g/L)
F^-	18.10000	Na^+	24.28000
Cl^-	139.71000	K^+	0.28402
CO_3^{2-}	20.00000	Ca^{2+}	0.07636
SO_4^{2-}	0.75030	Mg^{2+}	0.09012
SiO_3^{2-} (SiO_2)	0.01120	Fe^{3+}	3.08000
		Al^{3+}	0.00000

environmental protection pressure [5]. And the enterprise has a great amount of waste acid liquid containing F^- , which is badly in need of finding an environmental economy processing method. Meanwhile, it is difficult to polymerize in the preparation of PAC because of the common ion effect of F^- . We need to search for a new preparation method in this paper. Thus, this work optimized the process route using SCML to produce inorganic polymer flocculants (IPFs) polyaluminium chloride (PAC). Moreover, the reason for the generation of highly water insoluble materials was well explained via exploration of the XRD phase of products from the reactions. Besides, the well cost performance product PAC was obtained and the optimized route had also been applied in industry.

2. Materials and Experimental Methods

2.1. Materials and Instruments. Sodium aluminate, HCl, HAc, NaAc, $\text{Zn}(\text{Ac})_2$, $\text{NH}_3 \cdot \text{H}_2\text{O}$, KF, and EDTA were used for chemical purity. Other purchased industrial grade raw materials included technical hydrochloric acid diluted to 18 wt%; bauxite (Al_2O_3 30 wt%); calcined bauxite (Al_2O_3 40 wt%); calcium aluminate powder (Al_2O_3 53 wt%, CaO 28 wt%); polyaluminium chloride (PAC, Al_2O_3 29 wt%). SCML was the byproduct acid from Do-fluoride Chemicals Co. and the composition was described in Table 1.

pH values were determined by pH500 meter, CLEAN, USA; SGZ-2 turbidimeter was employed to measure turbidity by Shanghai Yuefeng Instruments & Meters Co., Ltd; COD_{Cr} (potassium dichromate as oxidant) was measured by 5B-6 COD reactor, Lian-Hua Tech. Co., China.

2.2. Experimental Methods and Details

2.2.1. Preparation of PAC from Synthetic Cryolite Mother Liquor. Certain amount of synthetic cryolite mother liquor was added into a three-neck flask with a condenser firstly. After the temperature of the flask was heated to 70°C in oil bath, certain amount of bauxite was added into the system step by step. The reaction should continue for 1 h after the temperature increases to 100°C. Then alkaline polymerization adjusting agent (APA, calcium aluminate powder, or sodium aluminate powder) was added into the above reaction system gradually to adjust pH value. The addition speed of APA depended on pH value of the system: when pH value was lower than 2.7, the speed can be fast, but when it was over 2.7, the speed should be slow until it increased to 3.5~3.8 further. At this point, APA should not be added into the system any more. After all these operations, the reaction is kept for another 1.5 h at 100°C. Then the reaction should be suspended immediately via halting both the vigorous stirring and oil bath heating followed by coagulating the system for 12 h using the residual heat of oil bath. Liquid PAC was obtained after the filtering of the upper clear liquid of the already stewed reaction suspension. And solid PAC was finally obtained after the initial liquid PAC was dried at 105°C.

2.2.2. Basicity of the Produced PAC. OH⁻ is the basic component influencing the morphology of polyaluminium chloride [6–9] whose index in PAC is measured by basicity (B). According to GB 15892-2003 (water treatment chemical-polyaluminium chloride) [10], basicity can be measured. The mol percentage of OH and Al in PAC is defined as basicity and this parameter can reflect the degree of polymerization of PAC to some extent, which affects the coagulation performances of PAC. Basicity can be calculated according to the following during the fabrication process of PAC:

$$\text{Basicity} = \frac{(\text{OH})}{(\text{Al})} \times 100\%. \quad (4)$$

2.2.3. Coagulation Performance of the Produced PAC. Coagulation tests were performed by using simulated diatomite water and real oily wastewater samples. All coagulation tests were conducted in 100 mL beakers using a magnetic stirring apparatus. 100 mL of the test water was placed in a beaker and stirred rapidly at 200 rpm for 2 min after adding the coagulant at room temperature, followed by slow stirring at 40 rpm for 2 min and sedimentation for 10 min. Then a supernatant sample was taken at 1.0 cm below the surface of the test water for turbidity and COD_{Cr} measurement.

2.2.4. Characterization of the Produced PAC. The produced PAC solution was dehydrated at 105°C and made powder

sample for structure analysis. X-ray diffraction (XRD) was measured for the determination of crystalline phases in solid coagulants using D/max-rA X-ray diffractometer with Cu K radiation in the 2θ range of 3° to 80° at a scan rate of 8°/min. The solid produced PAC was analyzed by FT-IR with the Perkin Elmer spectrum 100 FT-IR spectrophotometer and potassium bromide pellet method. The spectra were scanned in the range of 4000 to 500 cm⁻¹.

3. Results and Discussion

3.1. Synthesis Optimization. The pH value of the leaching reaction system was the most critical technological parameter during the fabrication process of PAC [11–13]. Due to the amphoteric compound property of aluminum, the state of aluminum salt solution showed certain transformation law along with pH value alteration. When the pH value of the leaching agent was less than 4, aluminum mostly existed as hydrated ions. These hydrated ions would get hydrolysed as pH value increased, and the mononuclear or monohydroxy compounds would first generate, and then the new produced compounds evolve into three-nuclear or multi-hydroxy compounds along with further increase of pH value. In this compound, bridging effect took place between ions and hydroxyl, creating multiple nuclear hydroxyl complexes known as inorganic polymer. The specific states of aluminum salt solution along with pH value alteration were as follows [13–15]:

$$\begin{aligned} \text{pH} < 4, & [\text{Al}(\text{H}_2\text{O})_n]^{3+}, n = 6\sim 10; \\ 4 < \text{pH} < 6, & [\text{Al}_6(\text{OH})_{15}]^{3+}, [\text{Al}_7(\text{OH})_{17}]^{4+}, \\ & [\text{Al}_8(\text{OH})_{20}]^{4+}, [\text{Al}_{13}(\text{OH})_{34}]^{5+}; \\ 6 < \text{pH} < 8, & [\text{Al}(\text{OH})_3]; \\ \text{pH} > 8, & [\text{Al}(\text{OH})_4]^{-}, [\text{Al}_8(\text{OH})_{26}]^{2-}. \end{aligned}$$

The chemical equations to prepare PAC were indicated as follows:



According to the above reaction principles, the influencing factors such as the kind and amount of APA, amount of water insoluble material, and leaching aluminum as well as the degree of polymerization (or basicity) were deeply discussed in this work and results were described in Table 2 from which two laws were concluded.

- (1) Once synthetic cryolite mother liquor was the only taken acid leaching agent, the leaching efficiency of aluminum was not that high. Nevertheless, it could be enhanced apparently when appropriate HCl was added into synthetic cryolite mother liquor.
- (2) When calcium aluminate was used as APA, Ca²⁺ would react with F⁻ and SiO₃²⁻ in synthetic cryolite mother liquor and high amount of water insoluble material was thus produced. However, if calcium aluminate was replaced by sodium aluminate as APA, the

TABLE 2: Optimization experiment to prepare PAC by SCML leaching bauxite.

Sample	Acid	Alkali	Al ₂ O ₃ (%)	Basicity (%)	Insoluble solid in water (%)
A	SCML	Calcium aluminate	28.7	87	11.2
B	SCML + HCl	Calcium aluminate	29.1	79	5.8
C	SCML + HCl	Sodium aluminate	30.2	66	1.5

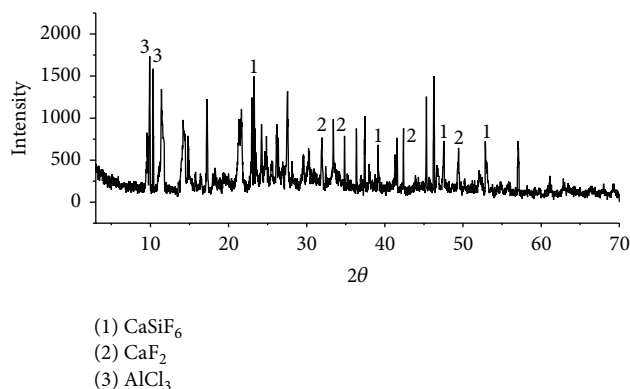


FIGURE 2: XRD spectra of PAC (Sample B) generated from polymerization induced by calcium aluminate as pH adjusting agent.

amount of water insoluble material would decrease significantly.

Based on the above experimental results, the reaction condition was optimized as follows: 200 mL mixed acid was obtained first by blending 150 mL synthetic cryolite mother liquor (containing HCl 12%) with 50 mL industrial 31% concentrated HCl. 80 g bauxite was then added into the mix and the reaction was kept for 1~2 h at 80~100°C. The polymerization was completed when 23 g sodium aluminate was added into the system to adjust pH value followed by coagulation for 12 h under vigorous stirring. PAC with industrial quality standard could be obtained after the stewing and filtering of the reaction agent.

3.2. Structure of the Produced PAC. The final product following the optimized preparative conditions was analyzed with XRD and FT-IR to obtain detailed structural information.

XRD spectra of PAC (Sample B) generated from polymerization induced by calcium aluminate as pH adjusting agent were showed in Figure 2. It was indicated that there appeared characteristic absorption bands assigned to water insoluble CaF₂ and CaSiF₆ besides the absorption band of AlCl₃. This might be because HF in synthetic cryolite mother liquor dissolved SiO₂ in calcium aluminate into SiO₃²⁻ and both SiO₃²⁻ and F⁻ encountered Ca²⁺ leached from calcium aluminate to form water insoluble CaF₂ and CaSiF₆.

However, in the XRD spectra of PAC (Sample C) generated from polymerization induced by sodium aluminate as pH adjusting agent (Figure 3), it was not difficult to find that there existed characteristic absorption bands of Fe except for the absorption band of AlCl₃. This might be because HF

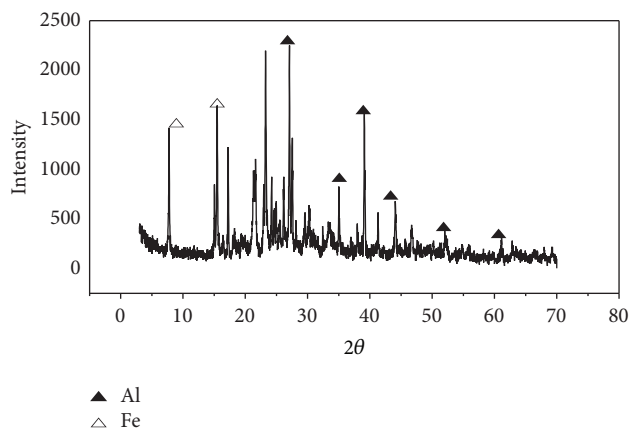


FIGURE 3: XRD spectra of PAC (Sample C) generated from polymerization induced by sodium aluminate as pH adjusting agent.

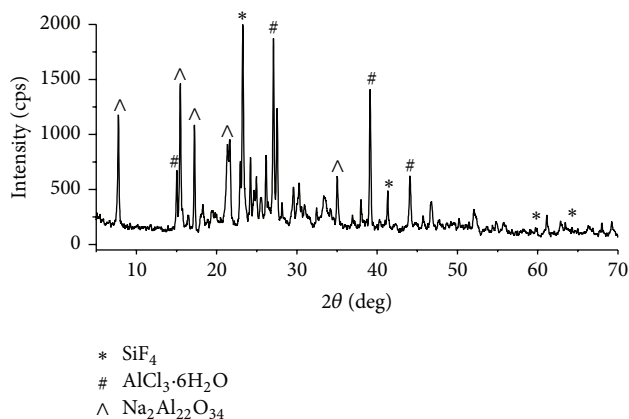


FIGURE 4: XRD spectra of crystal leached from bauxite via SCML and HCl mixed acid.

and HCl in synthetic cryolite mother liquor dissolved Fe in bauxite into Fe²⁺ and Fe³⁺, with Fe(OH)₃ further produced.

In order to confirm that Fe in bauxite can be abundantly dissolved out in acid leaching process, SCML and HCl mixed acid was proposed to leach bauxite. XRD results of the crystal obtained from the dried leaching solution indicated that the main components of this crystal contained SiF₄, AlCl₃·6H₂O, and Na₂Al₂O₃₄ (Figure 4). Thus, it was clear that PAC prepared from SCML was rather different from industrial grade PAC. Instead, it was made up of multiple crystal phases and components and AlCl₃, FeCl₃, SiF₄, and H₂SiO₃ were especially typical. The plural gel formed by the polymerization of these components might show synergism effect on the coagulation characteristic of PAC [16–20].

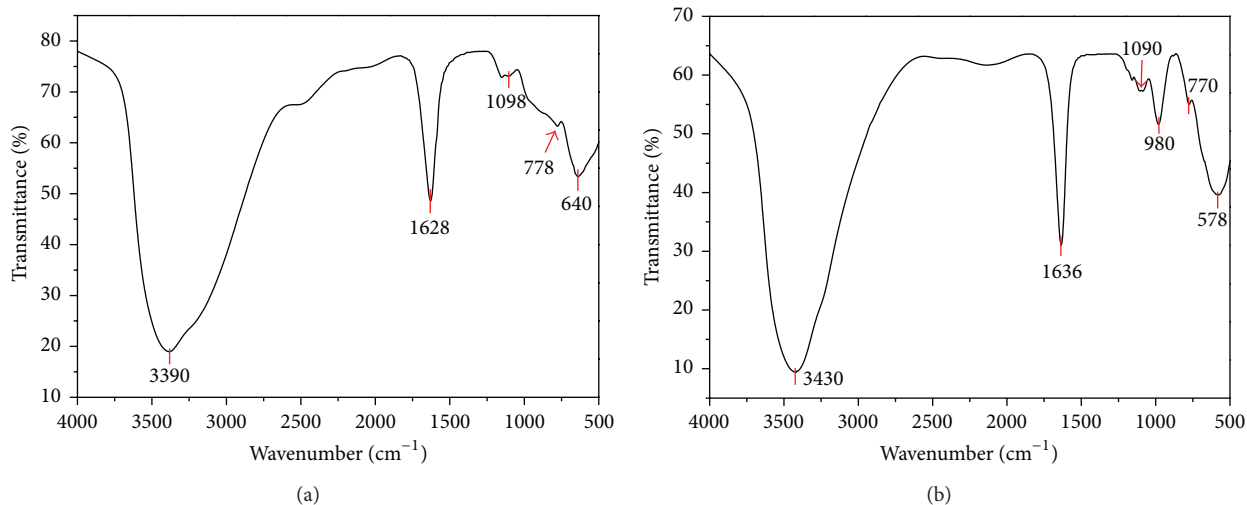


FIGURE 5: FT-IR spectra for (a) the produced PAC by SCML and (b) industrial grade PAC.

It was well recognized in collochemistry that the positive discharged $\text{Fe}(\text{OH})_3$ colloidal particles with small amount in system could create bridged bonds among negative colloidal particles just like coagulating agent, thus getting precipitated via mutual absorption. On this occasion, $\text{Fe}(\text{OH})_3$ functioned as coagulant aid [18, 19].

The existence of small amount of silica sol (also ludox) not only could promote the coagulating process of water as well as improving the structure of precipitation particles, but also could increase their weight, accelerating the formation and precipitation of precipitation particles. Therefore, silica sol could also function as coagulant aid. Unlike the large amount of positive charge of Al_{13} as key component of flocculation agent of PAC, the surface of silica gel particles was filled with negative charge instead. Thus, these two kinds of particles with totally opposite charge would allure each other to get absorbed. Meanwhile, silica gel could also absorb other scattered colloidal particles with positive charge, strengthening the coagulating effect accordingly [15, 17, 21, 22].

From the above discussion, it was found that the produced PAC by SCML (PAC-SCML) was rather different from common industrial grade PAC (PAC-IG). Except for the relative strong coagulating character, it was a kind of composite flocculant containing certain amount of Fe and Si, which could be treated as the compound of PAC, polyaluminum ferric chloride (PAFC), and polysilicate (PSi) [18–20, 23]. Besides, FT-IR spectra of this special PAC showed much difference from that of common PAC as indicated in Figure 5.

The possible chemical bonds in PAC-SCML (Sample C) were investigated by the FT-IR spectra and were compared with PAC-IG (Figure 5). The two samples showed similar FT-IR spectra. Both spectra exhibited a broad absorption peak in the range of $3200\text{--}3650\text{ cm}^{-1}$ (3390 cm^{-1} for PAC-SCML and 3430 cm^{-1} for PAC-IG), which could be assigned to the stretching vibrations of $-\text{OH}$ groups. The peaks in the range of $1600\text{--}1700\text{ cm}^{-1}$ (1628 cm^{-1} for PAC-SCML and 1636 cm^{-1} for PAC-IG) were attributed to the bending vibrations of water

absorbed, polymerized, and crystallized in the coagulant. The PAC-IG was not a pure substance, which also contains some iron ions. The peak at 1098 cm^{-1} for PAC-SCML and the peak at 1090 cm^{-1} for PAC-IG were attributed to the asymmetric stretching vibration of $\text{Fe}-\text{OH}-\text{Fe}$ or $\text{Al}-\text{OH}-\text{Al}$; furthermore, there were two peaks at 778 cm^{-1} and 640 cm^{-1} for PAC-SCML and two peaks at 770 cm^{-1} and 578 cm^{-1} for PAC-IG, which were attributed to bending vibrations of $\text{Fe}-\text{OH}$ and $\text{Al}-\text{OH}$, respectively [24–28].

3.3. Coagulation Characteristics. Coagulation tests were performed by using simulated diatomite water and real oily wastewater samples. The turbidity of the simulated diatomite water samples was 1480 NTU, 720 NTU, and 80 NTU. The COD_{Cr} of the oily wastewater samples obtained from Liaohe Petroleum Exploration Bureau of China was 534 mg/L and its turbidity was 124 NTU.

As indicated in the flocculation results in Table 3, the coagulation effect of PAC-IG was much better than that of PAC-SCML for simulated diatomite water with low turbidity. However, the coagulation effect of PAC-SCML had distinguished advantages over that of PAC-IG for simulated diatomite water with high turbidity, which might originate from the formation of PAFC and PSi with strengthening coagulation effect in acid leaching process. Moreover, the small amount of water insoluble CaF_2 and CaSiF_6 in PAC-SCML could also benefit the coagulating reaction for high turbidity water.

The COD_{Cr} removal of PAC-SCML and PAC-IG both achieved the minimum at 60 mg/L dosage while PAC-SCML was relatively superior to PAC-IG for oily sewage from Liaohe Oilfield, and the same law was presented for turbidity removal.

The results suggested that despite the small difference in alumina content between PAC-SCML and PAC-IG, PAC-SCML was superior to PAC-IG in both the comprehensive coagulating character and manufacturing cost due to the certain amount of Fe and Si in PAC-SCML.

TABLE 3: Coagulation behavior contrast of the produced PAC by SCML versus industrial grade PAC.

Performances	Simulated diatomite water added 30 mg/L flocculant			Oily wastewater added 60 mg/L flocculant	
	Residual turbidity (NTU)			Residual COD _{Cr} (mg/L)	Residual turbidity (NTU)
Samples	1480 Initial	720 Initial	80 Initial	534 Initial	124 Initial
A	261	—	—	358	42
B	279	—	—	355	38
C	25	24	15	245	6
PAC-IG	34	20	10	330	18

4. Conclusions

The preparation of PAC coagulant from synthetic cryolite mother liquor from clay-brine process (PAC-SCML) with advanced performances compared with conventional industrial grade PAC (PAC-IG) coagulant was achieved. Reaction conditions including the choice of leaching acid and alkaline polymerization adjusting agent, the pH value, and the reaction temperature and reaction time were thoroughly studied to optimize the coagulation performances and minimize the insoluble solid in water of the prepared coagulant. The optimized technique to prepare PAC-SCML was that adjusting the concentration of HCl in synthetic cryolite mother liquor to 18% with the industrial grade HCl (the concentration about 32% to 36% in general) firstly, and then adding the needed bauxite. Then the acid leaching reaction was kept for 1~2 h at 80~100°C and sodium aluminate was consequently added to adjust pH value to 3.5~3.8. The whole technology would be completed after a 24 h coagulation process. The coagulation performances tested showed that PAC-SCML is better than PAC-IG in turbidity removal at high turbidity simulated diatomite water and in COD_{Cr} removal at real oily wastewater. Both XRD and FT-IR results confirmed that there existed certain amount of Fe and Si in PAC-SCML, which could combine Al to form multiple nuclear inorganic polymer and make the resultant PAC-SCML possess advanced coagulating performances. This technology will become an effective way to treat the large amount of waste acid solution in cryolite fabrication process.

Conflict of Interests

The authors declare that there is no conflict of interests regarding the publication of this paper.

Acknowledgment

This research was supported by the National High Technology Research and Development Program (863 Program 2012AA06A109) of China.

References

- [1] H. P. Ding, "Production technology and market situation of cryolite products," *Yunnan Metallurgy*, vol. 33, no. 3, pp. 64–69, 2004.
- [2] Z. Y. Tang, "Producing sand like synthetic cryolite by clay bittern method," Patent CN 1056091 A, 1991.
- [3] H. H. Yu, H. Wang, S. Y. Yang et al., "The comprehensive utilization of aluminium fluoride mother liquor," *Inorganic Chemicals Industry*, vol. 37, no. 4, pp. 34–35, 2005.
- [4] T. Dong, J. M. Liu, Z. X. Li et al., "High concentration fluoride wastewater treatment," *Tianjin Chemical Industry*, vol. 18, no. 5, pp. 58–60, 2004.
- [5] M. Zhang, H. N. Yang, X. X. Zhang et al., "Preparation of polyaluminium ferrous chloride by using cryolite mother liquor," *Inorganic Chemicals Industry*, vol. 42, no. 3, pp. 43–44, 2010.
- [6] L. Allouche and F. Taulelle, "Conversion of Al₁₃ Keggin ϵ into Al₃₀: a reaction controlled by aluminum monomers," *Inorganic Chemistry Communications*, vol. 6, no. 9, pp. 1167–1170, 2003.
- [7] W. Seichter, H. J. Mogel, P. Brand, and D. Salah, "Crystal structure and formation of the aluminium hydroxide chloride Al-13(OH)(24)(H₂O)(24) Cl-15 center dot 13H(2)O," *European Journal of Inorganic Chemistry*, no. 6, pp. 795–797, 1998.
- [8] W. Z. Wang and P. H. Hsu, "The nature of polynuclear OH-Al complexes in laboratory-hydrolyzed and commercial hydroxylaluminum solutions," *Clays & Clay Minerals*, vol. 42, no. 3, pp. 356–368, 1994.
- [9] J. E. van Benschoten and J. K. Edzwald, "Chemical aspects of coagulation using aluminum salts—I. Hydrolytic reactions of alum and polyaluminum chloride," *Water Research*, vol. 24, no. 12, pp. 1519–1526, 1990.
- [10] GB15892-2003, "Water treatment chemical-Poly aluminium chlorid. Chinese administration of quality supervision, inspection and quarantine".
- [11] R. R. Lu, Y. H. Zhang, F. S. Zhou, X. Wang, Q. An, and Z. Meng, "Novel polyaluminum ferric chloride composite coagulant from Bayer red mud for wastewater treatment," *Desalination and Water Treatment*, vol. 295, pp. 1–9, 2013.
- [12] W. Li, T. Hua, and Q. X. Zhou, "Preparation, morphology and coagulation characteristics of a new polyferric chloride coagulant prepared using pyrite cinders," *Environmental Technology*, vol. 32, no. 8, pp. 911–920, 2011.
- [13] Z. L. Huang, Y. H. Hu, and Z. F. Jiang, "Preparation of polyaluminum chloride from waste chlorhydric acid and poor quality Kaolin," *Environmental Protection of Chemical Industry*, vol. 22, no. 5, pp. 284–286, 2002.
- [14] W. Lan, H. Qiu, J. Zhang et al., "Characteristic of a novel composite inorganic polymer coagulant-PFAC prepared by hydrochloric pickle liquor," *Journal of Hazardous Materials*, vol. 162, no. 1, pp. 174–179, 2009.
- [15] T. Sun, C. Sun, G. Zhu et al., "Preparation and coagulation performance of poly-ferric-aluminum-silicate-sulfate from fly ash," *Desalination*, vol. 268, no. 1–3, pp. 270–275, 2011.

- [16] G. Zhu, H. Zheng, W. Chen, W. Fan, P. Zhang, and T. Tshukudu, "Preparation of a composite coagulant: polymeric aluminum ferric sulfate (PAFS) for wastewater treatment," *Desalination*, vol. 285, no. 31, pp. 315–323, 2012.
- [17] B. Y. Gao, Z. S. Wang, and H. X. Tang, "Study on the hydrolysis-polymerization process of aluminum and the interaction between hydrolyzed aluminum species and polysilicic acid in flocculant polyaluminum silicate chloride (PASC)," *ACTA Scientiae Circumstantiae*, vol. 20, no. 2, pp. 151–153, 2000.
- [18] F. S. Zhou, L. Ma, J. G. Wu et al., "Complexing agent, preparing method and use thereof," CN1552629, 2004.
- [19] F. S. Zhou, L. Ma, J. G. Wu et al., "Complexometric synergist, preparing method and use thereof," CN1552636, 2004.
- [20] F. S. Zhou, L. Ma, J. G. Wu et al., Flocculent, preparing method and use thereof. CN1552637, 2004.
- [21] D. S. Wang and H. X. Tang, "Poly ferric silicon type compound inorganic high molecular flocculant and its preparing method," CN1210818, 1999.
- [22] Z. P. Ai, B. Y. Gao, and S. R. Wang, "Electron microscopic observation on sol and gel of polysilicic acid," *Environmental Chemistry*, vol. 13, no. 2, pp. 119–122, 1994.
- [23] Y. M. Fang, X. D. Zhao, and X. L. Zhang, "Study on the image, structure and coagulation behavior of polysilicate-aluminum ferric," *Industrial Safety and Environmental Protection*, vol. 33, no. 10, pp. 22–24, 2007.
- [24] F. Zhou, S. Wang, J. Su et al., "Structural characteristics of infrared spectra for polyaluminum chloride in enhanced reactions of modification," *Spectroscopy and Spectral Analysis*, vol. 24, no. 5, pp. 532–535, 2004.
- [25] H. Yu, B. Y. Gao, Q. Y. Yue et al., "Study on the structural characteristics of polyaluminum silicate chloride by infrared spectrum method," *Journal of Shandong University (Natural Science Edition)*, vol. 34, no. 2, pp. 198–201, 1999.
- [26] W. N. Chen, H. P. Zhong, J. Yang et al., "Analysis of IR spectrum and crystal morphology of polyaluminum-silica chloride (PASC) prepared by various methods," *Chemical Research and Application*, vol. 14, no. 1, pp. 73–75, 2002.
- [27] F. S. Zhou, S. H. Wang, J. Z. Su et al., "Infrared spectra and characteristics of PMC—a multicore inorganic polymer flocculant," *Fine Chemicals*, vol. 20, no. 10, pp. 615–618, 2003.
- [28] X. Zhang, L. Zhou, and M. Tang, "Study of infrared spectra of polyaluminum ferric chloride," *Spectroscopy and Spectral Analysis*, vol. 22, no. 1, pp. 39–42, 2002.

Research Article

The Effect of Salinity on Membrane Fouling Characteristics in an Intermittently Aerated Membrane Bioreactor

Kang Xie,¹ Siqing Xia,² Jing Song,³ Jixiang Li,⁴ Liping Qiu,¹
Jiabin Wang,¹ and Shoubin Zhang¹

¹ School of Civil Engineering and Architecture, University of Jinan, Jinan, Shandong 250022, China

² State Key Laboratory of Pollution Control and Resource Reuse, College of Environmental Science and Engineering, Tongji University, Shanghai 200092, China

³ Shandong Province Environmental Protection Technology Service Center, Jinan, Shandong 250102, China

⁴ Shanghai Advanced Research Institute, Chinese Academy of Sciences, Shanghai 201203, China

Correspondence should be addressed to Kang Xie; sdxxkang@gmail.com and Siqing Xia; otw1208@gmail.com

Received 24 April 2014; Revised 13 July 2014; Accepted 16 July 2014; Published 5 August 2014

Academic Editor: Chaomeng Dai

Copyright © 2014 Kang Xie et al. This is an open access article distributed under the Creative Commons Attribution License, which permits unrestricted use, distribution, and reproduction in any medium, provided the original work is properly cited.

The effect of salinity on the membrane fouling characteristics was investigated in the intermittently aerated membrane bioreactor (IAMBR). Five different salinity loadings were set from 0 to 35 g·L⁻¹ (referring to NaCl), respectively. The removal of total organic carbon (TOC) and ammonia-nitrogen (NH₄⁺-N) was gradually decreased with increasing salinity. The variation of membrane filtration resistance, particle size distribution (PSD), extracellular polymeric substances (EPS), soluble microbial products (SMP), and relative hydrophobicity (RH) analysis revealed that salinity has a significant effect on sludge characteristics in IAMBR. The results also indicated that the membrane fouling is often caused by the integration of sludge characteristics in saline wastewater.

1. Introduction

Recent years, with the rapid development of economy, pollutions of water environment, and shortages of water resource are becoming the most important problems for public health [1]. In addition, the increasing environmental protection requirements need new technologies to make a better effluent quality. Membrane bioreactor (MBR) where activated sludge process is combined with membrane filtration has been widely used for wastewater treatment and reuse. MBR is able to provide small footprint, perfect effluent, higher biodegradation efficiency, and less excess sludge, regarding as an innovative and promising technology [2]. However, membrane fouling, which reduces membrane permeability and increases operational cost, is still the major obstacles for the wider application of MBR in biological wastewater treatment. It is extensively studied by focusing on fouling factors, such as sludge characteristics, operational conditions, feedwater characteristics, aeration, hydraulic conditions, and membrane materials [3]. In general, complex membrane

foulants and sludge characteristics are assumed to be the main cause of membrane fouling. Sludge characteristics are direct affected by operating parameters, dissolved oxygen, organic loading, salinity, and so on. The understanding of inorganic fouling in saline wastewater is still not clear. Once the inorganic scaling forms on the membrane surface, it is difficult to be eliminated using chemical cleaning [4]. Therefore, more attention should be paid to membrane fouling in saline wastewater.

Industrial wastewater, wastewater recycling, and seawater utilization often lead to high salinity in discharged wastewater. In general, effluent of many industries such as food processing, leather, petroleum, dairy, and fish processing often causes saline wastewater, which increased rapidly over the last decades [5–7]. Furthermore, in areas lacking fresh water, such as Hong Kong, seawater can be used for toilet flushing in order to save freshwater, resulting in higher salinity in wastewater treatment plant (WWTP) [8]. These high salinity wastewaters often contain large amounts of soluble inorganic salts combined with organic compounds.

For conventional activated sludge system, high salinity has been shown to cause plasmolysis and loss of activity of cells because of the unbalance of osmotic stress [9].

However, the MBR is considered as a promising technology to treat salinity wastewater, owing to higher biomass concentration retained by membrane filtration and longer sludge retention time. Several studies have recently reviewed saline wastewater treatment using MBR. Jang et al. [10] investigated the effect of salinity on the performance and membrane fouling in MBR. The results showed a decreasing of ammonia removal and significant changes of microbial community composition. And then, the membrane fouling increased with elevated salinity. Johir et al. [11] also showed a poor performance at higher salinity ($35 \text{ g}\cdot\text{L}^{-1}$).

It is known that a modification in biomass kinetics as well as in sludge characteristics would be attained in MBR treating saline wastewater, which can significantly influence the development of membrane fouling. The SMP, EPS, PSD, and so on were investigated by previous studies [12, 13] trying to examine the relation between sludge characteristics and membrane fouling in saline wastewater. Nevertheless, it has not completely elucidated the variation of sludge characteristics and membrane fouling at different salinities.

Therefore, an IAMBR was used to treat salinity wastewater in this study, and the main aim of this study was to investigate the system performance and variation of sludge characteristics such as PSD, EPS, SMP, and RH at different salinity.

2. Materials and Methods

2.1. IAMBR Setup and the Operation. As shown in Figure 1, an intermittently aerated membrane bioreactor (IAMBR) was operated to treat salinity contained municipal wastewater in this study. The effective volume of the bioreactor was 8 L. The IAMBR was equipped with two hollow fiber polyvinylidene fluoride (PVDF) ultrafiltration (UF) membrane modules (Litree Company, Suzhou, China) with a total surface area of 0.12 m^2 and nominal pore size of $0.02 \mu\text{m}$. The outer and inner diameters of the fibers were 1.45 mm and 0.85 mm, respectively. Permeate was extracted by a peristaltic pump at a permeate flux of $5 \text{ L}\cdot\text{m}^{-2}\cdot\text{h}^{-1}$ with mode of 10 min filtration and 2 min rest. The transmembrane pressure (TMP) was monitored by a vacuum meter (Weiken YN-60, Shanghai). Intermittent aeration was supplied by air diffuser at the bottom of the membrane module with the air blower switch on/off. The air flow rate was $0.6 \text{ m}^3\cdot\text{h}^{-1}$ in order to provide oxygen for biological treatment and to alleviate membrane fouling and cake formation. The IAMBR was operated in cycles of 3 hours: 1 hour anoxic reaction without aeration and filtration (anoxic phase) and 2 hours aerobic reaction membrane filtration (aerobic phase). At the beginning of the anoxic phase, the synthetic wastewater was fed to the reactor for about 10 minutes until water level reaching 8 L. The water level was dropped until 6 L at the end of each cycle during the filtration period. Therefore, the hydraulic retention time (HRT) was 12 hours in the IAMBR.

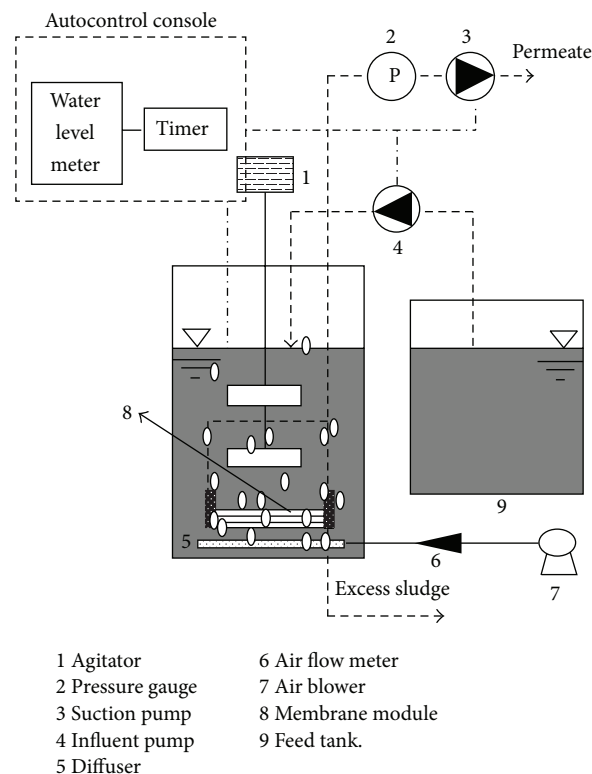


FIGURE 1: Schematic diagram of the bench-scale IAMBR.

During the acclimation period, five parallel IAMBRs (acclimated reactors) were inoculated with activated sludge obtained from QuYang municipal wastewater treatment plant (Shanghai, China). The IAMBRs fed with synthetic wastewater comparable to domestic wastewater adding salinity according to Xie et al. [14]. The main constituent of the synthetic wastewater was shown in Table 1. The salinity levels were expressed as the concentration of sodium chloride (NaCl). The NaCl concentrations of five IAMBRs were 0, 5, 10, 15, 20, and $35 \text{ g}\cdot\text{L}^{-1}$, respectively. The salinity level in each reactor gradually increased from 0 to $35 \text{ g}\cdot\text{L}^{-1}$ with every $5 \text{ g}\cdot\text{L}^{-1}$. After the sludge was matured, it was taken to other five small reactors (operated reactors), respectively. The concentration of mixed liquor suspended solids (MLSS) in each operated reactor was maintained at $5000 \pm 210 \text{ mg/L}$. The HRT, SRT, aeration intensity, and so on were controlled at the same operating mode. The temperature was maintained at $25 \pm 2^\circ\text{C}$.

2.2. Analytical Methods. The influent and effluent were collected daily from the five reactors. The total organic carbon (TOC) was measured instead of chemical oxygen demand (COD), because of the limitations of COD when measuring the organic matter in wastewater samples with chlorides higher than $2000 \text{ mg}\cdot\text{L}^{-1}$. TOC was determined by a TOC analyzer with autosampler (TOC V-CPN, Shimadzu, Japan). The $\text{NH}_4^+\text{-N}$, MLVSS (mixed liquor volatile suspended solid), and MLSS were measured according to Chinese NEPA standard methods [15]. The transmembrane pressure (TMP)

TABLE 1: The main constituent of the synthetic wastewater.

Main composition	Glucose	Corn starch	Peptone	NH ₄ Cl	KH ₂ PO ₄
Concentration (mg·L ⁻¹)	250	250	28	133.75	30.8
Main composition	MgSO ₄ ·7H ₂ O	MnSO ₄ ·7H ₂ O	FeSO ₄	CaCl ₂	NaHCO ₃
Concentration (mg·L ⁻¹)	9	6	0.3	8	120

TABLE 2: Variations and removal efficiencies of TOC in five IAMBRs of different salinity during steady operations.

Salinity (g·L ⁻¹)	Influent (mg·L ⁻¹)	Effluent (mg·L ⁻¹)	Removal efficiency (100%)
0	106.6 ± 40.3	4.9 ± 1.9	95.3 ± 4.7
5	115.7 ± 16.9	4.8 ± 2.1	95.8 ± 1.6
10	110.9 ± 14.1	4.7 ± 1.3	95.7 ± 1.3
15	111.7 ± 20.9	9.4 ± 3.0	91.6 ± 1.6
20	112.8 ± 22.0	10.3 ± 3.6	90.9 ± 2.0
35	110.5 ± 19.4	18.3 ± 7.1	83.4 ± 3.6

was recorded with using a vacuum meter (YN-60, Shanghai Weiken). Dehydrogenase activity (DHA) was estimated using redox sensitive 2,3,5-triphenyltetrazolium chloride (TTC) followed Reddy's description [16]. The DHA was estimated by mg TF per g MLSS and per hour.

2.3. Evaluation of Filtration Resistance. Membrane resistance was characterized by the resistance-in-series model according to Meng et al. [17] as follows:

$$R_t = R_m + R_p + R_c = \frac{\Delta\text{TMP}}{\mu J}, \quad (1)$$

where R_t is the total membrane resistance (m⁻¹), R_m is the intrinsic resistance of the new membrane (m⁻¹), R_p is the pore blocking resistance (m⁻¹), R_c is the cake resistance (m⁻¹), ΔTMP is the transmembrane pressure difference (Pa), μ is permeate viscosity (Pa·s), and J is permeate flux (m³·m⁻²·s⁻¹). Total resistances were calculated from the flux, the transmembrane pressure difference, and the viscosity.

2.4. PSD Analysis. The mixed liquor samples were collected from the 5 different salinity operated reactors. The PSD was analyzed using a laser granularity distribution analyzer (Eye Tech Particle Size and Shape Analyzer, USA) with a detection range of 0.1–3600 μm.

2.5. EPS and SMP Analyses. EPS and SMP were extracted from the mixed liquors in each operated reactor according to the previous study [2]. Both the EPS and SMP concentrations were expressed by the carbohydrates and proteins. The carbohydrates concentrations were determined by the anthrone method with glucose as a standard, and the proteins concentrations were measured using the bicinchoninic acid assay (BCA) with bovine serum albumin as a standard. Both the EPS and SMP analyses were performed in triplicate, and the average value was calculated.

2.6. RH. The RH was measured as described previously [18]. The mixed liquor samples from 5 operated reactors

were homogenized by sonication and then were separated by hexadecane. The RH was quantified as the ratio of MLSS concentration in the aqueous phase after emulsification (MLSS_e) to the concentration of MLSS in the aqueous phase before emulsification (MLSS_i):

$$\text{RH} = \left[1 - \left(\frac{\text{MLSS}_e}{\text{MLSS}_i} \right) \right]. \quad (2)$$

Each sample was analyzed at least three times, and the average value was calculated. The sludge samples were washed with distilled water in order to avoid the salt interference.

3. Results and Discussion

3.1. The Performance of IAMBR at Different Salinity. After the activated sludge of 5 acclimated reactors was matured, the steady stage was reached. The influent and effluent were collected daily from each acclimated reactor for a long time under the steady stage, and the TOC and NH₄⁺-N were measured (Tables 2 and 3). As is shown in Tables 2 and 3, the TOC removal showed a similar tendency as that of NH₄⁺-N at different salinity of acclimated reactors. In view of the effluent quality, removal of TOC and NH₄⁺-N performed stably during the influent salinity increased from 0 to 10 g·L⁻¹ with the removal efficiencies about 95% and 98%, respectively. When the salinity increased to 15 g·L⁻¹ and 20 g·L⁻¹, a decrease of TOC removal was detected, which dropped to around 91%. In contrast to the decrease of TOC removal, the NH₄⁺-N removal efficiency was as high as 97% at 15 g·L⁻¹ salinity and then followed by notable decreases. By increasing the salinity to 35 g·L⁻¹, an even more prominent reduction of the TOC and NH₄⁺-N removal efficiencies was encountered. The TOC and NH₄⁺-N removal efficiencies dropped to about 83% and 70%, respectively.

It is obvious that there is no significant influence of salinity under 10 g·L⁻¹ on system performance. The system still showed a good removal at 15 and 20 g·L⁻¹ while slightly decrease was occurred. And then, a poor effluent quality was observed at 35 g·L⁻¹. This finding seems to indicate

TABLE 3: Variations and removal efficiencies of NH_4^+ -N in five IAMBRs of different salinity during steady operations.

Salinity ($\text{g}\cdot\text{L}^{-1}$)	Influent ($\text{mg}\cdot\text{L}^{-1}$)	Effluent ($\text{mg}\cdot\text{L}^{-1}$)	Removal efficiency (100%)
0	32.05 ± 11.45	0.45 ± 1.03	98.58 ± 2.51
5	32.88 ± 7.06	0.59 ± 0.60	98.19 ± 2.08
10	32.39 ± 9.48	0.47 ± 0.61	98.50 ± 2.12
15	30.91 ± 4.54	0.77 ± 0.27	97.47 ± 0.91
20	32.11 ± 4.74	2.07 ± 1.11	93.48 ± 3.56
35	31.17 ± 6.49	9.31 ± 2.39	70.12 ± 2.79

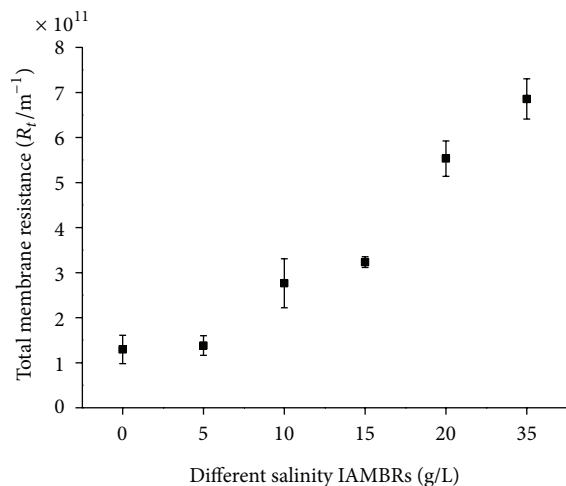


FIGURE 2: The variation of total membrane resistance at different salinity.

that elevated salinity environment leads to slow the activity of microorganisms in systems and consequently shows a lower removal. The majority of microorganisms in systems regarding as the conventional activated sludge always are the nonhalophilic [19]. They are normally able to tolerate lower salinity up to $10 \text{ g}\cdot\text{L}^{-1}$ without acclimation. Furthermore, the acclimation of microorganisms can work for salinity up to about $30 \text{ g}\cdot\text{L}^{-1}$. Nonetheless, when the salinity increased to $35 \text{ g}\cdot\text{L}^{-1}$, the higher osmotic stress would cause an outward flow of intracellular water, leading to cell dehydration and eventually plasmolysis and loss of activity of the cells for these microorganisms [20].

3.2. Evaluation of Filtration Resistance. In order to determine the membrane fouling, the filtration resistances at different salinity were analyzed (Figure 2). As is shown in Figure 2, the total membrane resistance increased gradually from $1.29 \times 10^{11} \text{ m}^{-1}$ to $6.85 \times 10^{11} \text{ m}^{-1}$ with the salinity increased from $0 \text{ g}\cdot\text{L}^{-1}$ to $35 \text{ g}\cdot\text{L}^{-1}$. It also can be seen that there was little increasing from $0 \text{ g}\cdot\text{L}^{-1}$ to $5 \text{ g}\cdot\text{L}^{-1}$ salinity, indicating a favorable toleration of membrane fouling under $5 \text{ g}\cdot\text{L}^{-1}$ salinity. However, when the salinity continuously increased to $35 \text{ g}\cdot\text{L}^{-1}$, the total membrane resistance showed a notable increasing, aggravating membrane fouling.

This implies that salinity exerts a positive impact on the membrane fouling. The membrane fouling is a complex

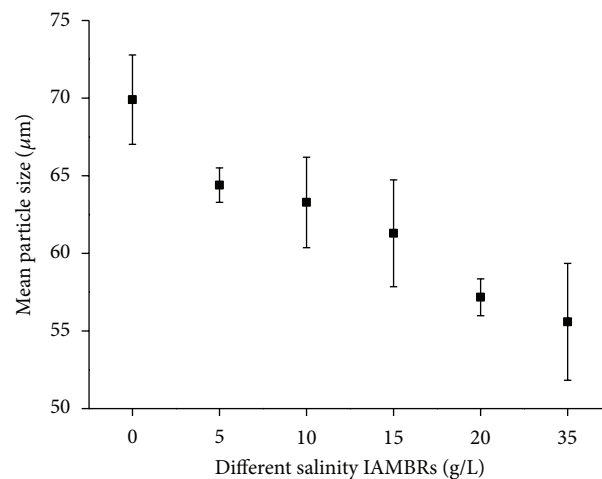


FIGURE 3: The variation of PSD at different salinity.

phenomenon in an elevated salt environment, which might be caused by inorganic fouling (main phenomenon is slat scaling), organic fouling (main phenomenon is colloidal fouling), biofouling, and their interactions. The higher salt environment can cause scaling on membrane [21] and can also aggravate colloidal fouling [22]. The deposition, growth, and metabolism of bacteria cells or flocs always result in biofouling. These findings can be reflected by sludge characteristics, such as PSD, EPS, SMP, and RH. Therefore, the sludge characteristics were further analyzed in this study to expand our knowledge of relations between sludge characteristics and membrane fouling.

3.3. Changes of PSD of Activated Sludge at Different Salinity. Variation of PSD of mixed liquors at different salinity IAMBRs is depicted in Figure 3. The mean particle size was evaluated on the basis of number of particles. It is evident that particle size decreased obviously along with increasing salinity. The particle size dropped from $69.9 \mu\text{m}$ to $55.95 \mu\text{m}$, while the salinity increased from 0 to $35 \text{ g}\cdot\text{L}^{-1}$.

In contrast to the continuous increase of total membrane resistance, the smaller particle size tended to result in higher membrane fouling. This could be explained by the The Carman-Kozeny equation (3) [23].

$$\alpha = \frac{180 \times (1 - \varepsilon)}{\rho_p d_p^2 \varepsilon^3}, \quad (3)$$

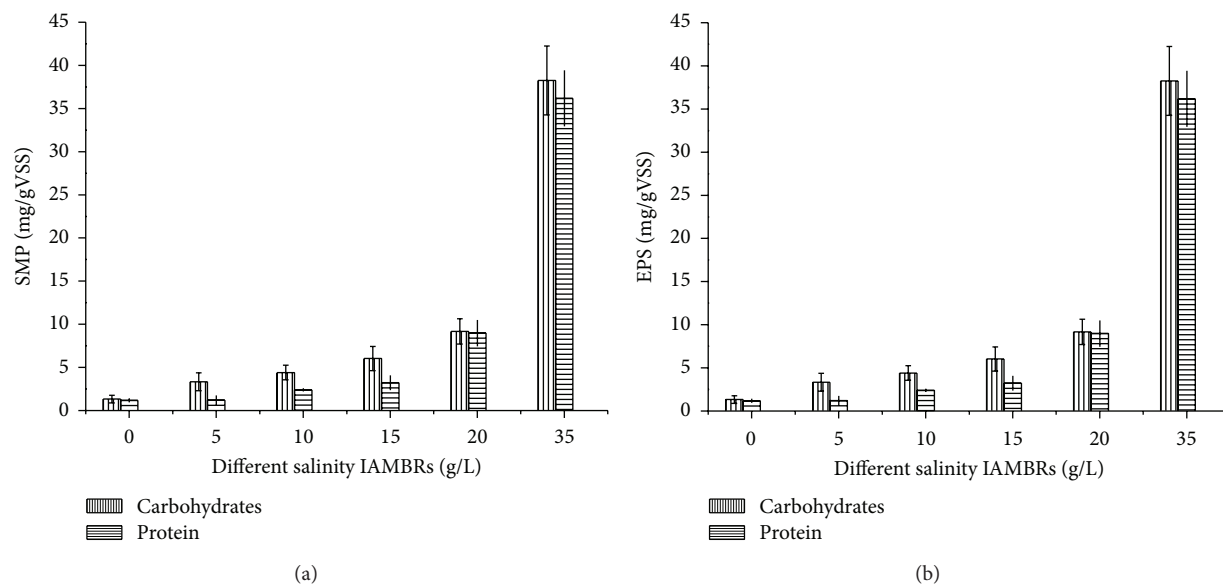


FIGURE 4: The variation of SMP (a) and EPS (b) at different salinity. The error bars show the standard deviation of the total concentrations in both (a) and (b).

where α is the specific cake resistance (m/Kg), ϵ is the cake porosity, d_p is the particle size (m), and ρ_p is the particle density (Kg/m^3).

As can be clearly seen from (3), the specific resistance of the cake layer is closely related to particle size. That is to say, the smaller particles deposit on the membrane surface/in the cake layer will cause greater specific resistance. The finding in this study corroborated that a significant decrease in particle size could intensify membrane fouling within the IAMBRs system at increased salinity. The larger particles can enlarge the void fraction of the cake [23] and then reduced the specific cake resistance according to (3). Meanwhile, larger particles cannot easily deposit onto the membrane surface at a high cross flow velocity because of the high shear force. On the contrary, the smaller particles can reduce the void fraction and can be back transported less efficiently from the membrane surface [23].

3.4. Effect of Salinity on EPS and SMP. Regarding the organic foulants, the SMP and EPS are considered as the most significant factor responsible for membrane fouling [24]. Both SMP and EPS are very heterogeneous and always consist of carbohydrates, proteins, lipids, and nucleic acids. In this study, the SMP and EPS normalized as the sum of total carbohydrates and proteins because these are the dominant components typically found in extracted SMP and EPS. Figures 4(a) and 4(b) compare the SMP and EPS concentrations at different salinity and show the average concentration of SMP and EPS in each IAMBR based on duplicate measurements.

As can be seen from Figure 4, the average concentrations of SMP and EPS increased gradually with the salinity

increased from 0 to $20\text{ g}\cdot\text{L}^{-1}$ and then followed by significant increase at $35\text{ g}\cdot\text{L}^{-1}$ salinity. For SMP, carbohydrates and proteins increased, when the salinity increased from 0 to $35\text{ g}\cdot\text{L}^{-1}$ and from 1.32 and 1.19 mg/gVSS to 38.25 and 36.19 mg/gVSS, respectively. So is EPS. The carbohydrates and proteins increased from 24.36 and 59.59 mg/gVSS to 270.19 and 324.5 mg/gVSS, respectively.

As compared to filtration resistance in Figure 2, it appears that increasing SMP and EPS is more closely related to membrane fouling. It is generally indicated that the SMP and EPS are the dominating fouling agents resulting in membrane pore blocking. Currently, more attention is paid to SMP in mixed liquors which often affect the structure and porosity of cake layer created on the membrane surface. Figure 4(a) points that the concentrations of carbohydrates in SMP are higher than these of proteins for all of 5 different salinity IAMBRs. This implies carbohydrates were identified as a majority component of SMP. The previous studies also confirmed that the concentration of carbohydrates in the mixed liquor played an important role in membrane fouling. Figure 4(b) shows the similar increasing tendency as EPS. However, the proteins exerted an adverse impact on the membrane fouling, which is higher than carbohydrates. It seems to assume that the excreted protein in mixed liquors increased with decrease in microbial activity as salinity elevated and the carbohydrate regarding as available carbon declined.

Additionally, it has to be mentioned that the SMP and EPS concentrations were significantly increased at $35\text{ g}\cdot\text{L}^{-1}$ salinity due to the more biopolymers excreted by sludge mixture. This could be in response to salt shock. Microorganisms generally accelerate endogenous respiration [25, 26] and secrete organic cellular constituents [27] at higher salinity, meaning loss of activity. Furthermore, the poor removal

efficiencies of TOC and $\text{NH}_4^+\text{-N}$ at $35\text{ g}\cdot\text{L}^{-1}$ salinity were thus mainly attributable to the lower activity of microorganisms.

3.5. Variation of RH at Different Salinity. The RH is considered as one of the main factors to reflect the characteristics of sludge mixture, which is measured as adherence to hydrocarbons. It is assumed that hydrophobic interactions and polymeric entanglement could enhance the sludge floc fractions cohesion, tending to clog membrane.

The results of variation of RH at different salinity are presented in Figure 5. It is obvious that the RH increased from 63% to 88% with the salinity increased from 0 to $20\text{ g}\cdot\text{L}^{-1}$. The result is in accordance with filtration resistance. The higher RH could lead to intensify membrane fouling. These observations are probably attributed to sludge characteristics deteriorated following increased salinity [12], resulting in an increase of the hydraulic resistance.

However, when the salinity increased to $35\text{ g}\cdot\text{L}^{-1}$, the RH dropped to 72%, quickly. This finding is incompatible with that mentioned above. The most important effect of salinity on membrane fouling in numerous research is not well established. Particularly, the membrane fouling is probably attributed to the interactions of sludge characteristics caused by salinity. Only one factor cannot reflect the reason of higher membrane fouling. The decrease of RH at higher salinity in this study is postulated to the loss of sludge activity. Figure 6 shows the change of sludge activity. The DHA was used to characterize sludge activity. It can be seen from Figure 6 that the DHA dropped quickly when the salinity increased to $35\text{ g}\cdot\text{L}^{-1}$, regarding as the loss of sludge activity. This result probably leads to the poor performance of the TOC and $\text{NH}_4^+\text{-N}$ removal and the loss of sludge activity.

4. Conclusions

This study compared the performance and the sludge characteristics in IAMBRs treating the different synthetic wastewater from 0 to $35\text{ g}\cdot\text{L}^{-1}$ salinity levels. The results of the removal of TOC and $\text{NH}_4^+\text{-N}$ showed a poor performance at higher salinity. The sludge characteristics analysis showed that filtration resistance, SMP, and EPS gradually increased following the salinity increased from 0 to $35\text{ g}\cdot\text{L}^{-1}$. Differently, the mean particle size of sludge mixture decreased with the elevated salinity. The RH increased with the salinity increased from 0 to $20\text{ g}\cdot\text{L}^{-1}$, while dropping quickly at $35\text{ g}\cdot\text{L}^{-1}$ salinity, indicating the loss of microbial activity. The membrane fouling may be attributed to the interactions of the variation of sludge characteristics caused by salinity. Therefore, the further study should be paid more attention to expand our knowledge of the relation between the membrane fouling and sludge characteristics in salinity wastewater.

Conflict of Interests

The authors declare that there is no conflict of interests regarding the publication of this paper.

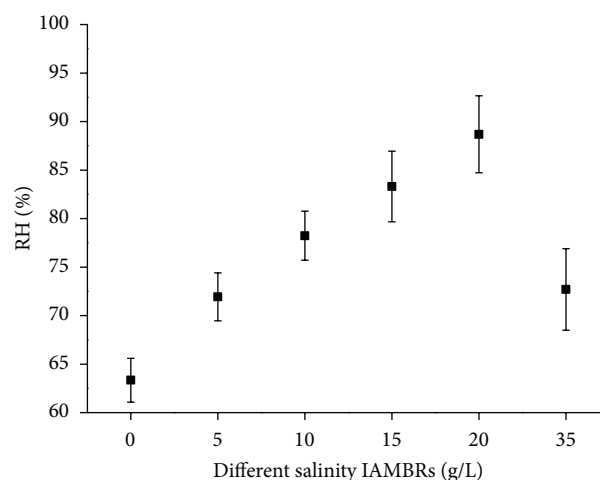


FIGURE 5: The variation of RH at different salinity.

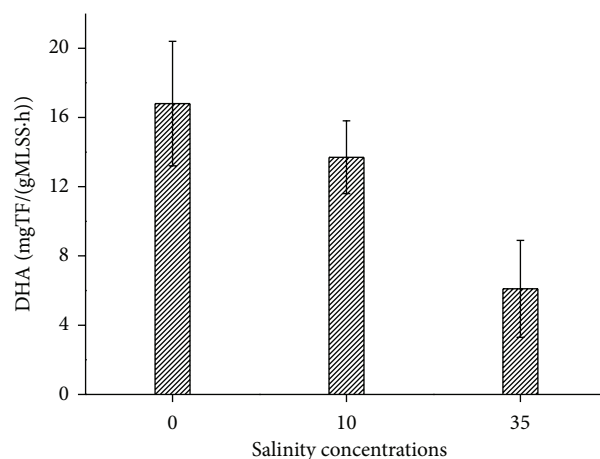


FIGURE 6: The variation of DHA at different salinity.

Acknowledgments

The authors thank the Research Fund for the Doctoral Program of University of Jinan (no. XBS1339) and the National Natural Science Foundation of China (no. 51278225) for the financial support.

References

- [1] C. Kappel, A. J. B. Kemperman, H. Temmink, A. Zwijnenburg, H. H. M. Rijnaarts, and K. Nijmeijer, "Impacts of NF concentrate recirculation on membrane performance in an integrated MBR and NF membrane process for wastewater treatment," *Journal of Membrane Science*, vol. 453, pp. 359–368, 2014.
- [2] S. Xia, J. Li, S. He et al., "The effect of organic loading on bacterial community composition of membrane biofilms in a submerged polyvinyl chloride membrane bioreactor," *Biore-source Technology*, vol. 101, no. 17, pp. 6601–6609, 2010.
- [3] F. Meng, S. Chae, A. Drews, M. Kraume, H. Shin, and F. Yang, "Recent advances in membrane bioreactors (MBRs): membrane fouling and membrane material," *Water Research*, vol. 43, no. 6, pp. 1489–1512, 2009.

- [4] H. S. You, C. C. Tseng, M. J. Peng, S. H. Chang, Y. C. Chen, and S. H. Peng, "A novel application of an anaerobic membrane process in wastewater treatment," *Water Science and Technology*, vol. 51, no. 6-7, pp. 45–50, 2005.
- [5] U. Sudarno, J. Winter, and C. Gallert, "Effect of varying salinity, temperature, ammonia and nitrous acid concentrations on nitrification of saline wastewater in fixed-bed reactors," *Bioresource Technology*, vol. 102, no. 10, pp. 5665–5673, 2011.
- [6] O. Lefebvre and R. Moletta, "Treatment of organic pollution in industrial saline wastewater: a literature review," *Water Research*, vol. 40, no. 20, pp. 3671–3682, 2006.
- [7] O. Lefebvre, S. Quentin, M. Torrijos, J. J. Godon, J. P. Delgenès, and R. Moletta, "Impact of increasing NaCl concentrations on the performance and community composition of two anaerobic reactors," *Applied Microbiology and Biotechnology*, vol. 75, no. 1, pp. 61–69, 2007.
- [8] L. S. Tam, T. W. Tang, W. Y. Leung, G. H. Chen, and K. R. Sharma, "A pilot study on performance of a membrane bioreactor in treating fresh water sewage and saline sewage in Hong Kong," *Separation Science and Technology*, vol. 41, no. 7, pp. 1253–1264, 2006.
- [9] J. Zhang, Y. Zhang, and X. Quan, "Electricity assisted anaerobic treatment of salinity wastewater and its effects on microbial communities," *Water Research*, vol. 46, no. 11, pp. 3535–3543, 2012.
- [10] D. Jang, Y. Hwang, H. Shin, and W. Lee, "Effects of salinity on the characteristics of biomass and membrane fouling in membrane bioreactors," *Bioresource Technology*, vol. 141, pp. 50–56, 2013.
- [11] M. A. H. Johir, S. Vigneswaran, J. Kandasamy, R. BenAim, and A. Grasmick, "Effect of salt concentration on membrane bioreactor (MBR) performances: detailed organic characterization," *Desalination*, vol. 322, pp. 13–20, 2013.
- [12] G. Di Bella, D. Di Trapani, M. Torregrossa, and G. Viviani, "Performance of a MBR pilot plant treating high strength wastewater subject to salinity increase: analysis of biomass activity and fouling behaviour," *Bioresource Technology*, vol. 147, pp. 614–618, 2013.
- [13] Y. Tian and X. Su, "Relation between the stability of activated sludge flocs and membrane fouling in MBR: under different SRTs," *Bioresource Technology*, vol. 118, pp. 477–482, 2012.
- [14] K. Xie, S. Xia, J. Song et al., "The effect of salinity on ammonia-oxidizing bacterial community in the Conventional Sequencing Batch Reactor (CSBR) and Intermittently Aerated Membrane Bioreactor (IAMBR)," *Fresenius Environmental Bulletin*, vol. 21, no. 1, pp. 153–162, 2012.
- [15] Chinese NEPA, *Water and Wastewater Monitoring Methods*, Chinese Environmental Science Publishing House, Beijing, China, 4th edition, 2002.
- [16] C. Nagendranatha Reddy, A. Naresh Kumar, J. Annie Modestra, and S. Venkata Mohan, "Induction of anoxic microenvironment in multi-phase metabolic shift strategy during periodic discontinuous batch mode operation enhances treatment of azo dye wastewater," *Bioresource Technology*, vol. 165, pp. 241–249, 2014.
- [17] F. Meng, F. Yang, B. Shi, and H. Zhang, "A comprehensive study on membrane fouling in submerged membrane bioreactors operated under different aeration intensities," *Separation and Purification Technology*, vol. 59, no. 1, pp. 91–100, 2008.
- [18] B. Wilén, B. Jin, and P. Lant, "The influence of key chemical constituents in activated sludge on surface and flocculating properties," *Water Research*, vol. 37, no. 9, pp. 2127–2139, 2003.
- [19] C. R. Woolard and R. L. Irvine, "Treatment of hypersaline wastewater in the sequencing batch reactor," *Water Research*, vol. 29, no. 4, pp. 1159–1168, 1995.
- [20] A. Uygur, "Specific nutrient removal rates in saline wastewater treatment using sequencing batch reactor," *Process Biochemistry*, vol. 41, no. 1, pp. 61–66, 2006.
- [21] W. C. L. Lay, Y. Liu, and A. G. Fane, "Impacts of salinity on the performance of high retention membrane bioreactors for water reclamation: a review," *Water Research*, vol. 44, no. 1, pp. 21–40, 2010.
- [22] J. H. Choi, S. H. Lee, K. Fukushi, and K. Y. Yamamoto, "Comparison of sludge characteristics and PCR-DGGE based microbial diversity of nanofiltration and microfiltration membrane bioreactors," *Chemosphere*, vol. 67, no. 8, pp. 1543–1550, 2007.
- [23] C. Ma, S. Yu, W. Shi, S. G. J. Heijman, and L. C. Rietveld, "Effect of different temperatures on performance and membrane fouling in high concentration PAC-MBR system treating micro-polluted surface water," *Bioresource Technology*, vol. 141, pp. 19–24, 2013.
- [24] F. Meng, F. Yang, J. Xiao, H. Zhang, and Z. Gong, "A new insight into membrane fouling mechanism during membrane filtration of bulking and normal sludge suspension," *Journal of Membrane Science*, vol. 285, no. 1-2, pp. 159–165, 2006.
- [25] D. F. Kincannon and A. F. Gaudy, "Response of biological waste treatment systems to changes in salt concentrations," *Biotechnology and Bioengineering*, vol. 10, pp. 483–496, 1968.
- [26] M. Ingram, "The influence of sodium chloride and temperature on the endogenous respiration of *Bacillus cereus*," *Journal of General Physiology*, vol. 23, pp. 773–778, 1940.
- [27] E. Reid, X. Liu, and S. J. Judd, "Effect of high salinity on activated sludge characteristics and membrane permeability in an immersed membrane bioreactor," *Journal of Membrane Science*, vol. 283, no. 1-2, pp. 164–171, 2006.

Research Article

Dechlorination of Hexachloroethane in Water Using Iron Shavings and Amended Iron Shavings: Kinetics and Pathways

D. L. Wu, Y. X. Liu, Z. G. Liu, and L. M. Ma

State Key Laboratory of Pollution Control and Resource Reuse, College of Environmental Science and Engineering, Tongji University, Shanghai 200092, China

Correspondence should be addressed to Z. G. Liu; lzg0532@tongji.edu.cn

Received 5 March 2014; Accepted 18 May 2014; Published 30 June 2014

Academic Editor: Chaomeng Dai

Copyright © 2014 D. L. Wu et al. This is an open access article distributed under the Creative Commons Attribution License, which permits unrestricted use, distribution, and reproduction in any medium, provided the original work is properly cited.

In contrast to previous studies which employed zero-valent iron powder, this paper investigated reductive dechlorination of hexachloroethane (HCA) using iron shavings and bimetallic iron shavings modified with Cu, Ag, or Pd. Results clearly show that iron shavings offer superior reductive dechlorination of HCA. In addition, surface-normalized pseudo first-order dechlorination rates of $0.0073 \text{ L}\cdot\text{m}^{-2}\cdot\text{h}^{-1}$, $0.0136 \text{ L}\cdot\text{m}^{-2}\cdot\text{h}^{-1}$, $0.0189 \text{ L}\cdot\text{m}^{-2}\cdot\text{h}^{-1}$, and $0.0084 \text{ L}\cdot\text{m}^{-2}\cdot\text{h}^{-1}$ were observed in the presence of iron shavings (Fe^0) and the bimetallic iron shavings Cu/Fe, Ag/Fe, and Pd/Fe, respectively. Bimetallic iron shavings consisting of Cu/Fe and Ag/Fe could greatly enhance the reductive reaction rate; Pd/Fe was used to achieve complete dechlorination of HCA within 5 hours. The additives of Ag and Pd shifted product distributions, and the reductive dechlorination of HCA occurred via β reductive elimination and sequential hydrogenolysis in the presence of all iron shavings. This study consequently designed a reaction pathway diagram which reflected the reaction pathway and most prevalent dechlorination products. Iron shavings are a common byproduct of mechanical processing plants. While the purity of such Fe metals may be low, these shavings are readily available at low costs and could potentially be used in engineering applications such as contamination control technologies.

1. Introduction

Since zero-valent iron (ZVI) was applied to perform the reductive dechlorination of chlorinated alkanes in the early 1990s [1], the use of ZVI to treat contaminants has been an attractive research topic [2, 3]. As a result, numerous relevant studies have been performed on such reductive transformation of contaminants including aromatic compounds [4], heavy metals [5, 6], radioactive pollutant [7], and azo dyes [8]. Iron media have also been investigated for remediation of nitrate in contaminated groundwater [9]. Possible mechanisms considered for contaminant reduction on iron media include (i) direct reduction at the metal surface, possibly via pitting in the oxide surface, (ii) reduction by Fe(II) formed in situ, and (iii) reduction by atomic hydrogen [10, 11].

In order to enhance the reactivity and functionality of ZVI, depositing the other metals such as Ni, Cu, Pt, or Pd as a catalyst onto the iron surface leads to the synthesis of bimetallic iron particles. Fennelly and Roberts employed individual metals and several bimetals (Ni/Fe, Cu/Fe) to

investigate the reductive degradation of 1,1,1-trichloroethane (1,1,1-TCA) [12]; this work proved that bimetals can not only boost the dechlorination reaction rate, but they can also exert a large influence on the types of final products. In addition, there have been many reports concerning the use of nanoscale ZVI and nanoscale bimetallic iron to study the reductive treatment of pollutants [13–15]. Nanoscale iron has high dechlorination reactivity but it is very costly to produce and also highly vulnerable to inactivation and aggregation.

The most relevant prior research has focused on the use of ZVI powder or nanoscale iron to investigate the reductive transformation of contaminants in groundwater. But iron powder and nanoscale-iron consist of extremely fine particles; they readily form inactive films. Iron shavings, which are a common solid waste generated in many mechanical processing plants with an abundant local supply and relatively low cost are a superior reducing agent. In actual engineering applications, iron shavings offer stable long-term performance. Ma and Zhang have already employed filler produced from iron shavings in large-scale engineering

applications containing 910,000 kilograms of iron shavings (60,000 m³/d), which have chiefly consisted of industrial wastewater pretreatment, and the material has been shown to improve wastewater biodegradability [16]. However, there has been no systematic research on the specific reaction processes and detailed mechanisms when iron shavings are used to perform the reductive transformation of pollutants. Works on the amended iron shavings by Cu, Ag, and Pd are very limited as well, particularly, the Ag/Fe bimetallic iron. One of the primary goals of this study is to fill this gap. Wüst et al. observed a combined zero- and first-order kinetic model in describing the dechlorination of TCE and *cis*-DCE by ZVI [17]. Arnold and Roberts adapted a modified Langmuir-Hinshelwood-Hougen-Watson (LHHW) kinetic model to describe iron mediated dechlorination of chlorinated ethylene and acetylene [18]. However, reported reaction rates for various chlorinated compounds are highly variable among different investigators.

The characteristics of iron shavings differed from iron powder greatly, and there has been no research reports concerning the potential reduction processes and mechanisms of chlorinated hydrocarbons by iron shavings. Furthermore, because most past research on reaction kinetics focused on the overall kinetics of removal of parent compounds, there has been limited research on the entire kinetics of final reaction products and intermediate products. This study uses iron shavings, which possess tremendous engineering application potential, as the main reducing agent, and compares the reaction performance of iron shavings and conventional iron powder. Taking hexachloroethane as the target pollutant, the reductive reactivity of iron shavings and bimetallic iron shavings was investigated in batch experiments, as well as the detailed entire reaction kinetics, reaction products, and pathways. This study might facilitate the development of iron shaving wastewater treatment techniques by providing a full-scale understanding of the mechanism that iron shavings bring about on the reductive transformation of pollutants.

2. Experimental Section

2.1. Materials and Reagents. The chief experimental material consisted of metallic iron shavings, which were obtained from the machine shop at Tongji University; the shavings made of 38CrMoAl steel, with a carbon content of approximately 0.3-0.4%, also contained trace elements, including Si, Mn, Cr, Mo, and Al (detailed elemental composition is shown in Table 1). A lathe was used to cut the iron into curly shavings with a width of 0.5-1.0 cm, length of 3-10 cm, and thickness of 0.2 mm. The specific surface area of the iron shavings was 0.3 m²/g (tested by application of the Brunauer-Emmett-Teller (BET)); the appearance of the shavings is shown in Figure 1. The experiment used 100 mL reaction bottles (marked volume of 100 mL, actual volume of roughly 120 mL) to ensure that the reaction occurred in a tightly sealed vessel, and 1 mL gas-tight sample collectors were used to collect samples for analysis. Deionized water from Milli-Q (Millipore Corp.) deoxygenated by purging with high-purity N₂ was used in all experiments. The reagents of

TABLE 1: Elemental composition of iron shavings used (%).

Elemental	Content (wt%)
Fe	>95
C	0.35~0.42
Si	0.2~0.45
Mn	0.3~0.6
Cr	1.35~1.65
Mo	0.15~0.25
Al	0.70~1.10



FIGURE 1: Image of the unwashed shavings (38#CrMoAl steel).

hexachloroethane, pentachloroethane, tetrachloroethylene, trichloroethylene, and dichloroethylene were all HPLC grade and were purchased from the Sigma Company. The NaOH, NaHCO₃, HCl, CuSO₄, AgNO₃, and PdCl₂ used in this study were analytically pure and were purchased from the Sinopharm Chemical Reagent Co., Ltd. All chemicals were used as received. The purity of the iron powder was 99%; it was purchased from the Shanghai Runjie Chemical Reagent Co., Ltd.

2.2. Methods. Stock solutions of hexachloroethane were prepared in methanol. 20 μL of stock solution was spiked into 1000 mL of aqueous solution to achieve the desired initial concentration. Iron shavings were washed in NaHCO₃ solution to remove any surface oil or grease and were soaked in water for several days to allow the surface to rust. The rusty iron shavings were then washed in deaerated 0.1 mol/L hydrochloric acid (HCl) and rinsed 5 times with deaerated water. 50 g of the shavings was packed into reaction bottles with marked volume of 100 mL, and an aqueous solution of hexachloroethane with a predetermined concentration was added. The bottles were immediately sealed using Teflon-coated stoppers and crimp-sealed with aluminum foil caps to provide a better seal. The reaction bottles were placed in a water bath on a constant temperature shaking incubator, which shook at a constant rate of 180 r/min. Each experiment was performed in triplicate including a set of control vials

containing the introduced hexachloroethane solution with the same concentration as that used in the experiment but without iron, and a set of blank vials containing only the iron and deaerated Milli-Q water. At intervals, gas-tight sample collectors were used to take samples for analysis of reactants and their transformation products. Each sample was 1 mL; the samples were then rapidly added to automatic sampling bottles containing 29 mL of deionized water for analysis by purge and trap-gas chromatograph. Analysis of organic carbon mass in the controls indicated that the mass varied by less than 5% over the course of a typical experiment.

Preparation of Cu/Fe, Ag/Fe, and Pd/Fe bimetallic iron shavings. The bimetallic iron shavings were prepared using a chemical deposition method by soaking the iron shavings in CuSO_4 , AgNO_3 , and PdCl_2 solutions, respectively, which involved the deposition of 0.1 wt% of the other metals on the surface of the iron shavings. In this method, CuSO_4 , AgNO_3 , and PdCl_2 solutions with desired concentrations were added to reaction bottles filled with 50 g of iron shavings. After reaction, it is assumed that all the other metals were coated on the iron shavings to give 0.1% Cu, Ag, and Pd by weight, respectively. These shavings after being washed were added to hexachloroethane-water solutions employing the same method as described above, and samples were taken at fixed intervals for analysis.

2.3. Analysis. Qualitative and quantitative analyses of chlorinated alkanes were performed using XPT-GC/MS (purge and trap-gas chromatography/mass spectrometry). A TEKMAR AQUAteK70 automatic sampler was used to inject samples, with a sample volume of 5 mL. Pretreatment conditions in the purge and trap concentrator: Purge time: 11 minutes; purge temperature: room temperature (25°C); purge gas flow: 40 mL/min (high-purity N_2). Dry purge time: 1 min; preheating temperature: 245°C ; sample inject temperature: 180°C ; furnace temperature: 150°C ; transmission line temperature: 150°C . GC/MS analytical conditions: US Thermal GC/MS multipurpose instrument equipped with HP-5 capillary tube column (inner diameter: 0.25 mm, liquid film thickness: $0.25\ \mu\text{m}$); length: 30 m; carrier gas: high-purity He, flow rate: 1.0 mL/min. The temperature program was initiated at a temperature of 35°C for 5 minutes, heating rate: $25^\circ\text{C}/\text{min}$, and final temperature: 200°C held for 1 minute. Sampler temperature: 200°C , ions source temperature: 250°C ; MS transmission line temperature: 250°C . The sample was automatically injected with a split ratio of 10 : 1.

3. Results and Discussion

3.1. Reductive Dechlorination of HCA by Various Iron Shavings. When investigating the reductive dechlorination reaction rate of HCA in presence of various iron shavings, the study focused on the effect of iron powder (Fe^0), iron shavings (Fe^0), and bimetallic iron shavings (Cu/Fe, Ag/Fe, Pd/Fe) on the rate of reductive dechlorination of HCA. Because the specific surface area of iron powder is $5.4\ \text{m}^2/\text{g}$, while that of iron shavings is $0.3\ \text{m}^2/\text{g}$, in order to ensure that the iron powder and iron shavings in reactor had the same surface

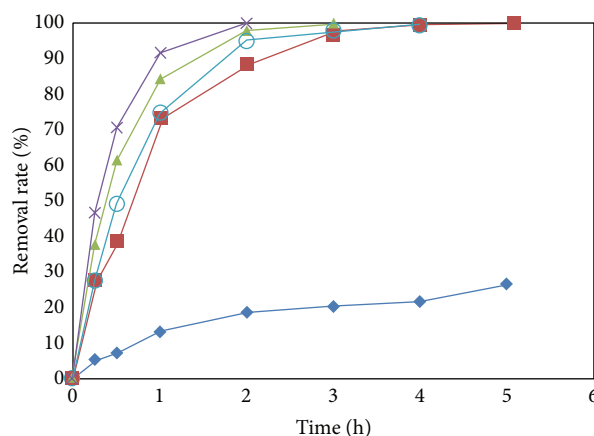


FIGURE 2: Removal rate of HCA obtained with various iron shavings. Initial concentration of HCA was $60\ \mu\text{mol}\cdot\text{L}^{-1}$. (◆) Fe^0 (powder), (■) Fe^0 (shavings), (○) Pd/Fe (0.1 wt%), (▲) Cu/Fe (0.1 wt%), (×) Ag/Fe (0.1 wt%).

area, 2.78 g of iron powder was added to the bottle. As shown in Figure 2, because HCA is highly chlorinated, it readily gave rise to reductive dechlorination by iron, and relatively high reaction rates were observed in all of the iron shavings system. However, it is clearly demonstrated that HCA removal rates observed in the presence of iron shavings are much more than those obtained in the presence of iron powder. This implies that, insofar as the specific surface area of the iron is the same, iron shavings possess better reductive activity than iron powders. The primary mechanism of organic chloride compound dechlorination is thought to be an electron transfer from ZVI to the chloride organic compound [1, 19]. Thus, the electron transfer at the iron's surface is certainly a probable process for HCA dechlorination in this system and is assumed to be the reaction mechanism in this paper. Presumably, many elementals that also consist of iron shavings can serve as the cathode to accelerate electron transfer from iron to organics and lead to the improvement of dechlorination reactions.

Identification of reaction products indicated that the variety of bimetallic iron shavings products could shift the product distributions. Figures 3–6 showed the concentration of different substances as a function of time during reductive dechlorination of HCA. The initial HCA concentration was $50\ \mu\text{mol}\cdot\text{L}^{-1}$. HCA that underwent reductive dechlorination at a very fast rate was observed in the Fe^0 (shavings) reduction system. The HCA removal rate reached 90% after 2 h of reaction time, and the chief reaction product was perchloroethylene (PCE). PCE underwent an extremely slow reductive dechlorination reaction in the presence of Fe^0 alone, and almost no dechlorination products of PCE were observed within 5 h. It can be seen from Figure 4 that the HCA reacted at an even faster rate in the Cu/Fe reduction system when compared with the Fe^0 alone, and the HCA removal rate reached 80% within 0.5 h. As before, the chief reaction product was also PCE. Because PCE underwent reductive dechlorination at an extremely slow rate in the Cu/Fe system, the PCE did not continue to undergo reductive dechlorination, forming

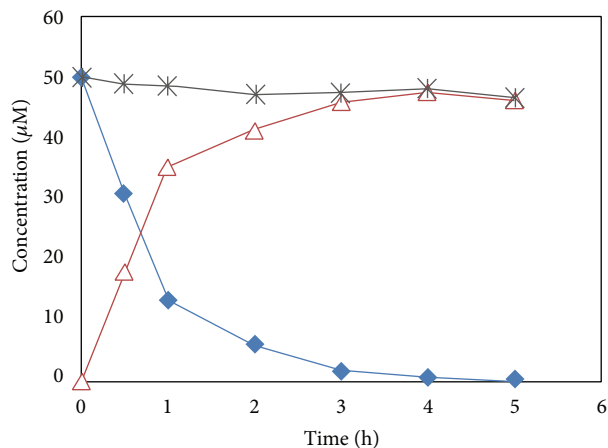


FIGURE 3: Dechlorination of HCA obtained with iron shavings alone. Initial concentration of HCA was $50 \mu\text{mol}\cdot\text{L}^{-1}$ and dosage of iron shavings was $500 \text{ g}\cdot\text{L}^{-1}$. (\blacklozenge) HCA, (\triangle) PCE, ($*$) mass balance (control).

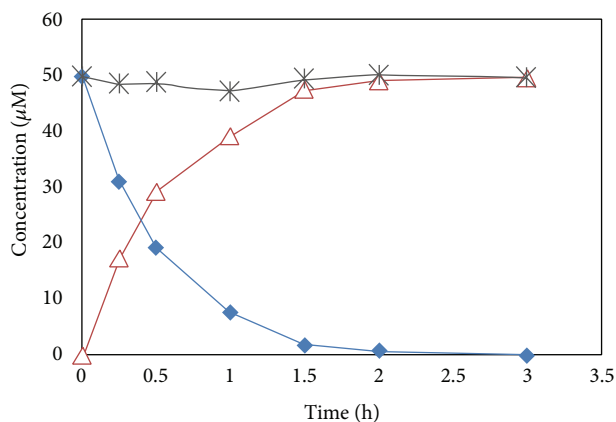


FIGURE 4: Dechlorination of HCA obtained with Cu/Fe (0.1 wt%). Initial concentration of HCA was $50 \mu\text{mol}\cdot\text{L}^{-1}$ and dosage of amended iron shavings was $500 \text{ g}\cdot\text{L}^{-1}$. (\blacklozenge) HCA, (\triangle) PCE, ($*$) mass balance (control).

other products within the time allotted for the experiment. However, the removal rate of HCA was found to be faster by Cu/Fe than by Fe^0 alone.

Figure 5 clearly reveals that HCA is reduced even faster in the Ag/Fe system than in the Fe^0 and Cu/Fe reduction systems. The products are more complex, because the chief reductive dechlorination product, PCE, can continue to undergo reductive dechlorination to form products such as TCE and DCE. The chief reduction products of a dilute HCA solution with Ag/Fe consist of PCE, TCE, and DCE. In addition, since DCE is ordinarily composed of the two isomers—*cis*-DCE and *trans*-DCE—HCA, it has a relatively complex reaction pathway. The addition of Ag can accelerate the dechlorination rate of HCA and PCE significantly, achieving nearly 100% removal rate within 2 h and 6 h, respectively, at a near neutral pH. Previous researches have shown that in

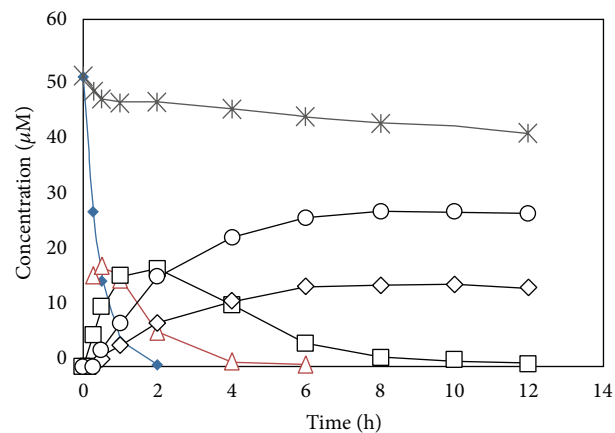


FIGURE 5: Dechlorination of HCA obtained with Ag/Fe (0.1 wt%). Initial concentration of HCA was $50 \mu\text{mol}\cdot\text{L}^{-1}$ and dosage of amended iron shavings was $500 \text{ g}\cdot\text{L}^{-1}$. (\blacklozenge) HCA, (\triangle) PCE, (\square) TCE, (\diamond) *trans*-DCE, (\circ) *cis*-DCE, ($*$) mass balance (control).

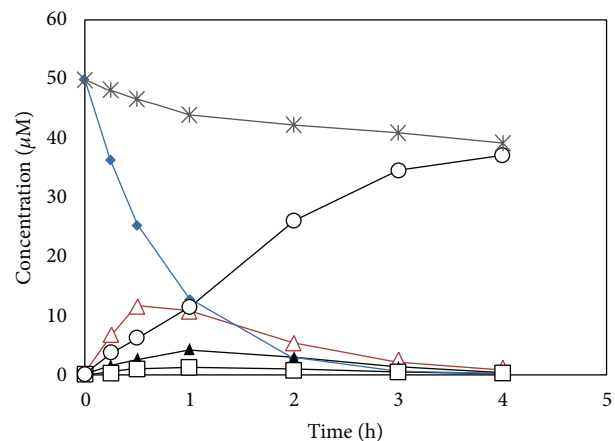


FIGURE 6: Dechlorination of HCA obtained with Pd/Fe (0.1 wt%). Initial concentration of HCA was $50 \mu\text{mol}\cdot\text{L}^{-1}$ and dosage of amended iron shavings was $500 \text{ g}\cdot\text{L}^{-1}$. (\blacklozenge) HCA, (\triangle) PCE, (\blacktriangle) TCE, (\square) DCE, (\circ) C_2H_4 , ($*$) mass balance (control).

bimetallic iron system, other metals can serve as a cathode to accelerate electron transfer from iron [20].

The dechlorination of HCA by Pd/Fe was shown in Figure 6. Unlike the Fe alone, Cu/Fe, and Ag/Fe materials, the chief reduction product of HCA with Pd/Fe is ethylene, and the chief intermediate products are PCE and TCE. This indicates that the dechlorination of HCA first occurs β reductive elimination forming PCE, and then quickly undergoes sequential hydrogenolysis to TCE, and TCE is in turn rapidly dechlorinated to ethylene. Compared with the Fe^0 , Cu/Fe, and Ag/Fe, HCA is even more thoroughly dechlorinated in the Pd/Fe catalytic reduction system, and the final product is the chlorine-free substance, ethylene. Research literature indicates that Pd is an excellent hydrogenation catalyst and can achieve the complete reductive dechlorination of chlorinated organic compounds without producing chlorine-containing compounds. The H generated by iron corrosion

can be catalyzed on the Pd surface to produce atomic hydrogen (H^*) for the chlorinated compounds dechlorination via Pd-catalyzed hydrodechlorination reactions [21]. The use of palladium-plated iron shavings in this research similarly caused HCA to undergo a fully dechlorinated reaction yielding the final product, ethylene. Bimetallic irons are frequently more reactive towards organohalides than unamended iron and can also alter product distributions. Cwiertny et al. demonstrated that not all additives enhanced rates of 1,1,1-trichloroethane (1,1,1-TCA) reduction nor was there any clear periodic trend in the observed reactivity [22]. And results suggested that absorbed atomic hydrogen, rather than galvanic corrosion, is responsible for the enhanced reactivity of bimetallic reductants.

3.2. Reaction Kinetics. The reduction of chlorinated organic compounds by the iron shavings is a typical solid-liquid interface reaction and has the following main reaction formula:



In the reaction process, solid Fe^0 is always in excess. The vast majority of surface reactions can be described using the Langmuir-Hinshelwood kinetics model. When the reaction takes place in a dilute solution of the reactants, the reaction rate equation can be expressed as

$$-\frac{dC}{dt} = kbC = K_{obs}C. \quad (2)$$

In this equation, K_{obs} is the observed reaction rate constant, which is the experimental reaction rate constant, and C represents the concentration of reactants. It is well established that the pseudo first-order kinetics could be applied in the reductive dechlorination of chlorinated organics by ZVI and bimetallic iron [1, 23]. While a dilute solution of HCA will quickly undergo a reductive dechlorination reaction by any of the iron shavings. The first step in the reductive dechlorination of HCA is β reductive elimination, which yields PCE. Unlike Fe^0 , Cu/Fe, or Pd/Fe, the reductive dechlorination of HCA by Ag/Fe is consequently a reaction network comprising of both one-way continuous reactions and parallel reactions as in Figure 7.

We can write the following reaction rate equations for each species based on the above pathway:

$$\frac{d[HCA]}{dt} = -k_1[HCA], \quad (3)$$

$$\frac{d[PCE]}{dt} = k_1[HCA] - k_2[PCE], \quad (4)$$

$$\frac{d[TCE]}{dt} = k_2[PCE] - (k_3 + k_4)[TCE], \quad (5)$$

$$\frac{d[trans-DCE]}{dt} = k_3[TCE], \quad (6)$$

$$\frac{d[cis-DCE]}{dt} = k_4[TCE]. \quad (7)$$

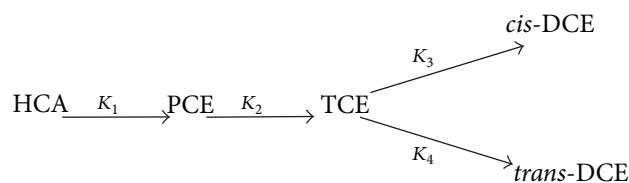


FIGURE 7: Reaction pathways for HCA reduction by Ag/Fe.

Solving (3), (4), and (5) yields

$$\begin{aligned} [HCA] &= [HCA]_0 e^{-k_1 t}, \\ [PCE] &= \frac{k_1}{k_2 - k_1} \left(e^{-k_1 t} - e^{-k_2 t} \right) [HCA]_0, \\ [TCE] &= k_1 k_2 [HCA]_0 \\ &\times \left\{ \frac{e^{-k_1 t}}{(k_1 - k_2)(k_1 - k_3 - k_4)} \right. \\ &\quad + \frac{e^{-k_2 t}}{(k_2 - k_1)(k_2 - k_3 - k_4)} \\ &\quad \left. + \frac{e^{-(k_3 + k_4)t}}{(k_3 + k_4 - k_1)(k_3 + k_4 - k_2)} \right\}. \end{aligned} \quad (8)$$

Zhou et al. have established the entire kinetics of 2,4,6-trichlorophenol by Pd/Fe including parent compounds and daughter compounds [21]. In accordance with data from dechlorination experiments using individual species of HCA, PCE, and TCE, we can derive that $K_1 = 2.842 \text{ h}^{-1}$, $K_2 = 1.251 \text{ h}^{-1}$, and $K_3 + K_4 = 0.463 \text{ h}^{-1}$. Following product analysis, it was found that in this experiment the mole ratio of the products *cis*-DCE and *trans*-DCE was 2.1, and therefore $K_3/K_4 = 2.1$. It can then be calculated that $K_3 = 0.149 \text{ h}^{-1}$ and $K_4 = 0.314 \text{ h}^{-1}$. When $[HCA]_0 = 50 \mu\text{mol} \cdot \text{L}^{-1}$ and all K values are substituted into the foregoing reaction kinetics equations, one obtains

$$\begin{aligned} [HCA] &= 50e^{-2.842t}, \\ [PCE] &= 89 \left(e^{-1.251t} - e^{-2.842t} \right), \\ [TCE] &= 47e^{-2.842t} - 142e^{-1.251t} + 95e^{-0.463t}. \end{aligned} \quad (9)$$

According to the mass balance,

$$\begin{aligned} [HCA]_0 &= [HCA] + [PCE] + [TCE] \\ &\quad + [cis-DCE] + [trans-DCE]. \end{aligned} \quad (10)$$

One obtains

$$\begin{aligned} [trans-DCE] &= 0.323 \left(50 - 8e^{-2.842t} + 53e^{-1.251t} \right. \\ &\quad \left. - 95e^{-0.463t} \right), \\ [cis-DCE] &= 0.677 \left(50 - 8e^{-2.842t} + 53e^{-1.251t} \right. \\ &\quad \left. - 95e^{-0.463t} \right). \end{aligned} \quad (11)$$

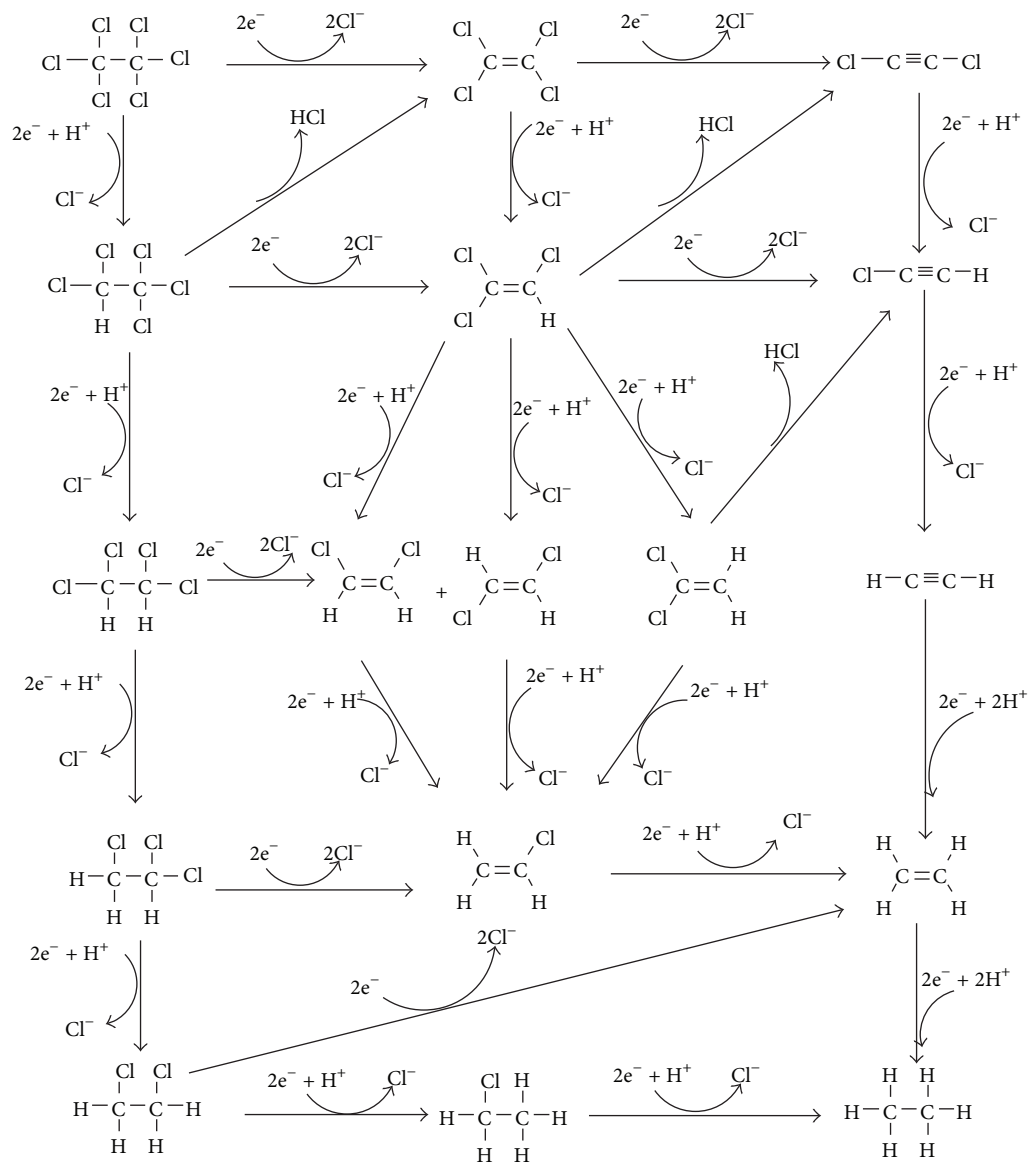


FIGURE 8: Proposed pathway for the dechlorination of HCA by iron shavings and amended iron shavings.

As a result, the entire reaction kinetics of the reductive dechlorination of an HCA solution with an initial concentration of $50 \mu\text{mol}\cdot\text{L}^{-1}$ in the presence of Ag/Fe can be expressed using the foregoing equations, in this way the curve expressed by the kinetics equation fits the experimental data. Similarly, the kinetics of HCA reduction by various iron shavings could be calculated according to reaction pathways. All the kinetic equations were summarized in Table 2.

After normalization of the surface of the iron shavings, the rate constants K_{SA} are $0.0073 \text{ L}\cdot\text{m}^{-2}\cdot\text{h}^{-1}$, $0.0136 \text{ L}\cdot\text{m}^{-2}\cdot\text{h}^{-1}$, $0.0189 \text{ L}\cdot\text{m}^{-2}\cdot\text{h}^{-1}$, and $0.0084 \text{ L}\cdot\text{m}^{-2}\cdot\text{h}^{-1}$, respectively. It was found that the Ag/Fe and Cu/Fe could enhance reductive dechlorination of HCA obviously. The Cu/Fe can speed up the reaction rate nearly twofold, and the Ag/Fe can increase it about 3 times compared to iron shavings alone. While the Pd/Fe catalytic material has relatively little effect on the HCA removal rate, however, it

can make HCA dechlorination to nonchlorinated products due to Pd as an excellent hydrogenation catalyst.

3.3. Intermediate Products and Reaction Pathways. Fennelly and Roberts observed different 1,1,1-trichloroethane (1,1,1-TCA) product distributions in Ni/Fe and Cu/Fe systems [12]. In order to perform a thorough evaluation of the products resulting from the reductive dechlorination of HCA, a high-concentration aqueous solution of HCA was prepared and the GC/MS system was used. The results of this experiment clearly indicated that, apart from transformation to PCE via β reductive elimination, HCA can also undergo hydrogenolysis to produce pentachloroethane (PCA) and tetrachloroethane (TeCA) and then trichloroethane (TCA) and dichloroethane (DCA). Furthermore, PCE also undergoes further dechlorination in the Ag/Fe and Pd/Fe reduction systems via hydrogenolysis yielding other products such

TABLE 2: Reaction pathways, kinetics for HCA reduction by Fe⁰ (shavings), Cu/Fe, Ag/Fe, and Pd/Fe.

Iron shavings	Pathway	K_n values	Equations for each substance
Fe ⁰ (shavings)	$\text{HCA} \xrightarrow{\kappa_1} \text{PCE}$	$K_1 = 1.098 \text{ h}^{-1}$	$[\text{HCA}] = 50e^{-1.098t}$ $[\text{PCE}] = 50(1 - e^{-1.098t})$
Cu/Fe	$\text{HCA} \xrightarrow{\kappa_1} \text{PCE}$	$K_1 = 2.044 \text{ h}^{-1}$	$[\text{HCA}] = 50e^{-2.044t}$ $[\text{PCE}] = 50(1 - e^{-2.044t})$
Ag/Fe	$\begin{array}{c} \text{HCA} \xrightarrow{\kappa_1} \text{PCE} \xrightarrow{\kappa_2} \text{TCE} \\ \text{PCE} \xrightarrow{\kappa_3} \text{cis-DCE} \\ \text{TCE} \xrightarrow{\kappa_4} \text{trans-DCE} \end{array}$	$K_1 = 2.842 \text{ h}^{-1}$ $K_2 = 1.251 \text{ h}^{-1}$ $K_3 = 0.149 \text{ h}^{-1}$ $K_4 = 0.314 \text{ h}^{-1}$	$[\text{HCA}] = 50e^{-2.842t}$ $[\text{PCE}] = 89(e^{-1.251t} - e^{-2.842t})$ $[\text{TCE}] = 47e^{-2.842t} - 142e^{-1.251t} + 95e^{-0.463t}$ $[\text{trans-DCE}] = 0.323(50 - 8e^{-2.842t} + 53e^{-1.251t} - 95e^{-0.463t})$ $[\text{cis-DCE}] = 0.677(50 - 8e^{-2.842t} + 53e^{-1.251t} - 95e^{-0.463t})$
Pd/Fe	$\text{HCA} \xrightarrow{\kappa_1} \text{PCE} \xrightarrow{\kappa_2} \text{TCE} \xrightarrow{\kappa_3} \text{C}_2\text{H}_4$	$K_1 = 1.267 \text{ h}^{-1}$ $K_2 = 0.978 \text{ h}^{-1}$ $K_3 = 1.41 \text{ h}^{-1}$	$[\text{HCA}] = 50e^{-1.267t}$ $[\text{PCE}] = 219(e^{-0.978t} - e^{-1.267t})$ $[\text{TCE}] = -1500e^{-1.267t} + 496e^{-0.978t} + 1004e^{-1.41t}$ $[\text{C}_2\text{H}_4] = 50 + 1669e^{-1.267t} - 715e^{-0.978t} - 1004e^{-1.41t}$

as trichloroethylene (TCE), dichloroethylene (DCE), vinyl chloride (VC), and ethylene. The reduction of PCE by β -elimination produces dichloroacetylene (DCAc), which can be further reduced to chloroacetylene (CAc) and then acetylene [24]. Reduction products are consequently highly dependent on the bimetallic materials.

In Ag/Fe reduction systems, as many as 10 species may be presented, including some products of side reactions. Determination of how these dechlorination products are generated is an extremely significant issue in research on the reaction pathway and reaction mechanism for the reductive dechlorination of HCA by various iron shavings. The proposed degradation pathways of HCA with various iron shavings based on the detected dechlorination products and the theoretical derivation were shown in Figure 8.

Results suggest that the pathway of the reductive dechlorination of HCA by iron shavings was found to be predominantly reductive β elimination. Apart from this, hydrogenolysis and dehydrochlorination reactions also occur. Previous research showed that the chemical degradation of chlorinated hydrocarbons also progressed with a stepwise dehalogenation mechanism [1]. Reductive β elimination has been shown to be a preferential pathway for compounds possessing α , β -pairs of chlorine atoms [25, 26], while hydrogenolysis or reductive α elimination is the primary transformation pathway for compounds possessing only α -chlorines [12, 27]. In addition, dehydrohalogenation becomes important under basic conditions [28].

4. Conclusions

The presented study gave insight into the entire dechlorination kinetics and dechlorination pathways of HCA by iron shavings and amended iron shavings. Iron shaving is a more effective reducing agent than traditional iron powder that is used in early research for dechlorination of HCA in water. The deposition of Cu, Ag, and Pd on the surface of iron shavings was found to significantly increase the rate of HCA reduction, Ag/Fe shavings increased the HCA reduction rate nearly threefold compared to iron shavings alone, and Pd/Fe shavings can promote the complete reductive dechlorination of HCA within 4 h, yielding products containing no chlorine. The dechlorination of HCA by all types of iron shavings followed pseudo first-order reaction kinetics. The pathway of reductive dechlorination of HCA predominantly consists of β reductive elimination, and hydrogenolysis and dehydrochlorination reactions also occur. Iron shavings are widely available inexpensive waste products and possess good reactivity and longevity usage in treatment of wastewater, and they can be readily used in engineering applications.

Conflict of Interests

The authors declare that there is no conflict of interests regarding the publication of this paper.

Acknowledgments

This work was financially supported by the Natural Science Foundation of China (Grant nos. 41172210, 50808136), the Fundamental Research Funds for the Central Universities (no. 0400219188), and the National Key Technology R&D Program (no. 2013BAC01B01).

References

- [1] L. J. Matheson and P. G. Tratnyek, "Reductive dehalogenation of chlorinated methanes by iron metal," *Environmental Science and Technology*, vol. 28, no. 12, pp. 2045–2053, 1994.
- [2] D. L. Wu, H. W. Wang, J. H. Fan, and L. M. Ma, "Catalytic reduction of CCl₄ in water by Fe⁰ and amended Fe⁰," *Huanjing Kexue/Environmental Science*, vol. 29, no. 12, pp. 3433–3438, 2008.
- [3] X. Zhang, B. Deng, J. Guo, Y. Wang, and Y. Lan, "Ligand-assisted degradation of carbon tetrachloride by microscale zero-valent iron," *Journal of Environmental Management*, vol. 92, no. 4, pp. 1328–1333, 2011.
- [4] B. Jafarpour, P. T. Imhoff, and P. C. Chiu, "Quantification and modelling of 2,4-dinitrotoluene reduction with high-purity and cast iron," *Journal of Contaminant Hydrology*, vol. 76, no. 1-2, pp. 87–107, 2005.
- [5] M. Gheju, "Hexavalent chromium reduction with zero-valent iron (ZVI) in aquatic systems," *Water, Air, and Soil Pollution*, vol. 222, no. 1–4, pp. 103–148, 2011.
- [6] N. Melitas, J. Wang, M. Conklin, P. O'Day, and J. Farrell, "Understanding soluble arsenate removal kinetics by zerovalent iron media," *Environmental Science and Technology*, vol. 36, no. 9, pp. 2074–2081, 2002.
- [7] C. Noubactep, K. B. D. Btatkeu, and J. B. Tchatchueng, "Impact of MnO₂ on the efficiency of metallic iron for the removal of dissolved Cr^{VI}, Cu^{II}, Mo^{VI}, S^{bV}, U^{VI} and Zn^{II}," *Chemical Engineering Journal*, vol. 178, pp. 78–84, 2011.
- [8] J. A. Mielczarski, G. M. Atenas, and E. Mielczarski, "Role of iron surface oxidation layers in decomposition of azo-dye water pollutants in weak acidic solutions," *Applied Catalysis B: Environmental*, vol. 56, no. 4, pp. 289–303, 2005.
- [9] S. Mossa Hosseini, B. Ataie-Ashtiani, and M. Kholghi, "Nitrate reduction by nano-Fe/Cu particles in packed column," *Desalination*, vol. 276, no. 1–3, pp. 214–221, 2011.
- [10] J. Klausen, S. P. Trober, S. B. Haderlein, and R. P. Schwarzenbach, "Reduction of substituted nitrobenzenes by Fe(II) in aqueous mineral suspensions," *Environmental Science and Technology*, vol. 29, no. 9, pp. 2396–2404, 1995.
- [11] A. M. Moore, C. H. De Leon, and T. M. Young, "Rate and extent of aqueous perchlorate removal by iron surfaces," *Environmental Science and Technology*, vol. 37, no. 14, pp. 3189–3198, 2003.
- [12] J. P. Fennelly and A. L. Roberts, "Reaction of 1,1,1-trichloroethane with zero-valent metals and bimetallic reductants," *Environmental Science and Technology*, vol. 32, pp. 1980–1988, 1998.
- [13] C. B. Wang and W. X. Zhang, "Synthesizing nanoscale iron particles for rapid and complete dechlorination of TCE and PCBs," *Environmental Science and Technology*, vol. 31, no. 7, pp. 2154–2156, 1997.
- [14] J. Zhang, Z. Hao, Z. Zhang, Y. Yang, and X. Xu, "Kinetics of nitrate reductive denitrification by nanoscale zero-valent iron,"

- Process Safety and Environmental Protection*, vol. 88, no. 6, pp. 439–445, 2010.
- [15] Y. H. Shih, C. Y. Hsu, and Y. F. Su, “Reduction of hexachlorobenzene by nanoscale zero-valent iron: kinetics, pH effect, and degradation mechanism,” *Separation and Purification Technology*, vol. 76, no. 3, pp. 268–274, 2011.
- [16] L. Ma and W. X. Zhang, “Enhanced biological treatment of industrial wastewater with bimetallic zero-valent iron,” *Environmental Science and Technology*, vol. 42, no. 15, pp. 5384–5389, 2008.
- [17] W. F. Wüst, R. Köber, O. Schlicker, and A. Dahmke, “Combined zero- and first-order kinetic model of the degradation of tce and cis-DCE with commercial iron,” *Environmental Science and Technology*, vol. 33, no. 23, pp. 4304–4309, 1999.
- [18] W. A. Arnold and A. L. Roberts, “Pathways and kinetics of chlorinated ethylene and chlorinated acetylene reaction with Fe(0) particles,” *Environmental Science and Technology*, vol. 34, no. 9, pp. 1794–1805, 2000.
- [19] Y. H. Shih, Y. C. Chen, M. Y. Chen, Y. T. Tai, and C. P. Tso, “Dechlorination of hexachlorobenzene by using nanoscale Fe and nanoscale Pd/Fe bimetallic particles,” *Colloids and Surfaces A*, vol. 332, no. 2-3, pp. 84–89, 2009.
- [20] D. W. Elliott and W. X. Zhang, “Field assessment of nanoscale bimetallic particles for groundwater treatment,” *Environmental Science and Technology*, vol. 35, no. 24, pp. 4922–4926, 2001.
- [21] T. Zhou, Y. Li, and T. T. Lim, “Catalytic hydrodechlorination of chlorophenols by Pd/Fe nanoparticles: comparisons with other bimetallic systems, kinetics and mechanism,” *Separation and Purification Technology*, vol. 76, no. 2, pp. 206–214, 2010.
- [22] D. M. Cwiertny, S. J. Bransfield, K. J. T. Livi, D. H. Fairbrother, and A. L. Roberts, “Exploring the influence of granular iron additives on 1,1,1-trichloroethane reduction,” *Environmental Science and Technology*, vol. 40, no. 21, pp. 6837–6843, 2006.
- [23] H. Song and E. R. Carraway, “Reduction of chlorinated ethanes by nanosized zero-valent iron: kinetics, pathways, and effects of reaction conditions,” *Environmental Science and Technology*, vol. 39, no. 16, pp. 6237–6245, 2005.
- [24] W. A. Arnold and A. L. Roberts, “Erratum: Pathways of chlorinated ethylene and chlorinated acetylene reaction with Zn(0),” *Environmental Science and Technology*, vol. 32, no. 19, pp. 3017–3025, 1998.
- [25] W. A. Arnold, W. P. Ball, and A. L. Roberts, “Polychlorinated ethane reaction with zero-valent zinc: pathways and rate control,” *Journal of Contaminant Hydrology*, vol. 40, no. 2, pp. 183–200, 1999.
- [26] E. C. Butler and K. F. Hayes, “Kinetics of the transformation of halogenated aliphatic compounds by iron sulfide,” *Environmental Science and Technology*, vol. 34, no. 3, pp. 422–429, 2000.
- [27] W. A. Arnold, P. Winget, and C. J. Cramer, “Reductive dechlorination of 1,1,2,2-tetrachloroethane,” *Environmental Science and Technology*, vol. 36, no. 16, pp. 3536–3541, 2002.
- [28] P. M. Jeffers, L. M. Ward, L. M. Woytowitch, and N. L. Wolfe, “Homogeneous hydrolysis rate constants for selected chlorinated methanes, ethanes, ethenes, and propanes,” *Environmental Science and Technology*, vol. 23, no. 8, pp. 965–969, 1989.

Research Article

Preparation and Application of Sustained-Release Potassium Ferrate(VI)

Xuan Xu,^{1,2} Wei Wei,¹ Ping Tao,¹ and Yan Zhang¹

¹ Key Laboratory of Three Gorges Reservoir Region's Eco-Environment, Ministry of Education, Chongqing University, Chongqing 400045, China

² National Centre for International Research of Low-carbon and Green Buildings, Chongqing University, Chongqing 400045, China

Correspondence should be addressed to Xuan Xu; xuxuan@cqu.edu.cn

Received 30 December 2013; Revised 19 April 2014; Accepted 25 April 2014; Published 19 May 2014

Academic Editor: Yalei Zhang

Copyright © 2014 Xuan Xu et al. This is an open access article distributed under the Creative Commons Attribution License, which permits unrestricted use, distribution, and reproduction in any medium, provided the original work is properly cited.

In this study, a composite system for the sustained release of potassium ferrate(VI) (sustained-release K_2FeO_4) was prepared and applied for water treatment. The objective of this research was to maximize the effectiveness of K_2FeO_4 for water treatment by enhancing its stability using diatomite. The sustained-release K_2FeO_4 was characterized using X-ray diffraction, scanning electron microscopy, and Fourier transform infrared spectroscopy. The results indicated that no new crystal phase was formed during the preparation and some K_2FeO_4 crystals entered the pores of the diatomite. From K_2FeO_4 release experiments, we found that the decomposition rate of K_2FeO_4 was obviously decreased, which greatly improved the contact rate between released K_2FeO_4 and pollutants. Via degradation of methyl orange, which was used as a model pollutant, the influential factor of K_2FeO_4 content within the complete sustained-release K_2FeO_4 system was studied. The optimal K_2FeO_4 content within the sustained-release K_2FeO_4 system was approximately 70%. In natural water samples, sustained-release K_2FeO_4 at a dosage of 0.06 g/L and with a reaction time of 20 minutes removed 36.84% of soluble microbial products and 17.03% of simple aromatic proteins, and these removal rates were better than those observed after traditional chlorine disinfection.

1. Introduction

Potassium ferrate(VI), with the formula K_2FeO_4 , as an environmentally friendly water treatment agent with strong oxidizing power, can not only sterilize natural water but also remove various organic and inorganic compounds [1–3]. In addition, its reduction by-product, Fe(III), is an effective flocculent that can absorb suspended solid and hazardous substances [4, 5]. More importantly, compared with chloric disinfection, no hazardous disinfection by-products (DBPs) are generated in K_2FeO_4 treatment of drinking water [6–8]. However, to date, K_2FeO_4 has not yet been widely applied as a replacement for chloric disinfectants in drinking water treatment, mainly due to the poor stability of concentrated K_2FeO_4 [9, 10]. The reduction potential of K_2FeO_4 varies from +0.7 V to +2.2 V in basic and acidic solutions, respectively [3]. The ferrate anion decomposes quickly during

the treatment process, resulting in low efficiency for water purification.

The stability of K_2FeO_4 is determined by its purity, the pH value of the solution, and various other factors [11]. Using a hypochlorite oxidation method, Hrostowski and Scott [12] successfully prepared K_2FeO_4 with a purity as high as 96.9%, which dramatically improved its stability during storage. However, this had little effect on the use of K_2FeO_4 given that its stability is still poor during the water treatment process. Wagner et al. [11] reduced the decomposition rate of K_2FeO_4 by controlling the solution pH value. In high pH solution, the concentration of hydrogen ions (H^+) is low, leading to only weak catalytic decomposition. However, controlling pH is not commercially viable in practical water treatment processes.

In the present research, K_2FeO_4 crystals were absorbed into a porous media, diatomite, which has a highly porous structure and high surface area [13], enabling the subsequent

slow release of K_2FeO_4 into water in order to prolong the reaction time and consequently improve the efficiency and purification effect of K_2FeO_4 . This method does not require a specific K_2FeO_4 purity or solution pH value, and, therefore, the technical difficulties and high cost of K_2FeO_4 preparation can be drastically reduced for the practical application of K_2FeO_4 in water purification processes.

2. Materials and Methods

2.1. Chemicals. The following chemicals were of analytical reagent grade and used without further purification: ferric nitrate (Sigma Aldrich Reagent Co., Ltd.), calcium hypochlorite (Shun Chemical Reagent Co., Ltd.), potassium hydroxide (Chongqing Chuandong Reagent Co., Ltd.), and methyl orange (ChengDu Kelong Chemical Co., Ltd.). Diatomite (Chinasun Specialty Products Co., Ltd.) was of chemically pure grade and was used without further purification.

2.2. Preparation of Sustained-Release K_2FeO_4 . A paste of 15 g of $Ca(ClO)_2$ and 25 mL of 13 mol/L KOH solution were added to a 100 mL beaker. After mild stirring, the mixture was filtered using an 800-eye filtering cloth and then 20 mL saturated KOH solution was added to the filtrate. The mixture was filtered again using 800-eye filtering cloth and 8 g of $Fe(NO_3)_3 \cdot 9H_2O$, which had been ground fully immediately prior to use, was slowly introduced to the filtrate in the ice water bath five times. After 1 hour of continued stirring in an agitator, diatomite was added to the mixture. To achieve samples with different K_2FeO_4 content, 6.92 g, 11.87 g, 18.46 g, 27.69 g, or 41.54 g of diatomite was added to individual samples. Each mixture was stirred for 5 additional minutes, followed by a 30-minute precipitation step in an ice bath. After filtration of the mixture, the filter cake was collected as the sustained-release K_2FeO_4 sample. The theoretical weight of K_2FeO_4 in each sustained-release K_2FeO_4 sample was 27.69 g. The sustained-release K_2FeO_4 samples were labeled as Fe_{80} , Fe_{70} , Fe_{60} , Fe_{50} , and Fe_{40} based on the theoretical mass fraction of K_2FeO_4 in each sample. For example, Fe_{80} indicates that the theoretical mass fraction of K_2FeO_4 in the composite was 80%. When diatomite was not added, the sample contained only K_2FeO_4 .

2.3. Characterization of Sustained-Release K_2FeO_4 . The X-ray diffraction (XRD) patterns of the sustained-release K_2FeO_4 samples were obtained using a Shimadzu XRD-6000 diffractometer using Cu $K\alpha$ radiation (40 kV, 30 mA). Data were recorded over the range from 10° to 80° (2θ) with a scan rate of 4° min^{-1} . Fourier transform infrared spectroscopy (FT-IR) patterns were obtained using a Shimadzu IRPrestige-21 infrared spectrometer with the frequency ranging from 500 to 2000 cm^{-1} . Scanning electron microscopy (SEM) images were obtained using a FEI Quanta 450 scanning electron microscope.

2.4. Ferrate Release Rate of Sustained-Release K_2FeO_4 . To control the decomposition rate of Fe(VI), the release rate experiment of sustained-release K_2FeO_4 was carried out in

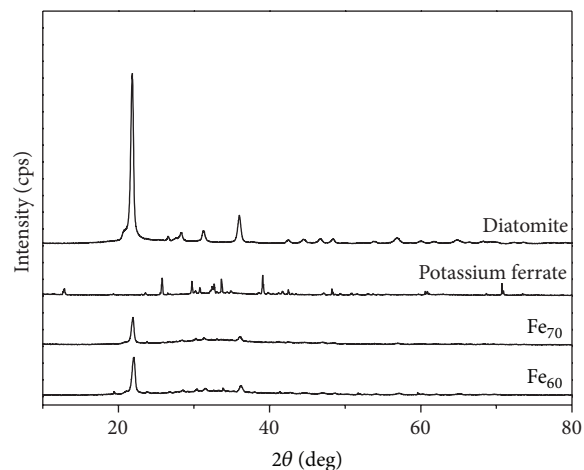


FIGURE 1: XRD patterns of Fe_{70} , Fe_{60} , K_2FeO_4 , and diatomite samples.

an ice water bath. First, 0.1 g pure K_2FeO_4 or a sample of each sustained-release K_2FeO_4 composite was added to a 250 mL beaker containing 250 mL water. The solution was then agitated at 60 rpm for 30 min in the ice water bath, and, finally, the concentration of Fe(VI) in solution was determined according to the adsorption at 510 nm using a spectrophotometer.

2.5. Degradation of Methyl Orange. Eight test solutions of 20 mg/L methyl orange were prepared by dissolving methyl orange granules in deionized distilled water. Then, 0.125 g Fe_{80} , 0.143 g Fe_{70} , 0.167 g Fe_{60} , 0.200 g Fe_{50} , 0.250 g Fe_{40} , 0.100 g K_2FeO_4 , 0.043 g diatomite, and a simple mixture of 0.100 g K_2FeO_4 and 0.043 g diatomite were added individually to these test solutions. The theoretical weight of K_2FeO_4 in all seven K_2FeO_4 -containing samples was 0.100 g. Each test solution was stirred rapidly and then allowed to stand for 20 min. The methyl orange degradation rate was calculated according to the concentration of methyl orange. The concentration of methyl orange was determined by fluorescence spectrophotometry using a Hitachi F-7000 fluorescence spectrophotometer, because methyl orange is a fluorescent substance [14]. The fluorescence intensity varied linearly with methyl orange concentration in the range of 5–20 mg/L, with a correlation coefficient of 0.998. Therefore, the concentration of methyl orange could be calculated using the fluorescence intensity value through a linear regression equation.

2.6. Degradation of Fluorescent Substances in Natural Water. Water samples were collected before and after liquid chlorine disinfection in a water supply network in Shapingba, Chongqing, China for comparative studies. The water in this network was treated for coagulation, sedimentation, and sand filtration before liquid chlorine disinfection. First, 0.015 g Fe_{70} was added to 250 mL water samples and then the changes in the three-dimensional fluorescence patterns were analyzed

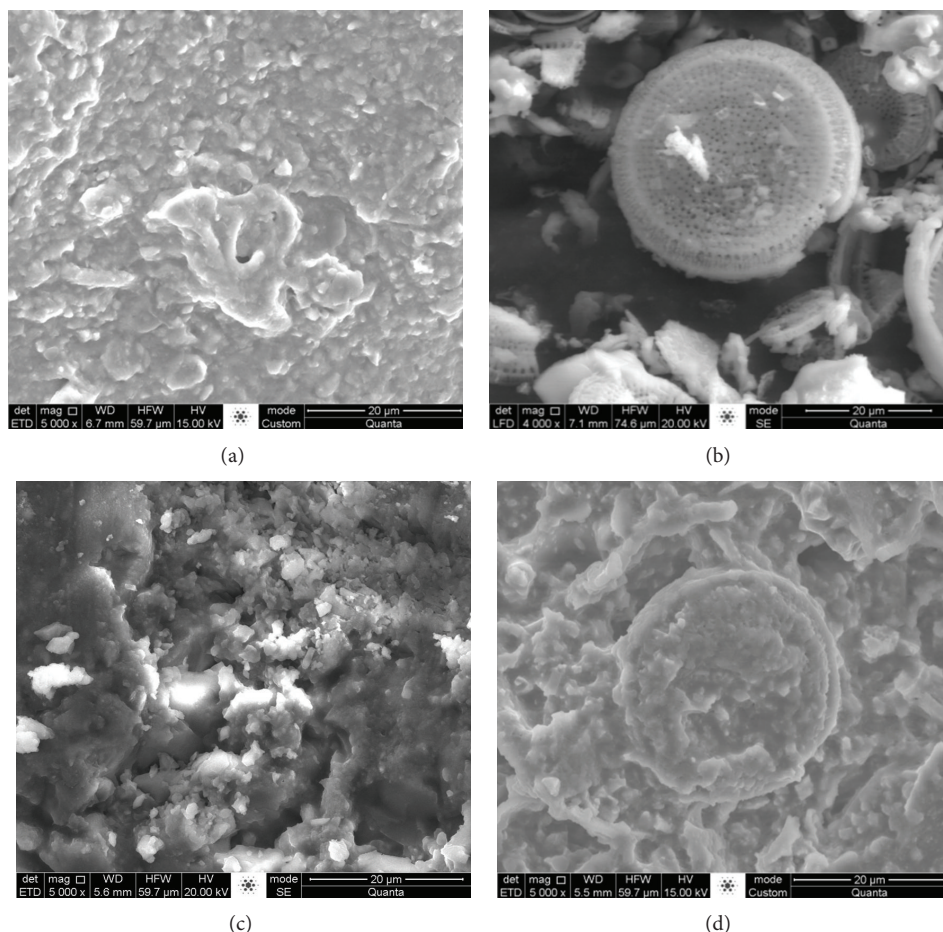


FIGURE 2: SEM images of Fe_{70} , Fe_{60} , K_2FeO_4 , and diatomite samples ((a) K_2FeO_4 ; (b) diatomite; (c) Fe_{60} ; and (d) Fe_{70}).

after a 20-minute reaction time. The resulting changes in fluorescence in the water samples were compared to those after the liquid chlorine disinfection process. Three-dimensional fluorescence patterns were obtained using a Hitachi F-7000 fluorescence spectrophotometer. The concentrations of soluble microbial products and simple aromatic protein also were determined according to the linear regression method used to determine the methyl orange concentration.

3. Results and Discussion

3.1. XRD Analysis of Sustained-Release K_2FeO_4 . The XRD patterns of Fe_{70} , Fe_{60} , K_2FeO_4 , and diatomite samples are shown in Figure 1. It can be seen that diatomite had two sharp diffraction peaks at $2\theta = 21.82^\circ$ and 36.00° . K_2FeO_4 had only one sharp diffraction peak at $2\theta = 29.72^\circ$. Other diffraction peaks belonged to the residual crystals of KOH and KNO_3 in the samples. The three sharp diffraction peaks of sustained-release K_2FeO_4 were at $2\theta = 21.82^\circ$, 29.72° , and 36.00° . Basically, the sharp diffraction peaks of Fe_{70} and Fe_{60} coincided with those of K_2FeO_4 and diatomite. In other words, no new crystal was generated during the preparation.

Therefore, the XRD analysis indicates that K_2FeO_4 and diatomite were combined by physical adsorption, which is beneficial to prevent the loss of K_2FeO_4 reactivity.

3.2. SEM Analysis of Sustained-Release K_2FeO_4 . Figure 2 shows SEM representative images of Fe_{70} , Fe_{60} , K_2FeO_4 , and diatomite samples. The particle size of K_2FeO_4 was roughly $2\ \mu\text{m}$. Due to its poor dispersion, an aggregation phenomenon was observed. The particle size of diatomite was approximately $35\ \mu\text{m}$, and void spaces (i.e., pores) between the particles were obvious. SEM images demonstrated that the voids in the diatomite were filled with K_2FeO_4 crystals, which even covered the surfaces of the diatomite. The particle size of K_2FeO_4 in the Fe_{70} samples was nearly the same as that of the pure K_2FeO_4 sample. Nevertheless, the dispersion of K_2FeO_4 particles in the Fe_{70} samples was much better than that of the pure K_2FeO_4 samples. Obvious aggregation of K_2FeO_4 particles was also visible in the Fe_{60} samples, with K_2FeO_4 crystals covering the diatomite surfaces. The K_2FeO_4 crystals covering the diatomite surfaces can dissolve in the water instantly and participate in the reaction, whereas the K_2FeO_4 crystals contained in the diatomite pores will dissolve

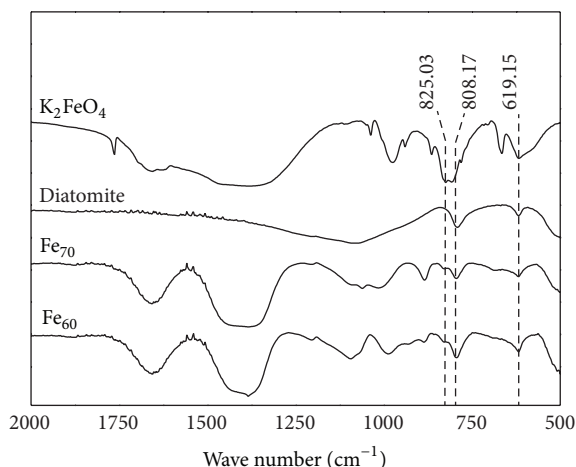


FIGURE 3: FT-IR spectra of Fe_{70} , Fe_{60} , K_2FeO_4 , and diatomite samples.

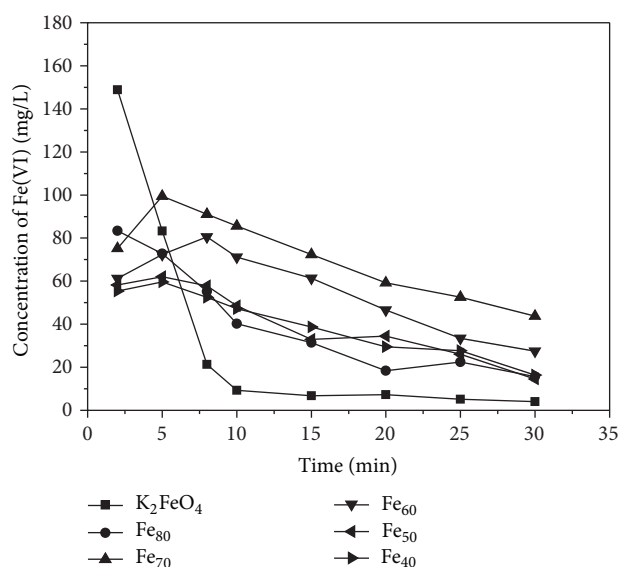


FIGURE 4: Ferrate release rate from sustained-release K_2FeO_4 samples. (Experimental conditions: ice water bath, 60 rpm agitation, and initial pH = 7.4~7.6.)

slowly and continuously and then react with substances in solution. Therefore, the SEM analysis indicates that a K_2FeO_4 proportion of 70% in the sustained-release K_2FeO_4 composites is appropriate for continued release of K_2FeO_4 .

3.3. FT-IR Analysis of Sustained-Release K_2FeO_4 . Figure 3 shows the transmittance FT-IR spectra of Fe_{70} , Fe_{60} , K_2FeO_4 , and diatomite samples. The IR absorption spectrum of the K_2FeO_4 sample includes a primary peak at 825.53 cm^{-1} , which can be recognized as the characteristic peak of FeO_4^{2-} and is attributed to the stretching vibrations of the Fe-O

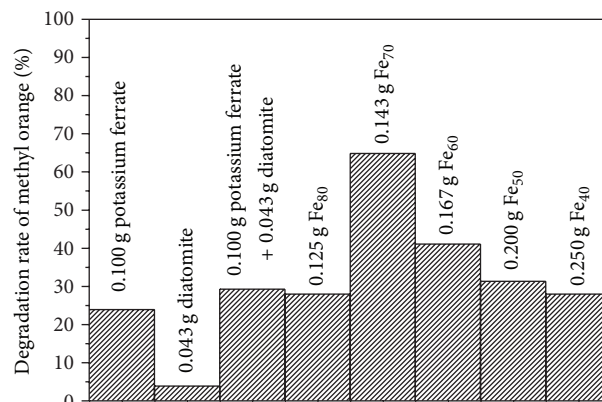


FIGURE 5: Removal rate of methyl orange using different treatments. (Experimental conditions: methyl orange concentration = 20 mg/L, solution volume = 500 mL, and reaction time = 20 min.)

bond [15, 16]. Other peaks may be the result of impurities in the K_2FeO_4 samples. The absorption peaks of the diatomite sample at 619.15 cm^{-1} and 808.17 cm^{-1} can be assigned to the stretching vibration of SiO-H. Both Fe-O and SiO-H bonds were detected in Fe_{70} and Fe_{60} samples, demonstrating the existence of K_2FeO_4 and diatomite in the composite samples.

3.4. Ferrate Release Rate from Sustained-Release K_2FeO_4 Samples. Figure 4 shows the changes in Fe(VI) concentration in solution after the addition of various sustained-release K_2FeO_4 composite samples. The figure shows that when pure K_2FeO_4 was added to the aqueous solution, the Fe(VI) concentration rapidly increased, reaching the maximum concentration within 2 min before beginning to decrease rapidly and showing complete degradation after 10 min. After addition of the sustained-release K_2FeO_4 samples in the aqueous solution, the Fe(VI) concentration was maintained at higher levels for longer periods, and the Fe(VI) decomposition rate was slower than that observed for pure K_2FeO_4 . Specifically, for the Fe_{70} , Fe_{60} , Fe_{50} , and Fe_{40} samples, the Fe(VI) concentration increased within 5 min, and the highest concentration from Fe_{70} samples reached 99.47 mg/L. These results demonstrate that sustained release of K_2FeO_4 was achieved from the diatomite pores observed in Figure 2. When sustained-release K_2FeO_4 was added to the water, K_2FeO_4 dissolved gradually starting from the outside of the samples and later from the inside of the diatomite pores, releasing Fe(VI) slowly and maintaining a higher concentration of Fe(VI) in solution. Such sustained, continuous release can reduce the decomposition rate of Fe(VI) and thereby improve the probability of interaction between Fe(VI) and pollutants, thus improving the effectiveness of Fe(VI) for water purification.

3.5. Degradation of Methyl Orange. Figure 5 presents the removal rate of methyl orange using different treatment agents. It is evident from this figure that the removal

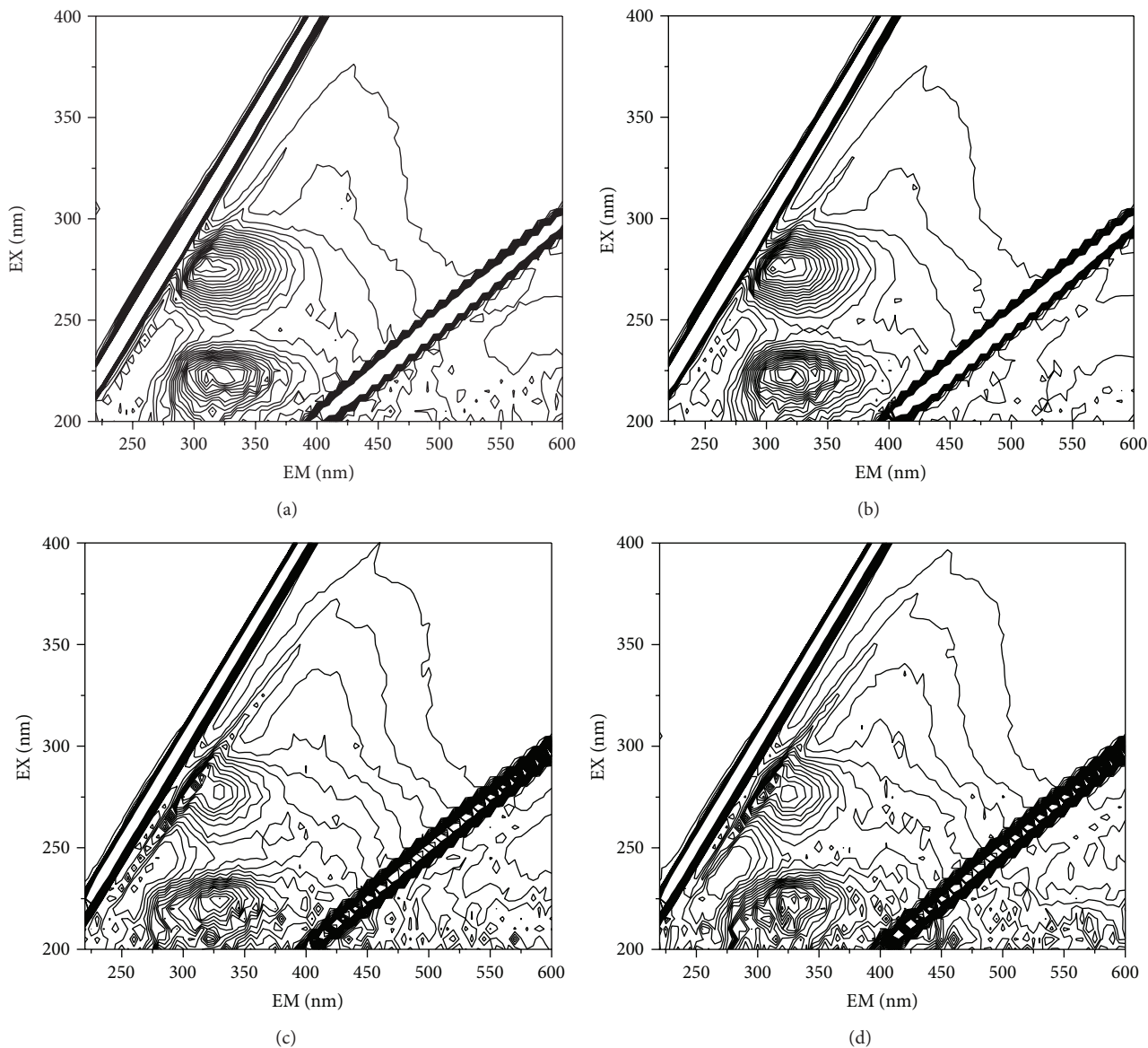


FIGURE 6: Three-dimensional fluorescence patterns demonstrating the removal of soluble organics by Fe_{70} and liquid chlorine. ((a) Water sampled before chlorine disinfection; (b) water sampled after chlorine disinfection: chlorine dosage = 1.5 mg/L, and reaction time = 30 min; (c) water treated by Fe_{70} : dosage = 0.06 g/L, and reaction time = 10 min; and (d) water treated by Fe_{70} : dosage = 0.06 g/L, reaction time = 20 min.)

rate of the simple mixture roughly equates the sum of the removal rate of K_2FeO_4 and diatomite. No synergistic effect was observed with the simple mixture of K_2FeO_4 and diatomite. The removal rates of methyl orange by sustained-release K_2FeO_4 samples were all higher than that using only K_2FeO_4 . However, considering that the diatomite within the sustained-release K_2FeO_4 samples could also absorb methyl orange, only the performances of Fe_{70} and Fe_{60} samples were better than those of the simple mixture. Specifically, 0.143 g of Fe_{70} and 0.167 g of Fe_{60} removed 6.49 mg (removal rate of 64.86%) and 4.11 mg (removal rate of 41.08%) of methyl orange, respectively. The removal efficiency of Fe_{70} was as 2.2 times that of the simple K_2FeO_4 and diatomite

mixture. Potassium ferrate formed a good Fe(VI) sustained-release structure, allowing Fe(VI) to be slowly released into the solution and thus reducing the decomposition rate of Fe(VI). As a result, the contact probability between Fe(VI) and methyl orange was increased and thus the removal rate of methyl orange was improved. For the simple mixture of K_2FeO_4 and diatomite, K_2FeO_4 quickly dissolved in the water, and most of the Fe(VI) failed to react with methyl orange. Therefore, the methyl orange removal rate with the simple mixture was significantly less than the rates achieved by the Fe_{70} and Fe_{60} samples. These results are consistent with those from the experiment determining the ferrate release rate from sustained-release K_2FeO_4 samples (Figure 4).

A possible reason for the reduced methyl orange removal rate at K_2FeO_4 mass fractions below 60% may be that the dosage of diatomite was high enough to cause an increase in the degradation rate of K_2FeO_4 . When the K_2FeO_4 mass fraction was above 70%, the crystal shape of the sustained-release K_2FeO_4 sample was approximately the same as that of the K_2FeO_4 sample and most of the K_2FeO_4 crystals failed to be absorbed into the pores of diatomite, which corresponded with a much lower removal rate of methyl orange.

In the process of sample preparation, the actual concentration of K_2FeO_4 is less than the theoretical value. We tested the purity of the prepared K_2FeO_4 and found that it was about 97%, which is close to the theoretical value. However, we could not determine the purity of the sustained-release K_2FeO_4 . However, the preparation time of sustained-release K_2FeO_4 is longer, and thus, the actual concentration of K_2FeO_4 in the sample may be significantly less than the theoretical value. For the degradation of methyl orange, the degradation effect is better after adding the theory amount K_2FeO_4 . This concluded that the degradation effect is better after adding the real amount of K_2FeO_4 .

3.6. Degradation of Fluorescent Substances in Natural Water.

Figure 6 shows the three-dimensional fluorescence patterns of water samples treated by traditional chlorine disinfection in a water network and Fe_{70} . Two fluorescence peaks were observed in these patterns at $\lambda_{ex}/\lambda_{em} = 275\text{ nm}/305\text{ nm}$ and $\lambda_{ex}/\lambda_{em} = 225\text{ nm}/330\text{ nm}$. These peaks represent soluble microbial products and simple aromatic protein [17]. After traditional chlorine disinfection, the fluorescence intensity at 275 nm/305 nm was reduced by 11.86%, but the fluorescence intensity at 225 nm/330 nm remained almost unchanged. The intensities of the two fluorescence peaks were reduced by 31.58% and 16.67%, respectively, after a 10 min treatment with Fe_{70} , and by 36.84% and 17.03%, respectively, after a 20 min treatment with Fe_{70} . The results indicate that the released K_2FeO_4 removed more soluble organic matter from the water samples than liquid chlorine. Thus, treatment with sustained-release K_2FeO_4 may improve the quality of purified drinking water.

4. Conclusions

In this study, a novel encapsulation method using hypochlorite oxidation to prepare sustained-release K_2FeO_4 was presented. The Fe(VI) release experiments demonstrated that diatomite as an encapsulation material affords the slow release of K_2FeO_4 into solution, which greatly increases the contact probability between released K_2FeO_4 and pollutants. The optimal mass fraction of K_2FeO_4 in the sustained-release K_2FeO_4 , among those tested, was found to be 70%. A maximum methyl orange removal rate of 64.86% was achieved with 0.3 g/L Fe_{70} and a reaction time of 20 min, for an initial methyl orange concentration of 20 mg/L. With an Fe_{70} dosage of 0.06 g/L and reaction time of 20 min, 36.84% of soluble microbial products and 17.03% of simple aromatic protein were removed from natural water samples.

Conflict of Interests

The authors declare that there is no conflict of interests regarding the publication of this paper.

Acknowledgments

Financial support from the National Natural Science Foundation of China (no. 51108483), the Natural Science Foundation Project of CQ CSTC (no. cstcjjA20002), the III Project (no. B13041), and the Fundamental Research Funds for the Central Universities (no. 106112013CDJZR210002) is gratefully acknowledged.

References

- [1] R. K. Murmann and P. R. Robinson, "Experiments utilizing FeO_4^{2-} for purifying water," *Water Research*, vol. 8, no. 8, pp. 543–547, 1974.
- [2] K. S. Kim, Y. K. Chang, S. K. Bae, and C. S. Hahn, "Selective oxidation of allylic and benzylic alcohols using potassium ferrate under phase-transfer catalysis condition," *Synthesis*, vol. 10, pp. 866–868, 1984.
- [3] V. K. Sharma, "Potassium ferrate(VI): an environmentally friendly oxidant," *Advances in Environmental Research*, vol. 6, no. 2, pp. 143–156, 2002.
- [4] J.-Q. Jiang and B. Lloyd, "Progress in the development and use of ferrate(VI) salt as an oxidant and coagulant for water and wastewater treatment," *Water Research*, vol. 36, no. 6, pp. 1397–1408, 2002.
- [5] Q. Han and W. Y. Dong, "Progress in development of potassium ferrate as new, highly efficient water treatment agent," *Environmental Science and Technology*, vol. 35, no. 12, pp. 200–205, 2012 (Chinese).
- [6] J. S. Mattice and H. E. Zittel, "Site specific evaluation of power plant chlorination," *Journal of the Water Pollution Control Federation*, vol. 48, no. 10, pp. 2284–2308, 1976.
- [7] M. J. Nieuwenhuijsen, M. B. Toledano, N. E. Eaton, J. Fawell, and P. Elliott, "Chlorination disinfection byproducts in water and their association with adverse reproductive outcomes: a review," *Occupational and Environmental Medicine*, vol. 57, no. 2, pp. 73–85, 2000.
- [8] J.-Q. Jiang, S. Wang, and A. Panagouloupoulos, "The exploration of potassium ferrate(VI) as a disinfectant/coagulant in water and wastewater treatment," *Chemosphere*, vol. 63, no. 2, pp. 212–219, 2006.
- [9] L. Delaude and P. Laszlo, "A novel oxidizing reagent based on potassium ferrate(VI) $^{1-}$," *The Journal of Organic Chemistry*, vol. 61, no. 18, pp. 6360–6370, 1996.
- [10] J. H. Qu, S. Lin, and L. L. Wang, "Aquatic stability of ferrate and its application in water treatment," *Acta Scientiae Circumstantiae*, vol. 21, pp. 106–109, 2001 (Chinese).
- [11] W. F. Wagner, J. R. Gump, and E. N. Hart, "Factors affecting the stability of aqueous potassium ferrate(VI) solutions," *Analytical Chemistry*, vol. 24, no. 9, pp. 1497–1498, 1952.
- [12] H. J. Hrostowski and A. B. Scott, "The magnetic susceptibility of potassium ferrate," *The Journal of Chemical Physics*, vol. 18, no. 1, pp. 105–107, 1950.
- [13] J. F. Lemonas, "Diatomite," *American Ceramic Society Bulletin*, vol. 76, no. 6, pp. 92–95, 1997 (Chinese).

- [14] L. Yu, J. Xi, H. T. Chan, T. Su, D. L. Phillips, and W. K. Chan, "The degradation mechanism of methyl orange under photocatalysis of TiO_2 ," *Physical Chemistry Chemical Physics*, vol. 14, no. 10, pp. 3589–3595, 2012.
- [15] W. He, J. Wang, H. Shao, J. Zhang, and C.-N. Cao, "Novel KOH electrolyte for one-step electrochemical synthesis of high purity solid K_2FeO_4 : comparison with NaOH," *Electrochemistry Communications*, vol. 7, no. 6, pp. 607–611, 2005.
- [16] Z. Xu, J. Wang, H. Shao, Z. Tang, and J. Zhang, "Preliminary investigation on the physicochemical properties of calcium ferrate(VI)," *Electrochemistry Communications*, vol. 9, no. 3, pp. 371–377, 2007.
- [17] Y. Han, X. J. Zhou, D. C. Peng, and X. C. Wang, "Effect of chlorination disinfection on three dimension fluorescence characteristic of DOM in secondary effluent," *Chinese Journal of Environmental Engineering*, vol. 6, no. 7, pp. 2226–2230, 2012 (Chinese).